ABSTRACT

Title of Document: BORON NEUTRON CAPTURE THERAPY FOR THE TREATMENT OF PROSTATE CANCER USING A BORON-CONTAINING CHOLESTERYL ESTER COMPOUND

Ian Alexander Gifford,
Doctor of Philosophy, 2013

Directed By: Professor Mohamad Al-Sheikhly, Department of Materials Science and Engineering

Boron neutron capture therapy (BNCT) for the treatment of prostate cancer using a boron-containing cholesteryl ester compound (BCH) was investigated. BNCT is a binary radiation therapy that relies on targeted delivery of ^{10}B to cancer cells followed by irradiation with thermal neutrons. High-linear energy transfer (LET) α particles and ^{7}Li nuclei released from the ^{10}B neutron capture event result in lethal double-strand DNA breaks within a 9 μm range. Given the high density energy deposition and short range, neighboring cells without ^{10}B remain unharmed. To evaluate the efficacy of BCH as a BNCT compound, a sample chamber within the thermal column experimental facility of the Maryland University Training Reactor (MUTR) was designed to provide a means of irradiating samples *in vitro* in a thermal neutron field. The thermal neutron fluence rate at 250 kW within the sample chamber is 8.69 $x10^{8}$ $n/cm^{2}/s$ with the < 3 eV neutron energy region representing 94.6% of the total neutron field. The hydrophobic BCH

compound was embedded in the lipid bilayer of DPPC:cholesterol liposomes for delivery to PC-3 prostate cancer cells. Liposomes were synthesized by the thin film layer technique with high-pressure homogenization size reduction. Dynamic light scattering analysis of the liposomes yielded a mean diameter of 111.5 nm and 0.113 relative variance. Cytotoxicity of the BCH-containing liposomes was evaluated by neutral red, MTS, LDH, and colony formation assays. Boron uptake by PC-3 cells was analyzed with high-performance liquid chromatography (HPLC) and inductively coupled plasma-mass spectrometry (ICP-MS). Drug delivery conditions that minimized cytotoxic effects yielded a boron uptake of 35.2 $\pm$ 4.3 μg/g cell. PC-3 cells were irradiated in the MUTR thermal column sample chamber to quantify the enhanced cell killing of the high-LET thermal neutron capture ^{10}B reactions. PC-3 cells treated with BCH and exposed to a 9.4 x 10^{11} n/cm^2/s thermal neutron fluence yielded a 20-25% increase in cell death compared to the untreated control.

BORON NEUTRON CAPTURE THERAPY FOR THE TREATMENT OF PROSTATE CANCER USING A BORON-CONTAINING CHOLESTERYL ESTER COMPOUND

By

Ian Alexander Gifford

Dissertation submitted to the Faculty of the Graduate School of the
University of Maryland, College Park, in partial fulfillment
of the requirements for the degree of
Doctor of Philosophy
2013

Advisory Committee:
Professor Mohamad Al-Sheikhly, Chair
Professor William Bentley
Professor Adam Hsieh
Professor Peter Kofinas
Professor Mohammad Modarres, Dean's Representative

Acknowledgements

There are many people to thank for their contributions to the completion of this dissertation, and without which would not have been possible. I would like to express my sincere gratitude to all that have taken the time to offer advice, motivation, resources, and time along the journey.

First, I would like to express my profound thanks to my advisor, Dr. Al-Sheikhly, for bringing me into his research group as a wandering undergraduate student, instilling confidence and scientific curiosity as core values, and motivating me to extend beyond my comfort zone to experience important successes and learning opportunities. Life takes many unexpected turns and I will always think back fondly on the path that led me to your mentorship. I would also like to express immense thanks to Vince Adams. Your devotion to the students that pass through the University is inspiring. Whether it relates to your uncanny ability to fix just about anything, creativity in problem solving, and advice provided at just the right times, I greatly value our friendship and appreciate your efforts. I would like to thank Dr. Wyatt Vreeland for his considerable efforts as a mentor throughout this research project. Your expertise in liposome preparation and light scattering, excitement in the pursuit of scientific discovery, and enthusiasm for exploring life have greatly impacted me and I appreciate everything you have done. Dr. Eric Burgett deserves tremendous credit for his contributions to this dissertation. Many days and nights spent discussing neutron spectrum unfolding, reactor physics, and the finer things in life are some of the fonder memories I have throughout graduate school and I

look forward to many years of friendship and collaboration between us. To my fellow graduate student Slavica Grdanovska, your help culturing cells and making liposomes was a huge benefit. Thank you very much and best of luck as you finish your graduate research. I would also like to thank my colleagues at AFRRI, Steve Miller, Dr. John Kalinich, Vernieda Vergara, and Dr. Lynn Cary, who without their support and expertise much of this research would not have been possible.

Most importantly, this dissertation was made possible due to the unconditional and endless love and support of my mom and dad, grandparents, and amazing wife, Katie. No words can express the gratitude I have for your devotion, inspiration, and the sacrifices you have made to encourage me to pursue my goals. I am reminded of my good fortune every day and love you all.

Table of Contents

List of Tables

List of Figures

Chapter 1: Introduction

According to the American Cancer Society, prostate cancer is the most frequently diagnosed cancer and the second leading cause of cancer death in men. It is estimated that 238,590 new cases of prostate cancer will occur in the United States this year (2013), with 29,720 cases resulting in death.[1] Because of this, the development of new treatment options involving targeted drug delivery to improve the efficacy of prostate cancer treatment is essential.

The goal of targeted drug therapy is to selectively deliver anti-cancer drugs to cancer cells, resulting in fewer side effects for the patient. One of the fundamental approaches is to design novel anti-cancer compounds that capitalize on the biological differences between cancer and normal cells. It has been reported that prostate cancer cells, like many other types of cancer cells, have high expression of low-density lipoprotein (LDL) receptors and lack feedback regulation of LDL receptor expression in order to accelerate their characteristic abnormal growth.[2] Therefore, targeted drug delivery can be accomplished by synthesizing cholesterol-based anti-cancer compounds specific to these LDL receptors. With this in mind, a new anti-cancer cholesteryl carborane ester compound (BCH) was synthesized for testing.[3] This compound was designed to mimic the native cholesteryl esters in the human body, and thus follow the same pathway to be selectively taken up by cancer cells via the elevated expression of LDL receptors within the cancer cell membrane.[4]

This research evaluates the efficacy of thermal neutron irradiation of prostate cancer cells containing the carborane compound, BCH, for the treatment of prostate cancer. The BCH compound has the potential to selectively target prostate cancer cells for boron neutron capture therapy (BNCT). Specifically, the development of a drug delivery method for preferential BCH-loading in prostate cancer cells, quantitative analysis of BCH uptake, cytotoxicity of boron-containing liposomes, and *in vitro* cell survival of BCH-containing cells following high-LET α particle and ^{7}Li release from ^{10}B thermal neutron capture have been investigated.

1.1 Global Objective

The global objective of this research is to investigate the efficacy of a novel boron-containing cholesteryl ester compound, BCH, as a targeting compound for BNCT of prostate cancer. To accomplish this goal, a thermal neutron irradiation facility at the University of Maryland was designed, fabricated, and characterized to provide a proper experimental facility to expose the boron-containing prostate cancer cells to a thermalized neutron beam with minimal high energy neutron beam contamination and γ-ray dose contribution. The global hypothesis of this dissertation is that by utilizing a targeted delivery pathway specific to prostate cancer cells, the boron-containing cells treated with the BNCT agent will exhibit lower cell survival following irradiation with a thermal neutron beam compared to the control cells that did not receive treatment with BCH.

1.1.1 Specific Hypotheses and Aims

1. The Maryland University Training Reactor (MUTR) is capable of providing a thermal neutron beam for the purpose of evaluating the efficacy of BNCT in biological samples.

- Design and fabricate a thermal column access plug for the irradiation of biological samples within the nuclear reactor thermal column.
- Characterize the neutron and γ-ray radiation fields within the thermal column access plug utilizing ionization chambers, foil activation, and computer modeling.

2. Encapsulation of BCH into the lipid bilayer of liposomes is an effective means of delivering the cholesteryl ester compound to prostate cancer cells.

- Quantify the loading efficiency of BCH encapsulation in liposomes following synthesis and size reduction.
- Analyze the size distribution of BCH-containing liposomes with dynamic light scattering.
- Measure the cytotoxic effects of the BCH-containing liposomes on the prostate cancer cells.
- Determine the delivery parameters required to attain sufficient boron loading within the prostate cancer cells by measuring the BCH uptake using high-

performance liquid chromatography (HPLC) and inductively coupled plasma-mass spectrometry (ICP-MS).

3. The targeted delivery of BCH to prostate cancer cells decreases cell survival following irradiation in a thermal neutron beam due to the generation of high-LET α particles and ^{7}Li nuclei from ^{10}B capture reactions.

- Compare the cell survival of prostate cancer cells with and without BCH after exposure to thermal neutrons using a colony formation assay.

Chapter 2: Technical Background

2.1 Physics of Boron Neutron Capture Therapy

Boron neutron capture therapy (BNCT) is a binary radiation cancer treatment with potentially significant therapeutic advantages compared to conventional chemical and radiation therapies. The treatment is based on specific cell killing by neutron irradiation of cancer cells that have been preferentially loaded with a boron-containing compound. The nuclear reaction between a thermal neutron and a ^{10}B atom produces a high-linear energy transfer (LET) α particle and ^{7}Li nuclei.

$$^{10}B + {}^{1}n \rightarrow {}^{7}Li\ (0.84\ MeV) + {}^{4}He\ (1.47\ MeV) + \gamma\ (0.48\ MeV) \qquad 94\% \qquad (2\text{-}1)$$

$$^{10}B + {}^{1}n \rightarrow {}^{7}Li\ (1.01\ MeV) + {}^{4}He\ (1.78\ MeV) \qquad 6\% \qquad (2\text{-}2)$$

These high-LET particles impart their energies in a relatively short range, approximately 9 and 5 μm respectively.[5] Because this distance is on the same scale as a typical cell diameter, the particles are theoretically capable of fatally damaging cells containing the ^{10}B, while leaving neighboring cells unharmed.[6-8] The 1.5 MeV α particles that result from this capture reaction have an average LET of ~200 keV/μm, therefore capable of imparting lethal damage when only a few particles deposit their energy.[9] Figure 2-1 provides a schematic for this reaction.

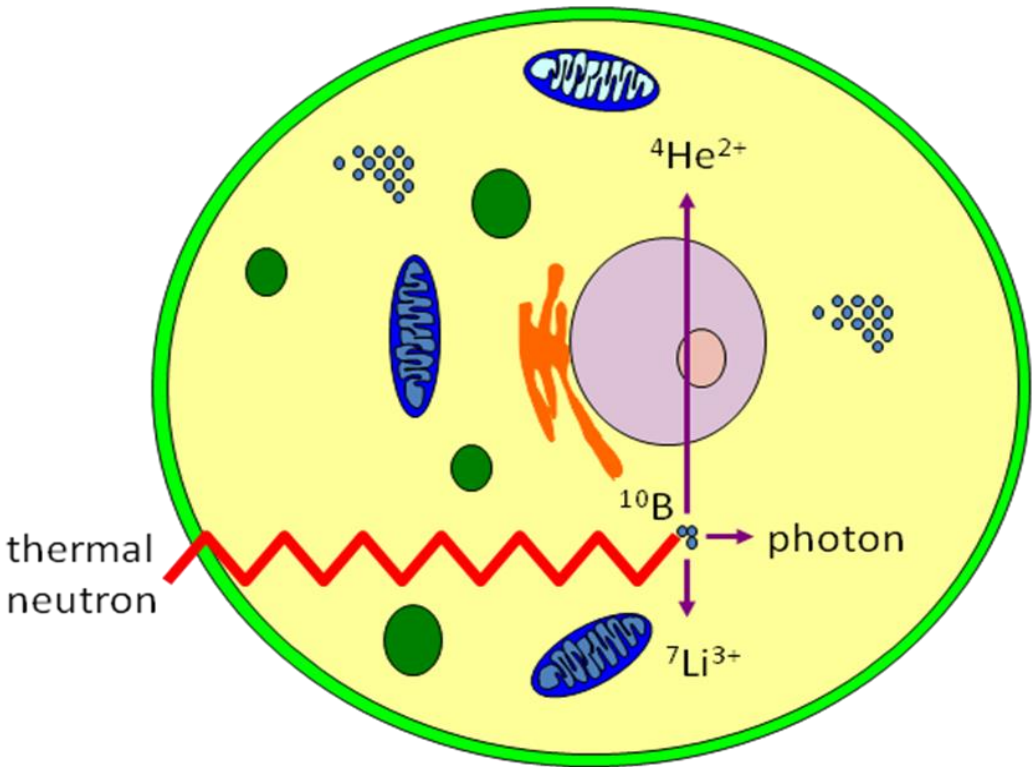

Figure 2-1. BNCT cell killing mechanism from ^{10}B capture of a thermal neutron resulting in the release of a high-LET α particle and ^7Li nuclei.

It is important to note that hydrogen and nitrogen found within normal tissue can also participate in capture reactions to produce γ-rays and protons. However, the thermal neutron cross sections of these atoms are very small in comparison to ^{10}B, as shown in Table 2-1, and do not contribute significantly to the thermal neutron capture dose associated with BCNT irradiations.

Table 2-1. Cross sections for relevant BNCT nuclear reactions.

Reaction	Cross Section (b)
$^{10}B\ (n,\alpha)\ ^{7}Li$	3838
$^{1}H\ (n,\gamma)\ ^{2}H$	0.332
$^{14}N\ (n,p)\ ^{14}C$	1.82

There are several advantages of BNCT for targeted treatment: (1) because the boron-containing compounds are neither required to be cytotoxic nor to release anti-cancer units in the cells, boron conjugates can be designed solely for targeted delivery purposes, (2) radiation can be applied in a time window (radiation window) when the therapeutic ratio of boron-containing compounds in the cancer cells versus the surrounding normal tissue reaches a maximum, and (3) BNCT is particularly suitable for prostate cancer treatment because the physiological location of the prostate is distant from many vital organs and can thus be targeted with a direct neutron beam.[5, 7, 10]

The biological effects of radiation damage are principally observed as damage to DNA. This damage can be the result of either direct or indirect action of radiation. In direct action, radiation interacts with the target DNA molecule causing ionization or excitation. While direct action can be initiated by any form of radiation (x-rays, γ-rays, charged and uncharged particles), it is most often the result of radiation with high-LET. LET is the amount of energy that is transferred to a material per unit length of the radiation track, and is a function of the size, charge, and energy of the radiation. Particles that are large

in size and carry a charge (i.e. α particles) are known as densely ionizing, while low-LET radiation (i.e. x-rays) is referred to as sparsely ionizing. Indirect action, on the other hand, occurs as radiation is absorbed by matter (typically water) surrounding the target DNA molecule, leading to the formation of free radicals. These free radicals then diffuse to the DNA and interact with the target molecule. Further discussion of radiation induced DNA damage is provided in Chapter 7.

2.2 BNCT Clinical Trials

The first clinical trials for BNCT of glioblastoma multiforme (GBM) with borax and sodium pentaborate as the boron agents were initiated in the 1950s at the Brookhaven National Laboratory (BNL) and the Massachusetts Institute of Technology Reactor (MITR), however they were terminated in 1961 when it was determined that the treatments were not as effective as anticipated.[11, 12] Analysis of the data showed that biodistribution studies and improved characterization of radiation sources were key factors that needed to be addressed for the future success of BNCT as a potential large-scale treatment option.[13] Studies began again in Japan in 1967 using BSH as the boron-containing agent in combination with tumor "debulking". Thermal neutron beams were utilized with craniotomies to increase neutron penetration and limit exposure to the skin.[14, 15] While failing to provide an increase in patient survival times, the results were promising when compared to previous reports. Clinical use of BPA to treat patients with cutaneous malignant melanomas began in the late 1980s.[16] Reported successes in these trials led to the first clinical trials using a BPA-fructose compound for the treatment

of GBM in 1994.[17] A key difference in these trials was the use of epithermal neutron beams to provide deeper tissue penetration, thus avoiding opening of the skull as previously performed in the Japanese trials. Other advantages included the development of Monte Carlo treatment planning, improved physical dosimetry, and reliable boron analysis techniques.[18] The trials at BNL and MITR produced results comparable to conventional photon therapies.[19] Trials from Sweden and Finland have shown considerable increases in survival times compared to trials in the USA, although direct comparisons are difficult due to variations in therapy planning. Other clinical trials for BNCT treatment of melanomas, head and neck tumors, and colon adenocarcinoma have taken place in the US, Japan, Germany, Finland, Czech Republic, Argentina, Sweden, and Taiwan. A complete review of these trials is beyond the scope of this dissertation and can be found elsewhere.[6, 18, 20]

2.2 Drug Design and Synthesis

The overall success of BNCT is contingent on the ability to synthesize boron-containing compounds that satisfy the following requirements: (1) selective targeting of cancer versus normal cells, (2) minimum cellular concentrations of ~10^9 ^{10}B atoms/cell (~20 μg/g tumor), (3) minimum tumor-to-normal tissue differential in the 3-5 range, (4) persistent cellular concentration of ^{10}B throughout the irradiation procedure, and (5) low toxicity levels at doses required to attain adequate cellular concentrations.[7, 21-23]

Currently, three boron-containing compounds are approved for clinical trials by the US Food and Drug Administration (FDA) with Investigational New Drug classification. The first, borocaptate sodium Na_2[*closo*-$B_{12}H_{11}SH$] (BSH), is a carborane derivative containing ten boron atoms per molecule that has been used in BNCT treatment of GBM, and its biodistribution in animals has been studied.[24-28] The second, 4-dihydroxyborylphenyl-alanine (BPA), is an amino acid containing one boron atom per molecule that has been used to treat patients suffering from malignant melanoma and GBM, with similar studies in animal biodistribution.[29-33] The third, polyhedral borane dianion [*closo*-$B_{10}H_{10}$]$^{2-}$ (GB-10), has been studied for its ability to treat GBM.[34, 35] Each of these compounds is shown in Figure 2-2.

Figure 2-2. FDA approved BNCT agents.

However, each of these compounds has limitations in selective tumor targeting and retention, leading to interest in the development of new compounds with the ability to better satisfy the criteria previously described. The goal of developing and evaluating more selective boron delivery agents has been deemed the single greatest need for the future progress and success of BNCT.[36] A more complete discussion of these compounds can be found elsewhere.[5, 37] In addition to these FDA approved drugs, many other compounds have been suggested as BNCT candidates including, but not

limited to: boronated porphyrins, boronated nucleosides and nucleotides, monoclonal antibodies, and growth factors.[5, 7]

A promising new cholesteryl carborane ester compound (BCH) was synthesized that mimics the structure of native cholesteryl ester and contains a carborane cage as the source of boron for BNCT.[4, 38] This compound was evaluated in this research project for targeted therapy of prostate cancer. The structure of BCH is shown in Figure 2-3.

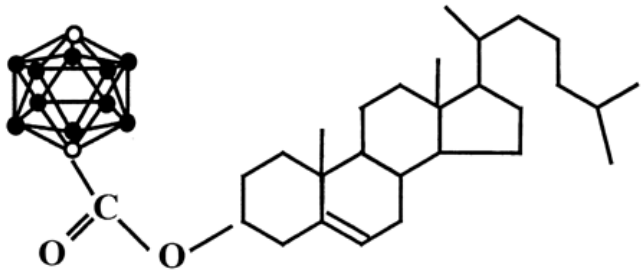

Figure 2-3. Chemical structure of BCH.

Similar to BSH, a boron cage is attached to the end of the molecule which contains ten boron atoms. In addition to this, the *para*-carborane cage increases the lipophilicity of the molecule, which may improve incorporation of the molecule into low-density lipoproteins (LDL).[39-41] Due to the high hydrophobicity of the BCH molecule, incorporation in a liposome formulation is required for delivery into a biological system.[4] Studies involving BCH uptake of normal neuron cells and brain glioma tumor cells have demonstrated the ability of this anti-cancer agent to preferentially target cancer cells.[42-44]

2.3 Targeted Drug Delivery

The success of BNCT rests in the ability to specifically target cancer cells for delivery of boron while limiting the uptake by normal cells. Methods to address this issue include synthesis of individually targeting boron-containing compounds, conjugation of boron-containing compounds to macromolecules, and encapsulation of the compounds in microcapsules.[5, 7]

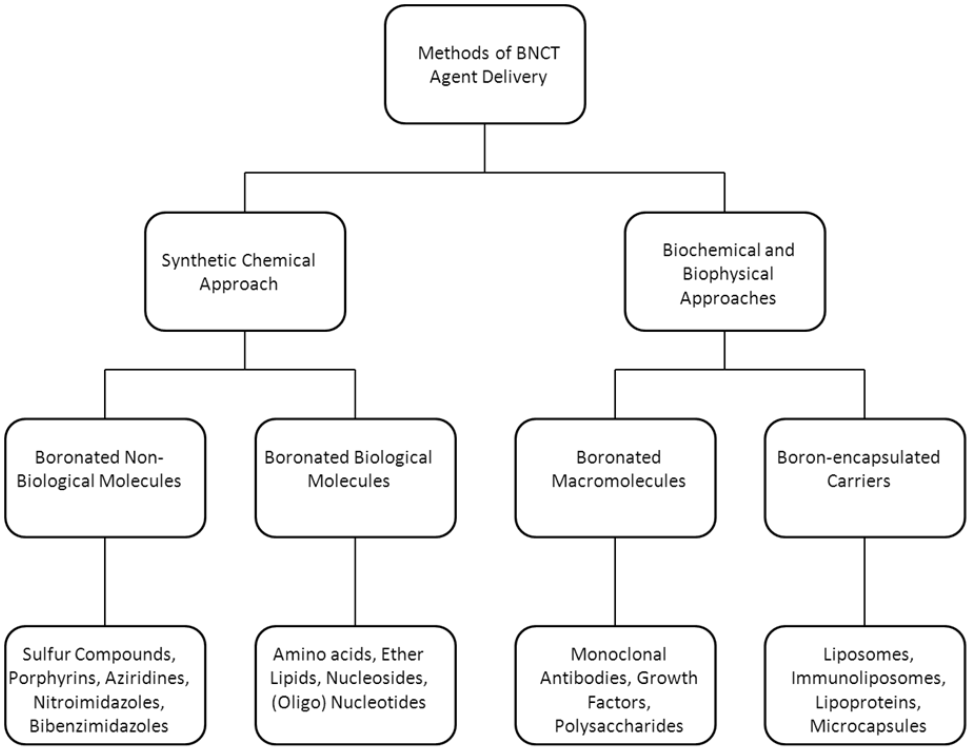

Adapted from Metha *Parm. Res.* 1996

Figure 2-4. Methods of BNCT agent delivery.

Another method for targeted delivery of ^{10}B to cancer cells is based on the over-expression of low-density lipoprotein (LDL) receptors by a variety of cancer cells.[45,

46] Specifically, it has been reported that human prostate cancer cells (PC-3) lack the feedback regulation of LDL receptors seen in normal human prostate cells.[2] LDL is a 20-25 nm particle consisting of a lipid monolayer containing apolipoprotein that binds to LDL receptors, surrounding approximately 1,500 cholesteryl esters within its hydrophobic core. LDL is the primary carrier of cholesterol in the blood stream and accounts for up to 90% of cholesterol found in the cell, the balance resulting from *de novo* synthesis.[47]

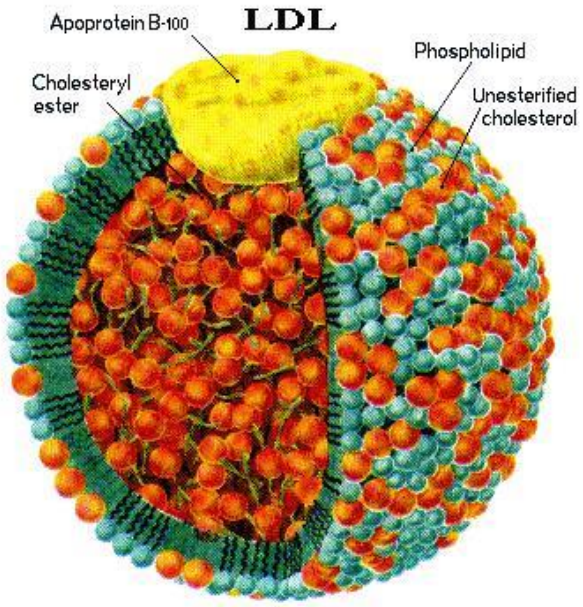

Figure 2-5. The structure of low-density lipoprotein (LDL).

LDL receptors are more active in many rapidly dividing cancer cells, likely due to the formation of new cell membranes which require high levels of cholesterol.[48, 49] The pathway for cellular uptake of LDL is termed receptor-mediated endocytosis and relies on cellular synthesis of transmembrane LDL receptors that are expressed on the cell surface. Once LDL binds to the receptor it is endocytosed into the cell and transported to

the lysosomes, where the LDL particles are hydrolyzed to form free cholesterol that can be used by the cells.

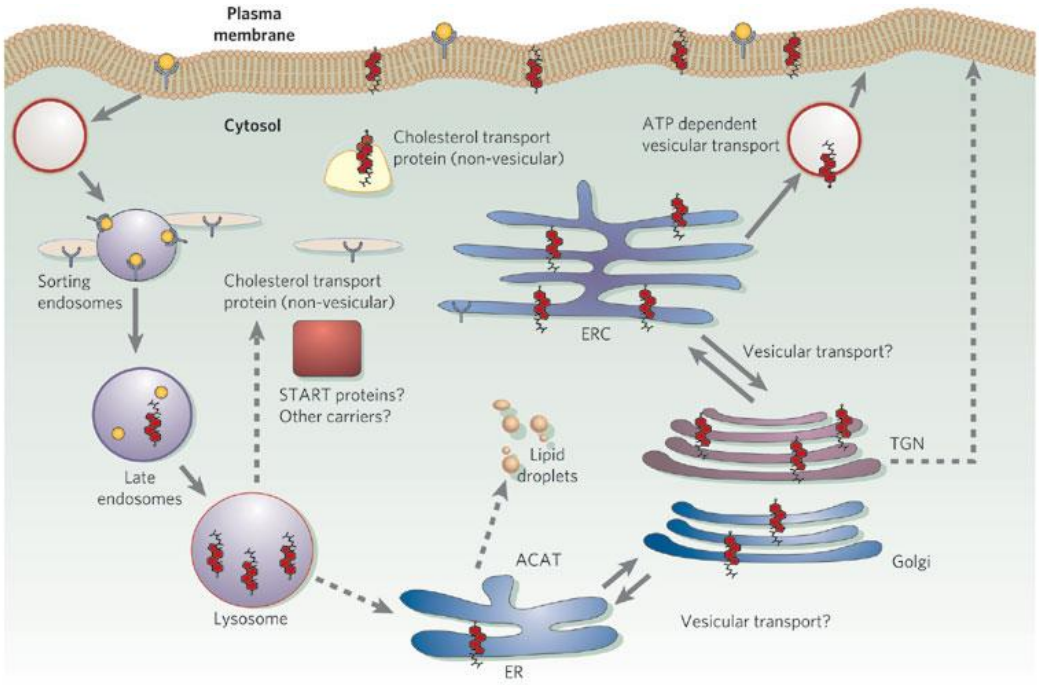

Figure 2-6. Mechanism of receptor-mediated endocytosis whereby LDL (yellow circles) carrying cholesterol and cholesterol esters bound to LDL receptors (light blue Y-shape) is internalized and transported to sorting endosomes and to late endosomes and lysosomes.[50]

In normally functioning cells, feedback regulation prevents expression of LDL receptors on the cell surface once a sufficient amount of cholesterol has been accumulated. In certain cancer cells however, this feedback is not present and cells will continue to endcytose LDL. Therefore, successfully incorporating BCH into LDL provides a means of not only preferentially targeting cancer cells, but also facilitating intracellular delivery of boron.

In order to introduce BCH into the LDL, the hydrophobic compound must be incorporated into liposomes. The liposomes contain a mixture of 1,2-dipalmitoyl-*sn*-glycero-3-phosphocholine (DPPC), cholesterol, and BCH. As described in Chapter 5, the compounds are mixed and dried to form a thin film which is then hydrated and agitated to form the liposome formulation. Following homogenization, the liposomes mix with LDL in the cell media. The liposomes provide a means of solubilizing the BCH and facilitate interaction with the LDL. Liposomes are able to interact with LDL through mechanisms of fusion, lipid transfer, and lipid exchange because they are both lipid based particles, creating an efficient means of loading hydrophobic drugs into LDL.[40, 42, 51]

2.4 Neutron Irradiation

An area of importance for the success of BNCT is the availability of a neutron source. To date, the dominant source of neutrons for BNCT is a fission reactor. An in depth discussion and review of modifications and construction of experimental facilities throughout the world for delivery of fission reactor-based neutron beams can be found in the following references.[52, 53]

Within the reactor core, neutrons are born from ^{235}U fission with energy ranging from fast to thermal. In order to improve the probability of interaction between neutrons and boron atoms within the cell, neutrons must be thermalized. This occurs by interaction with a moderator, causing neutrons to lose energy through collisions with other atoms. For clinical therapy, thermal neutrons that are incident upon the patient do not carry

enough energy to penetrate to the tumor depth. To resolve this problem, clinical sites are currently investigating the use of epithermal neutron beams that are moderated as they penetrate tissue, becoming thermal upon interaction with the tumor.[54, 55] Epithermal neutron beams have been utilized for BNCT therapy at reactors in the US at BNL and the MITR. In addition to this, reactors in The Netherlands, Finland, Sweden, the Czech Republic, and Japan are modifying reactors for research involving BNCT.[6] However, for research in an *in vitro* setting, the development of thermal neutron beams is of significant importance. Monoenergetic neutron beams from a ^{235}U fission source are not attainable and will always be contaminated with higher energy neutrons and γ-rays which lead to non-specific cell killing; but by increasing shielding and beam moderation, a higher proportion of incident radiation is delivered by thermal neutrons.

The capture of neutrons by ^{10}B is highly dependent on the energy of the incident neutron. The absorption cross section, which identifies the probability of interaction between a neutron and an atom, for boron is shown in Figure 2-7.

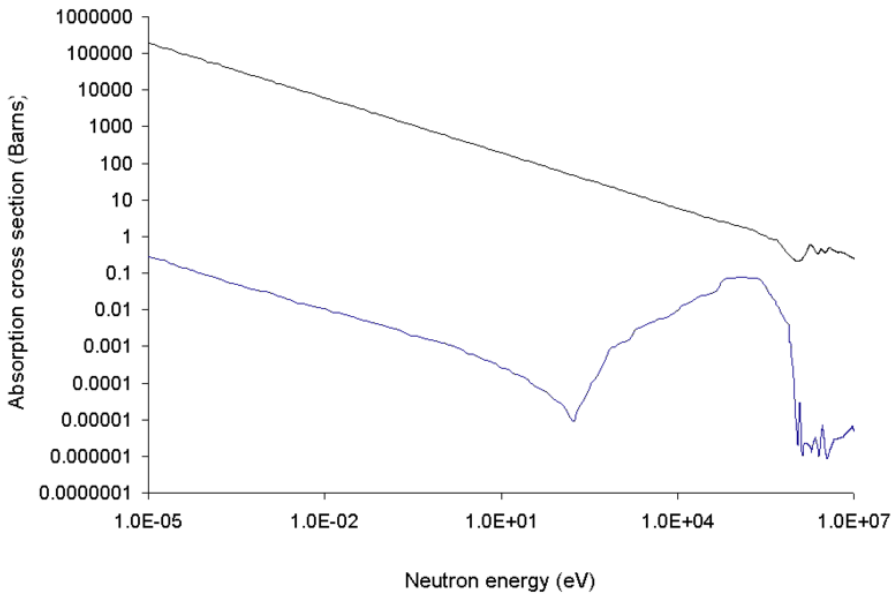

Figure 2-7. Absorption cross sections for ^{10}B (top) and ^{11}B (bottom).

As shown in the plot, the probability of neutron capture is largely dependent on the incident neutron energy. Therefore, it is very important to carefully characterize the neutron spectrum to ensure that the BNCT agent delivered to the tumor cells will undergo the capture process that results in the cell killing. The development and characterization of a thermal neutron experimental facility is discussed in Chapters 3 and 4.

There is great interest in the development of accelerator-based neutron sources (ABNS) for use in hospital settings; however, to date this mechanism of thermal neutron delivery is still in its infancy. In general, the achievable neutron fluence rates from ABNS compared to fission reactor sources are insufficient to provide the desired neutron fluence within a reasonable amount of time.[18] Development of this type of neutron source would be a landmark step in the clinical application of BNCT and is discussed in detail

elsewhere.[6, 7, 56-58] The first ABNS for clinical use is currently being developed in Japan by Sumitomo Heavy Industries and is expected to begin trials this year.[18]

Chapter 3: Nuclear Reactor Facility Development

3.1 Maryland University Training Reactor Facility

The 250 kW TRIGA Maryland University Training Reactor (MUTR) provides an ideal source of thermal neutrons for BNCT. The core of the MUTR presents a rectangular array of fuel elements consisting of UZrH fuel enriched to < 20% and three borated carbide control rods housed in a 6,000 gallon light water pool. The MUTR core is shown in Figure 3-1.

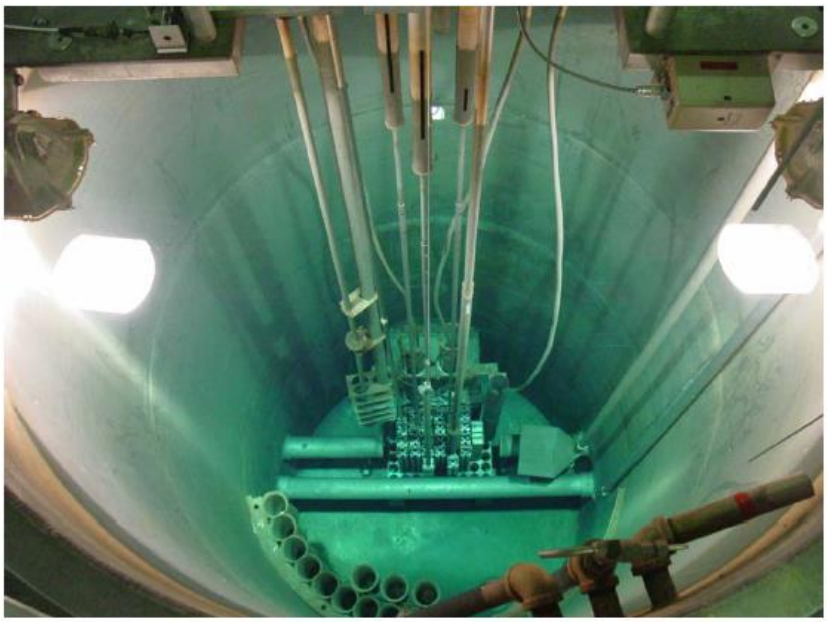

Figure 3-1. Overhead view of the 250 kW TRIGA MUTR core.

The fuel used in the MUTR core is referred to as Training, Research, Isotope production General Atomic (TRIGA) fuel due to its original design as a radiation source for research and training purposes. The design details and theory of TRIGA fuel can be found in GA

document GA-471 “Technical Foundations of TRIGA.”[59] Briefly, TRIGA fuel elements contain a mixed UZrH fuel-moderator surrounding a zirconium rod and clad in 304-stainless steel. Mixing the hydrogen moderator with the fuel allows for approximately 80% of the neutron moderation to occur within the fuel elements. The remaining 20% of neutron moderation occurs in the light water surrounding the MUTR core. The zirconium rod provides stability for the fuel element while minimizing neutron capture within the structural material. The stainless steel cladding provides safe encapsulation of fission products while allowing sufficient heat transfer from the fuel to the light water coolant and minimizing neutron absorption in non-fuel material. Graphite reflectors are positioned at the top and bottom of the fuel section to minimize neutron leakage. Figure 3-2 provides a schematic of a TRIGA fuel element.

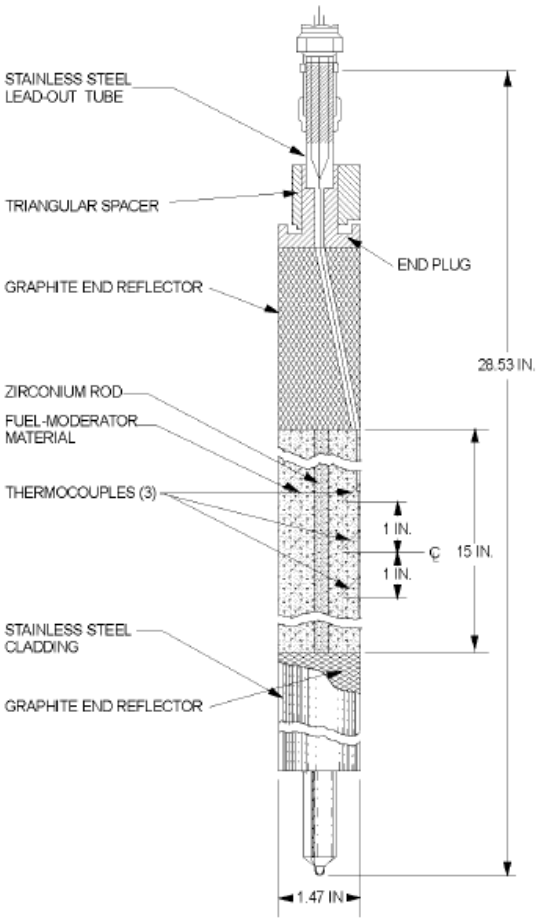

Figure 3-2. Schematic of a TRIGA fuel element.

To initiate the fission process, control rods are withdrawn from the core to increase the probabilty of neutron interaction with the ^{235}U within the fuel. A plutonium-beryllium neutron startup source provides the initial neutrons for the chain reaction. Neutrons are emitted from the startup source and travel through the light water moderator until they are captured by a ^{235}U atom. Once captured, ^{235}U undergoes fission whereby fission fragments, 2-3 neutrons, and photons are released.

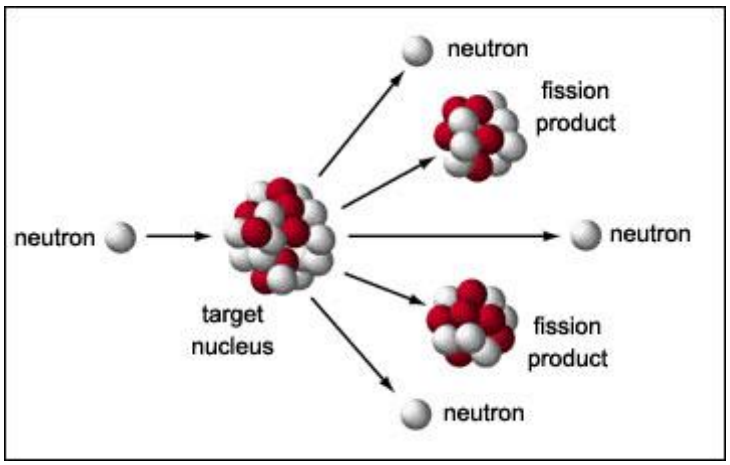

Figure 3-3. Thermal neutron capture of ^{235}U resulting in a fission event releasing 2-3 neutrons and fission fragments.

Of particular interest are the fission neutrons released from this reaction. Neutrons born immediately from the fission event are referred to as prompt neutrons and represent 99.3% of all fission neutrons. The remaining 0.7% are referred to as delayed neutrons and are emitted at a later time following the decay of fission fragments, known as delayed neutron precursors. It is important to note that neutrons born from fission have a skewed Gassian energy distribution with an average energy of 1-2 MeV. There are higher energy neutrons emitted (on the scale of 10 MeV), however, as shown in Figure 3-4 the probability of these high energy neutrons is relatively low.

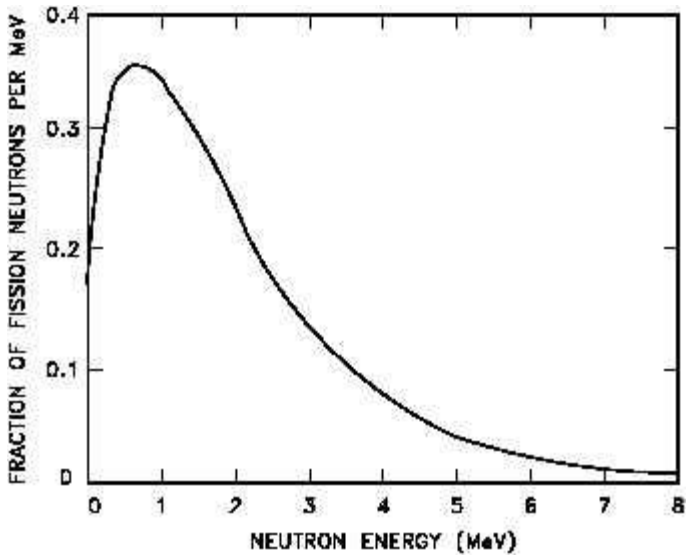

Figure 3-4. ^{235}U fission neutron energy spectrum.

Once born from fission, neutrons begin the process of moderation (also referred to as thermalization). As the neutrons pass through the hydrogenous material within the fuel matrix and light water surrounding the core, energy is transferred through collisions with similar Z (atomic number) matter and the epithermal and thermal energy regions are approached. Neutron moderation is critical because of the energy-dependent relationship between cross section and incident neutron. A representative cross section graph is presented in Figure 3-5.

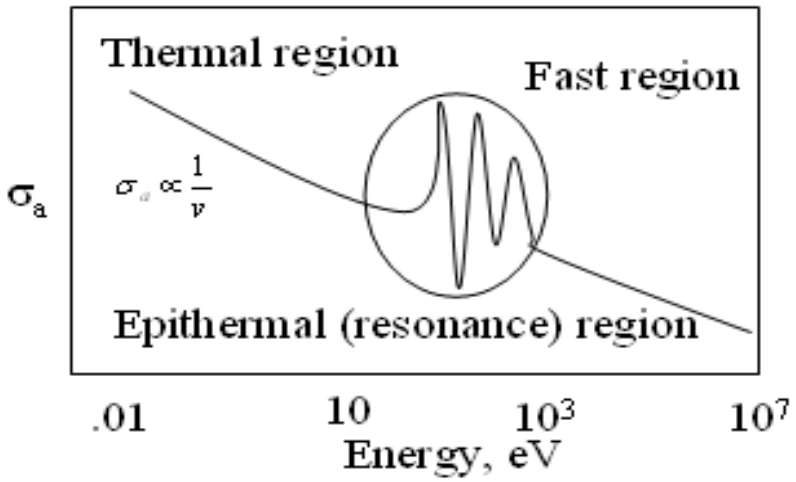

Figure 3-5. A representative neutron cross section as a function of energy identifying the thermal, epithermal, and fast regions.

The probability of neutron interaction increases proportional to 1/v in the thermal region. Because of this, a majority of ^{235}U fission events within the reactor core are a result of thermal neutron capture. Without adequate moderation to transition the higher energy neutrons born from a fission event to the lower energy regions, a chain reaction could not be sustained. Further discussion of neutron behavior as a function of energy and the importance of neutron moderation is found in Chapter 4.

While scattering within the fuel elements and light water moderator shift the neutron spectrum to a lower energy, further neutron beam moderation is required to produce a thermal neutron beam for BNCT. A schematic of the experimental facilities at the MUTR is shown in Figure 3-6.

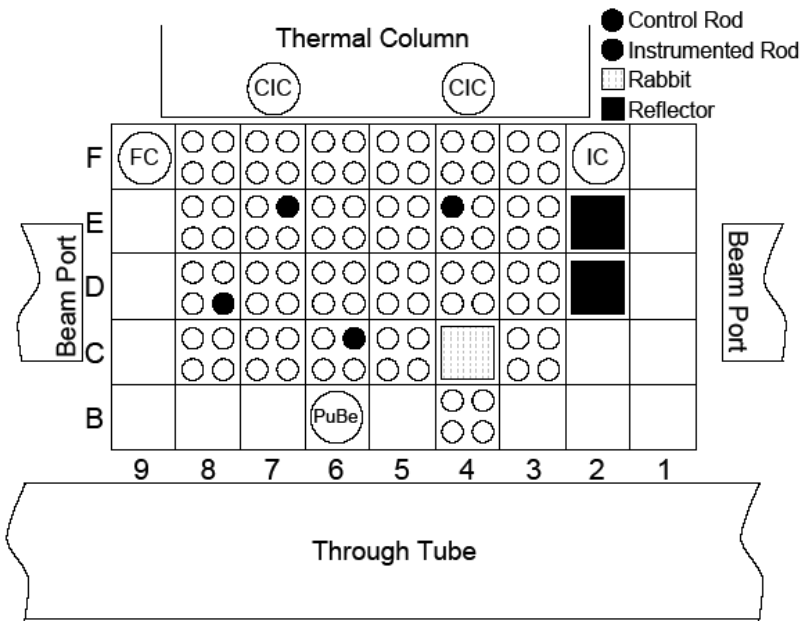

Figure 3-6. Schematic of the MUTR core and surrounding experimental facilities.

The thermal column [60] experimental facility was utilized for the *in vitro* BNCT irradiations. The TC is a graphite-filled housing extending from the southern face of the core through the pool tank wall and the concrete shield. The core end of the housing consists of a 0.953 cm (0.375 in.) thick aluminum sleeve that passes through an aluminum nozzle welded to the pool tank wall. The liner extends through the concrete shield and accommodates a steel-concrete shield plug at its outer end. The graphite assembly consists of 25.81 cm^2 (2 $in.^2$) graphite stringers arranged to form a stepped column 1.52 m (59.8 in.) in length. The section forward of the step is 0.959 m (37.8 in.) long and 0.610 m (24.0 in.) wide, in which the stringers are arranged in a 6 x 6 pattern. The outer section of the graphite column is 0.565 m (22.2 in.) long and 0.813 m (32.0 in.) wide with stringers arranged in an 8 x 8 pattern surrounded with 0.318 cm (0.125 in.) thick boral. Lead bricks surround the outer end of the TC graphite to provide shielding from γ–rays.

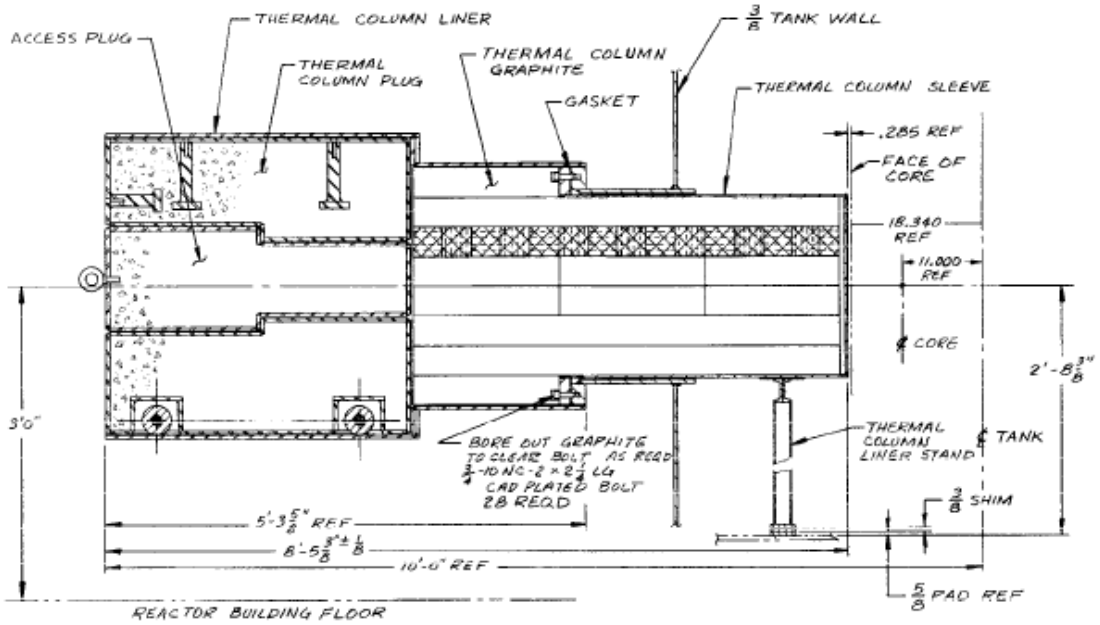

Figure 3-7. MUTR thermal column experimental facility.

3.2 Thermal Column Design and Fabrication

The original TC access plug was removed for the first time since the reactor was fueled with its current TRIGA rods in 1974 and replaced with a new setup which allows samples to be irradiated in the TC while controlling and monitoring the environmental conditions within the sample chamber. The goal was to provide a sample chamber where the surrounding gaseous atmosphere and temperature could be controlled throughout an irradiation and customized to the specific needs of the sample conditions. In addition to this, the new setup required adequate shielding during high power operations for the safety of personnel working in the reactor area. Figure 3-8 shows a schematic of the new TC access plug, highlighting the environmental control features and radiation shielding properties. The main structure of the access plug consists of 1.27 cm (0.5 in.) carbon

steel welded with carbon steel rod to minimize activation of the access plug during high power irradiations. The majority of this activation results from the neutron capture of ^{59}Co found in stainless steel. When a neutron is incident on ^{59}Co, neutron capture results in the formation of ^{60}Co, a strong gamma emitter with a half-life of 5.27 years. To avoid this potential source of radiation exposure to individuals working near the thermal column, as well as to minimize the non-specific irradiation of samples within the thermal column sample chamber, all steel used in the construction of the access plug was of the carbon variety. The sample chamber at the core end of the access plug measures 13 cm x 16 cm x 6 cm (5.11 in. x 6.30 in. x 2.36 in.) and is equipped with a thermocouple and inlet/outlet channels for gas flow around the sample. The gas flows through 0.635 cm (0.25 in.) OD copper tubing and is coiled on the outlet end to increase the time before the gas is vented from the access plug. This increases the time the gas is contained within the shielding and limits the release of radiation that results from neutron activation of the gases. Surrounding the sample chamber is a coil of 0.953 cm (0.375 in.) OD copper tubing through which heated or cooled water flows to control the temperature of the sample chamber. Similarly to the gas line, 15.24 m (50 ft.) of tubing is coiled within the access plug from the water outlet to limit the radiation levels external to the access plug. A temperature control unit which automatically responds to temperature fluctuations within the sample chamber during the irradiation is connected to the sample chamber thermocouple and water bath pump. The temperature of the sample chamber is controlled by a relay switch which turns on/off water flow according to the desired conditions. To provide adequate shielding during high power irradiations, the access plug was filled with normal concrete, as shown in Figure 3-9.

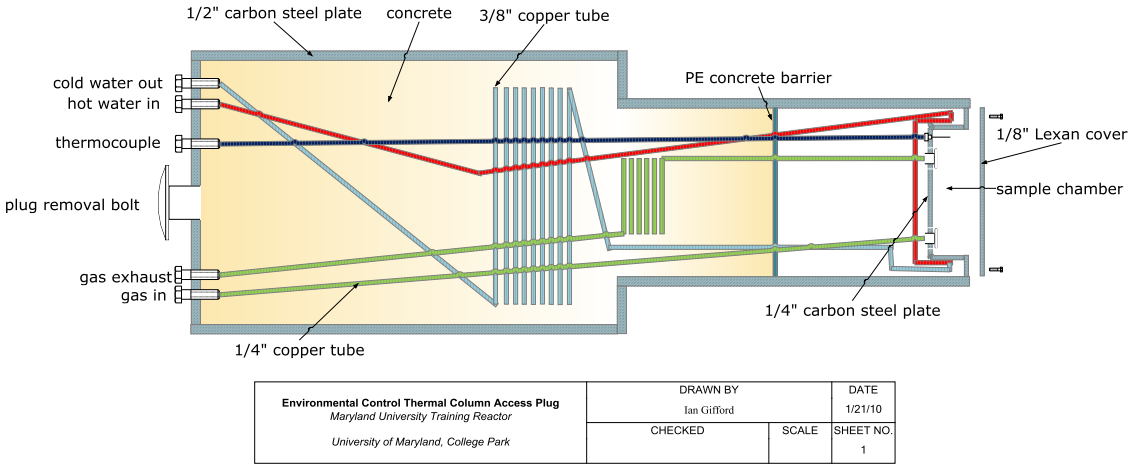

Figure 3-8. Schematic of environmental control thermal column access plug.

In order to insert and remove the thermal column access plug efficiently, a support table was fabricated as shown in Figure 3-10. The table is adjustable on 3 axes and equipped with ball bearings to allow easy movement of the access plug while seated on the table. The table is fixed in position on the exterior of the reactor wall, directly outside of the TC.

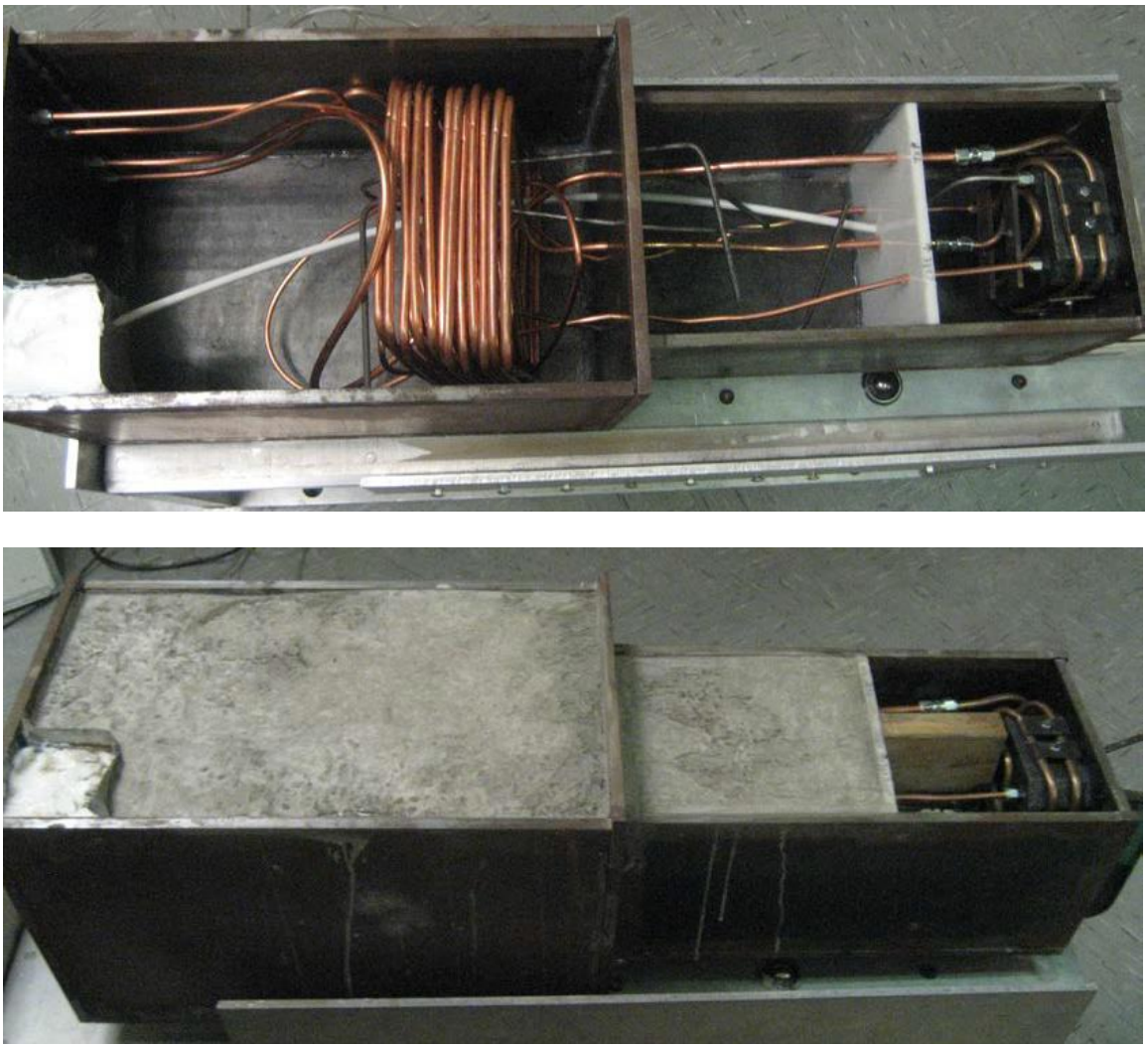

Figure 3-9. TC environmentally controlled access plug with gas and water lines plumbed to the sample chamber. The plug was filled with concrete to provide adequate radiation shielding during high power reactor operations.

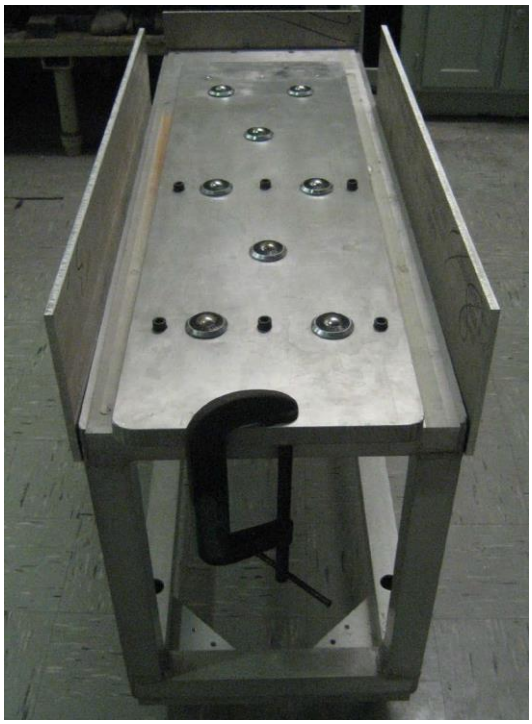

Figure 3-10. Customized table for insertion and removal of the TC access plug.

Chapter 4: Thermal Column Dose Mapping

4.1 Thermal Column Neutron Spectrum Unfolding

Proper characterization of a neutron field requires an understanding of the various neutron energies and their respective magnitudes within the field. Generally, neutrons are grouped into three main energy regions known as thermal (slow), epithermal (intermediate), and fast. Since neutrons are neutrally charged, the detection system always employs a reaction in which the neutron produces a charged particle or electromagnetic wave as a result. The probabilities of these reactions are directly dependent on the incident neutron energy and each energy region is dominated by a specific cross section type. The thermal regime is dominated by $1/\sqrt{E}$ and represents neutron capture resulting in activation or charged particle production, the epithermal regime is dominated by elastic and inelastic scattering as well as neutron capture producing γ–rays, and the fast reactions are dominated by atomic reactions such as fission, (n,2n), (n,charged particle) production type reactions as well as elastic scattering.[61] The techniques used to detect neutrons are divided into two subcategories, passive and active. Active detection relies on nuclear reactions that emit an energetic charged particle as a result of interaction with a neutron. The charged particle or recoiling nuclei directly ionize the detector material and the ionized material either emits light or the charge is collected on an anode. The signal generated by the charged particle gives a real-time indication of the presence of incident neutrons. Examples of active detectors include: $^{10}BF_3$ tubes, ^{3}He tubes, ^{10}B-lined proportional counters, ^{10}B-lined ionization chambers, $^{6}LiI(Tl)$ scintillators, and fission chambers.[61]

Passive neutron detectors do not provide a real-time response. These detectors "store" their response and can be read offline. These include detectors such as track-etch, thermal luminescent detectors (TLD), and activation detectors.[61] The track-etch detector relies on recoiling protons produced from neutrons scattering off hydrogen in poly(methyl methacrylate) (PMMA) to ionize and damage the PMMA, or other acrylic material, which is then etched in an organic solvent. The track path is preferentially etched and these tracks are then counted and correlated to neutron fluence and dose. TLD detectors are comprised of ^{6}LiF and ^{7}LiF materials. The probability of a ^{6}Li(n,α) reaction is considerably large at thermal neutron energies, while ^{7}Li has a non-existent (n,α) cross section. Both types of TLD material are equally susceptible to gamma radiation. The ^{7}Li reading is subtracted from the ^{6}Li reaction to give a total value of neutron fluence and dose. However, both TLD and track-etch detectors only provide an integral response to the neutron fluence rate and possess no ability to divine neutron spectral information. The last type of detector, the activation foil, can be used to quantify the energy-dependent neutron spectrum and neutron fluence rate. In the activation foil technique, a series of isotopes are used whose cross sections are uniquely independent with respect to the incident neutron energy. Each isotope is activated through a capture or charged particle production reaction and the resulting activation product is counted on a gamma ray detector, such as a High Purity Germanium (HPGe) detector. The activation rate can be calculated after accounting for the exposure time and delay time between exposure and counting on the gamma ray detector, both of which are known to high certainty. The most common passive detectors are thin foils and small diameter wires.

4.1.1 Neutron Detection by Activation Detectors

The high neutron reaction cross section associated with thermal neutrons makes passive detection an ideal method for unfolding neutron spectra within thermalized neutron fields. The foundation of this technique is based on the ability to induce radioactivity within a target material by exposing it to a field of thermal neutrons. One of the difficulties with measuring thermal neutrons is that most isotopes have a similar cross sectional shape in that neutron energy region. Because the spectral unfolding technique described in the following section requires unique energy-dependent responses, a variety of activation techniques must be incorporated to form unique responses. Despite this challenge, the activation technique offers one extreme advantage over other passive and active detection techniques, and that is because the passive activation foils responses do not change with respect to the neutron fluence rate. Active detectors can often suffer from pulse pileup, where the detector cannot register the signal as fast as the incident neutrons arrive.[61] In the activation technique, on the other hand, the detector decays at a known rate referred to as the half-life. If the foil is counted within ~7 half-lives, the HPGe detector can statistically quantify the amount of material that is present. In the following series of equations, this value of activity at time t can be used to determine the production rate, $\dot{P}$. This $\dot{P}$ value can then be used in the neutron spectral unfolding process to quantify the energy-dependent neutron spectra and total fluence rate. As a note prior to beginning the derivation of the production rate, the notation of fluence rate rather than flux is adopted throughout the following sections to maintain compliance with the SI unit systems. Fluence rate has units of $n/cm^2/s$ and refers to the amount of any

given particle which passes through a given area per unit time.[62]

The production rate, $\dot{P}$, is governed by the following equation:

$$\dot{P} = \varphi\sigma V \qquad (4\text{-}1)$$

where φ = energy-dependent neutron fluence rate

σ = energy-dependent microscopic cross section for the target reaction

V = target material volume

Therefore, the production rate is directly proportional to the neutron fluence rate. As the target material is exposed to the neutrons, radioactive nuclei, N, formed from the nuclear reaction increase. Once these radioactive nuclei are formed however, they begin to decay according to the decay constant for that particular nuclei. The rate of change of radioactive nuclei is described by the following differential equation:

$$\frac{dN}{dt} = \dot{P} - \lambda N \qquad (4\text{-}2)$$

where t = time

λ = decay constant

When one multiplies the number of radioactive nuclei by the decay constant, λ, the unit of activity (decays per second) is created. If one solves the above differential equation

with respect to N and multiplies by λ, one then achieves the activity, A, of the target material as a function of irradiation time, t:

$$A(t)= \dot{P}(1-e^{-\lambda t}) \qquad (4\text{-}3)$$

The activity of the target material will reach an equilibrium point, A_∞, known as the saturated activity once the material is irradiated in a neutron field for an infinitely long irradiation time. For irradiation times in excess of seven times the half-life of the radioactive nuclei, activation as a function of time is:

$$A(t)=A_\infty(1-e^{-\lambda t}) \qquad (4\text{-}4)$$

Upon removal of the target material from the neutron field, the induced radioactivity must be quantified. From this point in time, the radioactive nuclei are no longer being produced in the target material due to the absence of neutron fluence. The remaining radioactive nuclei continue to decrease by way of radioactive decay, hence the urgency to count the samples before the amount of activity falls below the minimum detectable activity of the detector system. The number of counts, C, as registered by the gamma ray detection system is determined by the following formula:

$$C = \varepsilon \int_{t1}^{t2} A_o e^{-\lambda(t-to)} dt + B = \varepsilon \frac{A_o}{\lambda} e^{\lambda to}(e^{-\lambda t1} - e^{-\lambda t2}) + B \qquad (4\text{-}5)$$

where ε = counting efficiency for a given gamma ray line

B = background counts

t_1 = starting count time

t_2 = ending count time

Combining formulas 4-4 and 4-5 yields a formula for saturated activity:

$$A_\infty = \frac{\lambda(C-B)}{\varepsilon(1-e^{-\lambda to})e^{\lambda to}(e^{-\lambda t1} - e^{-\lambda t2})} \qquad (4\text{-}6)$$

The equations discussed above assume that the activation product is not being activated further to produce a new product. This assumption has been quantified and calculated for isotopes used in the neutron spectrum unfolding. It was determined that the removal of the activation products through further activation is a negligible source of error and is therefore not necessary to consider in the calculations.

The saturated activity can be used to calculate the production rate, $\dot{P}$. The $\dot{P}$ value is then used to determine the magnitude of the neutron fluence rate. The following figure demonstrates the activation and decay scheme for any given activation foil and is representative of the activity of the target material as a function of time throughout the irradiation and counting phases.

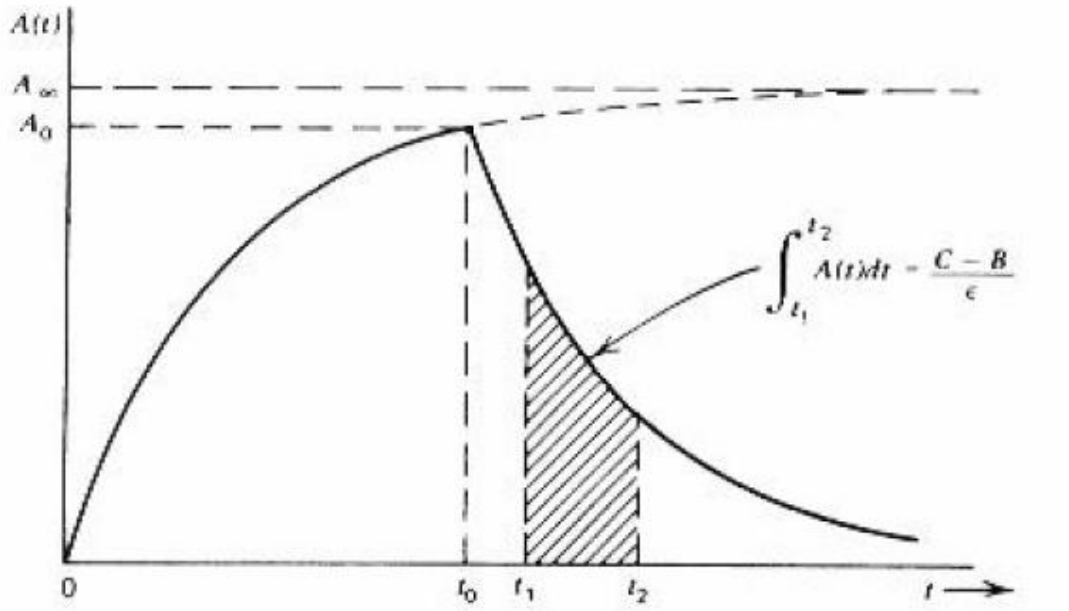

Figure 4-1. The activity of a target material during and following irradiation in a neutron field.[61]

As shown in formula 4-1, the production rate is directly influenced by the neutron reaction cross section of the target material. The neutron cross section is not constant for all neutron energies, but rather varies as a function of the energy of the incident neutron. The fission cross section as a function of neutron energy for ^{235}U is shown in Figure 4.2.

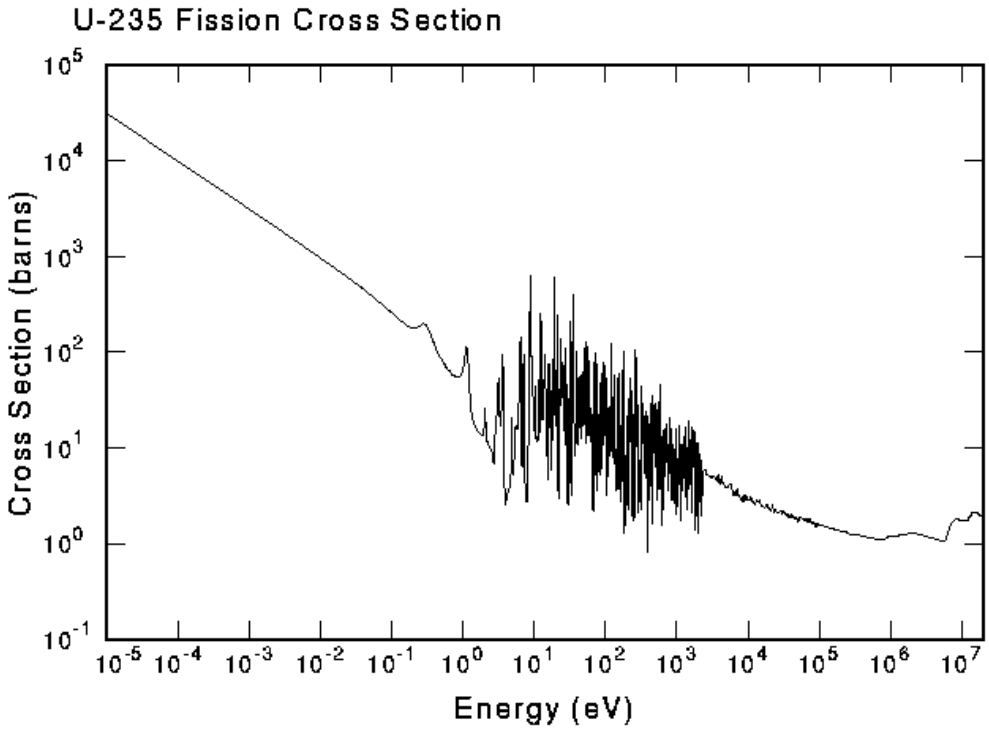

Figure 4-2. ^{235}U fission cross section as a function of neutron energy.

The cross section for each nucleus has unique variations as a function of energy, and by taking advantage of these variations it is possible to further unfold the energies of the neutron field beyond the broad thermal, epithermal, and fast regions. By comparing the responses to a wide range of irradiated target materials, also referred to as detectors, with precisely characterized cross sectional spectra, a higher resolution of neutron energies can be attained. A list of common target materials is provided in Table 4-1.

Table 4-1. Target materials for passive neutron detection.

Target Material	Target Isotope	Abundance (%)	Reaction	Cross Section (barns)	Isotope	$T_{1/2}$	Decay Mode	Decay Energy (MeV)	Decay Probability (%)
Gold	^{197}Au	100	(n,γ)	98.66	^{198}Au	2.69 d	γ	0.411	95.6
Copper	^{63}Cu	69.17	(n,γ)	3.995	^{64}Cu	12.7 h	γ	0.511	35.2
Scandium	^{45}Sc	100	(n,γ)	24.06	^{46}Sc	83.79 d	γ	0.889	100
								1.121	100
Indium	^{115}In	95.71	(n,γ)	181.6	^{116m}In	54.29 m	γ	1.294	84.4
								2.112	15.5
Iron	^{58}Fe	0.28	(n,γ)	1.153	^{59}Fe	44.47 d	γ	0.143	1.02
Silver	^{107}Ag	51.84	(n,γ)	34.17	^{108}Ag	2.37 m	β	1.649	97.15
	^{109}Ag	48.16	(n,γ)	80.66	^{110}Ag	24.6 s	β	2.892	99.7

In order to provide enhanced neutron spectrum unfolding resolution in the epithermal and fast neutron regions, the use of threshold reaction is common. These target materials exhibit unique neutron cross section behavior at specific energy levels, as shown in Table 4-2.

Table 4-2. Target materials for threshold reactions.

Target Material	Target Isotope	Abundance (%)	Reaction	Isotope	$T_{1/2}$	Threshold Energy (MeV)	Energy of Decay γ (keV)	γ Decay Probability (%)
Aluminum	^{27}Al	100	(n,α)	^{24}Na	14.95 h	4.9	1368.5	100
							2754.1	99.9
			(n,p)	^{27}Mg	9.46 m	3.8	834.8	71.8
							1014	28
Copper	^{63}Cu	69.1	(n,2n)	^{62}Cu	9.8 m	11.9	511	95
	^{65}Cu	30.83	(n,2n)	^{64}Cu	12.7 h	11.9	511	37.8
Nickel	^{58}Ni	68.08	(n,2n)	^{57}Ni	36 h	13	1370	86
	^{58}Ni	68.08	(n,p)	^{58}Co	70.86 d	1.9	810.77	99.45
Indium	^{115}In	95.71	(n,n')	^{115m}In	4.49 h	0.5	336.3	46.7
Titanium	^{46}Ti	8.25	(n,p)	^{46}Sc	83.79 d	5	889.25	99.98
							1120.5	99.99
	^{47}Ti	7.44	(n,p)	^{47}Sc	3.35 d	1.35	159.4	68
	^{48}Ti	73.72	(n,p)	^{48}Sc	43.67	4.5	983.5	100
							1037.5	0.975
Iron	^{56}Fe	91.75	(n,p)	^{56}Mn	2.58 h	4.9	840	99
	^{54}Fe	5.85	(n,p)	^{54}Mn	312.11 d	0.8	834.8	100
Magnesium	^{24}Mg	78.996	(n,p)	^{24}Na	14.95 h	6	1368.5	100
							2754.1	99.9
Vanadium	^{51}V	100	(n,α)	^{48}Sc	43.67 h	3	983.5	100

Gold	^{197}Au	100	(n,2n)	^{196}Au	6.18 d	8.6	333	22.9
							254.6	1.2
Zinc	^{64}Zn	48.8	(n,p)	^{64}Cu	12.7 h	2	511	37.8
Cobalt	^{59}Co	100	(n,α)	^{56}Mn	2.58 h	5.2	840	99
Tungsten	^{182}W	26.5	(n,2n)	^{181}W	121.2 d	8.5	57.53	32.7

And finally, the addition of resonance absorbers and neutron filters enables further customization to the unfolding of a neutron spectrum. By combining these materials with thermal neutron and threshold targets, finely tuned neutron energies can be extracted from the continuous spectrum of energies present in the neutron field. Table 4-3 provides some examples such absorbers and filters.

Table 4-3. Resonance absorbers and neutron filters used in passive detection.

Filter Material	Lower Window (MeV)	Upper Window (MeV)	Lower Cutoff (eV)	Upper Cutoff (eV)	Peak Cross Section (barns)
Zirconium	2	8			
Europium	0.1	1			
Iron	1	4			
Silver			4	10	3.00E+04
			10	11	2.00E+03
Bismuth			600	1050	1.00E+02
			1150	2250	2.00E+01
Cadmium			0.1	0.6	1.00E+04
Indium			1	3	3.00E+04
Uranium			4	8	1.00E+04
			10.5	12	1.00E+04
			12.5	13.5	1.00E+04

To further illustrate this concept, Figures 4-3 through 4-5 provide simulated detector responses for a range of incident neutron energies.

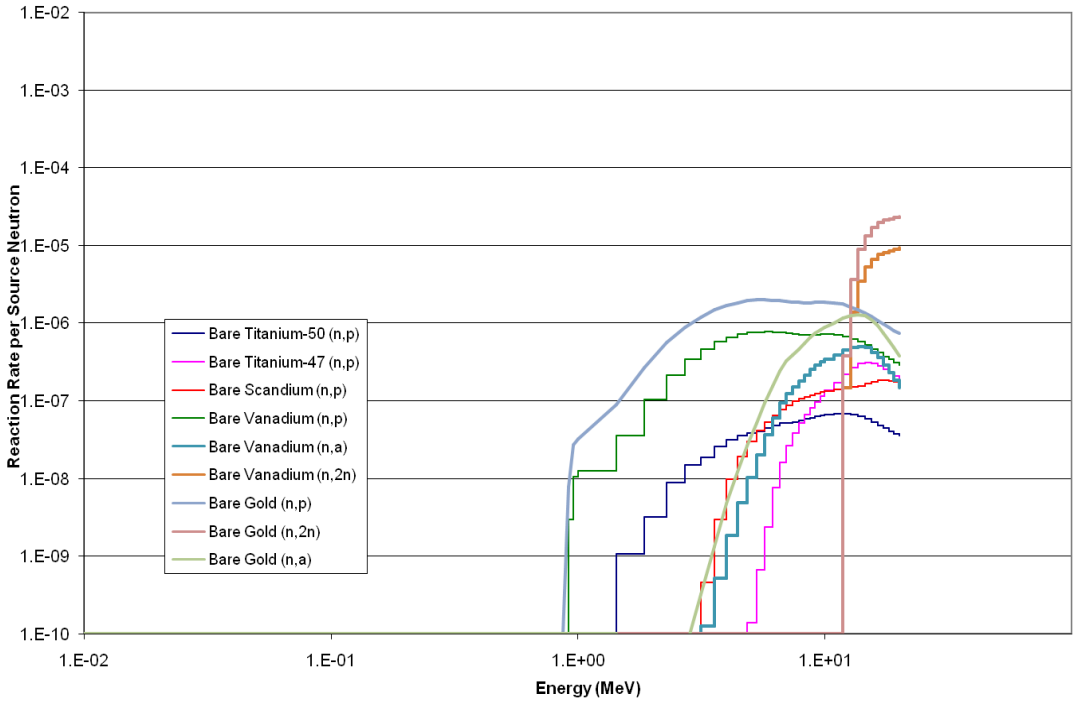

Figure 4-3. Energy-dependent reaction rates for threshold reaction materials in fast neutron spectroscopy.

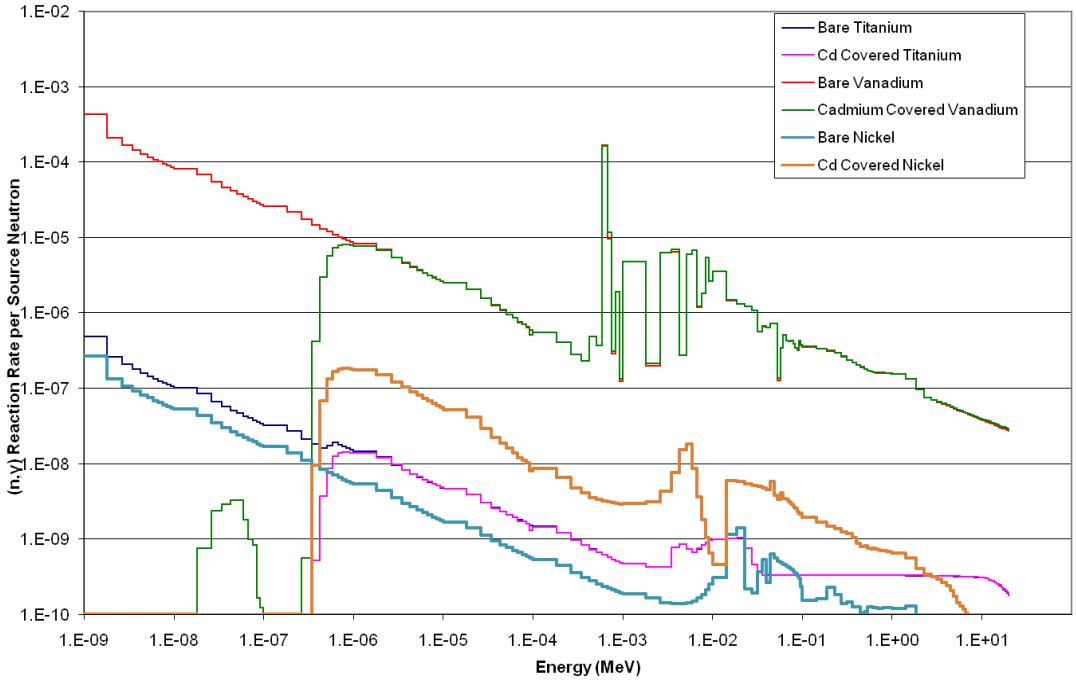

Figure 4-4. Energy-dependent neutron reaction rates for various activation foils described in Tables 4-1 through 4-3.

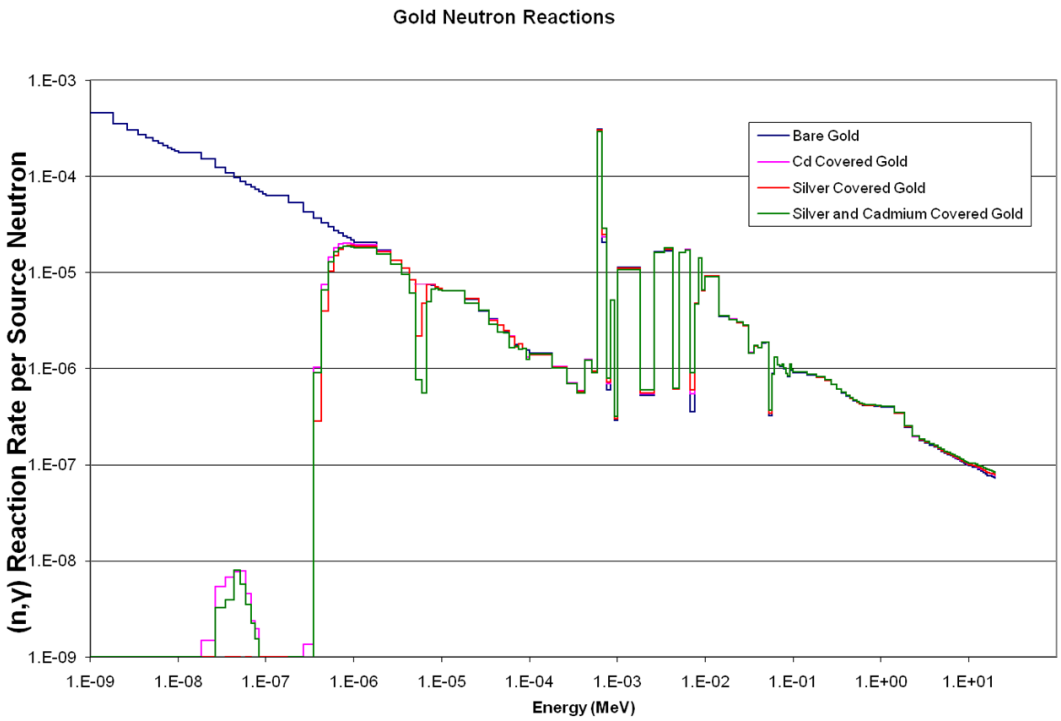

Figure 4-5. Energy-dependent neutron reaction rates for gold foils with various combinations of resonance absorbers and neutron filters highlighting the change in detector response below 1 eV.

A second method of integrating passive detection into neutron spectrum unfolding is the moderate and capture technique. Expanding upon the original designs of Bramblett, Ewing and Bonner, a moderate and capture technique was designed for quantifying the energy-dependent neutron fluence rate where the neutrons were known to emanate into the detector from one direction.[63] Rather than using resonance absorbers and neutron filters to shield target materials from certain neutron energies, the moderate and capture technique utilizes a series of detectors embedded in various thicknesses of neutron moderating material. This technique was used to supplement the resolution of resonance shielded activation foils. A schematic of this technique is shown in Figure 4-6.

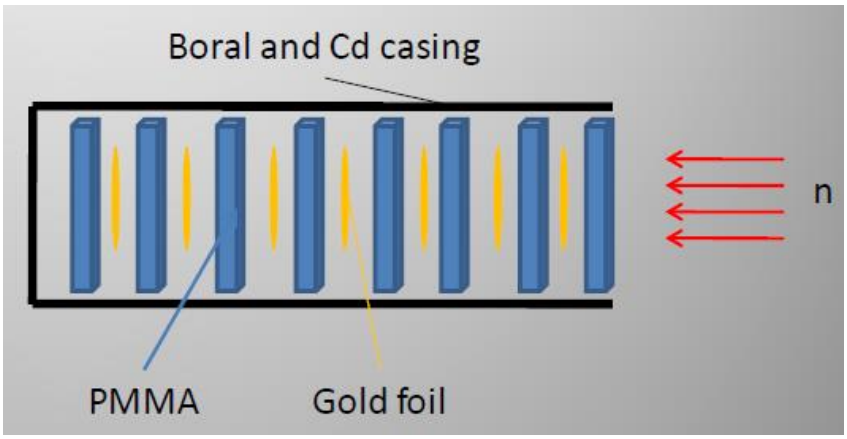

Figure 4-6. Schematic of the moderate and capture technique for neutron detection.

Because neutrons are thermalized efficiently by high hydrogen content material, varying thicknesses of hydrogenated materials provides varying degrees of neutron moderation. As a neutron field is incident on the target, neutrons are absorbed in the target material or scattered and thermalized within the moderator and continue through the detector system. Because the neutron absorption cross section for ^{197}Au is approximated as $1/\sqrt{E}$ with a higher value for lower neutron energies, neutrons with lower initial energies will be absorbed in the first foils while higher energy neutrons have a lower probability of capture and will continue to the next hydrogenous layer. After continuing further into the detector system, neutrons have a probability to be scattered and further thermalize. As the neutrons scatter within the PMMA, energy is transferred from the neutrons to the moderating material. The continuation of this scattering process results in a steady decrease of neutron energy as a direct function of the thickness of moderating material traversed. As the neutrons continue to thermalize, the probability of absorption by the target gold foil increases. Each layer of PMMA results in a further thermailzation of the neutron spectrum. The activation rate for each foil as a function of moderator thickness

results in a unique energy-dependent response. These unique responses, in concert with a known response matrix, are used in conjunction with the resonance shielding covered foils to unfold the thermal component to the neutron spectrum.

It is important to note that the directional detector system is succeptable to neutron scattering into the detector system from outside. This can lead to uncertainty and measurement error. Uncertainty due to neutrons that scatter into the detector system and result in activation of the foils has been minimized through careful design and engineering. This was accomplished by encapsulating the sides and rear of the unit in boral and cadmium, as both materials posess extremely large thermal neutron absorption and capture cross sections. The high thermal neutron capture cross sections of boral and cadmium prevent scattered neutrons from entering the downstream regions of the moderate and capture detector system without first passing through the acceptance aperature and entering the detector PMMA moderator region.

4.1.2 Analysis of Activation Detector Responses

Prior to analyzing the induced radioactivity within the detectors, the HPGe detector was calibrated with a NIST-traceable multi-nuclide calibration source to determine the detector efficiency at various photon energies. This energy-dependent detector efficiency is factored in at ε in formula 4-5. An HPGe spectrum of the NIST-traceable multi-nuclide calibration source is shown in Figure 4-7.

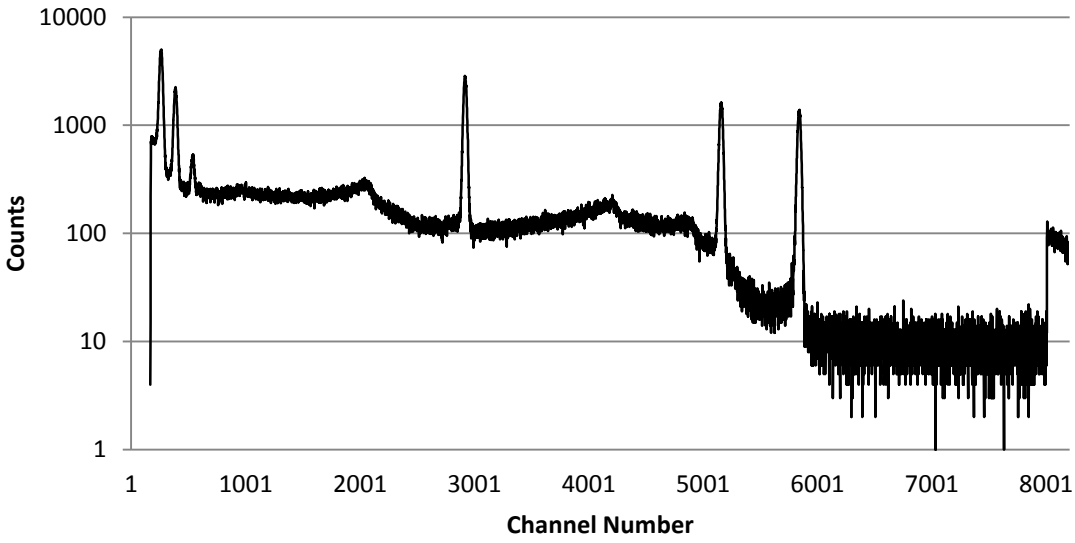

Figure 4-7. HPGe detector response for multi-nuclide calibration source.

The spatial distribution of the neutron fluence rate profile across the face of the thermal column access plug sample chamber was determined by irradiating a field of indium wires positioned along the planar window perpendicular to the dominant neutron field. The grid of indium wires was irradiated and analyzed to determine the production rate as a function of position within the neutron field. Figure 4-8 shows the spatial distribution of the neutron fluence rate across the face of the thermal column access plug.

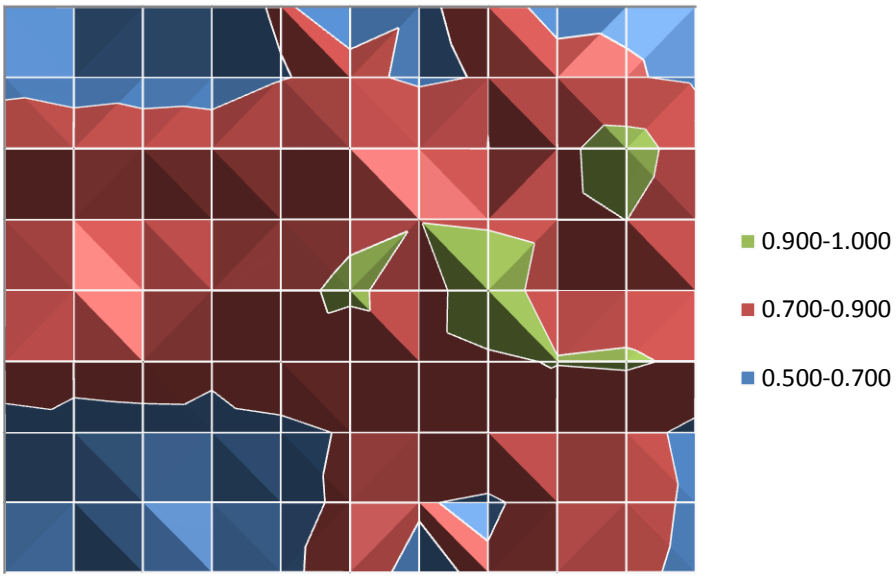

Figure 4-8. Normalized neutron fluence rate spatial distribution across the face of the thermal column sample chamber.

Analysis of the spatial profile of the neutron field across the face of the thermal column access plus reveals that the relative standard deviation across all regions of the TC sample chamber face is 13.8%. The peak fluence rate location is a factor of 1.78 higher than the lowest region. The thermal neutron fluence rate is maximal in the center region of the plug face. Scattering of thermal and epithermal neutrons in the air, water, and concrete filled sections surrounding the sample chamber contribute to an increased thermal neutron distribution within the center of the chamber.

After establishing the presence of a relatively uniform spatial distribution of neutrons in the sample chamber, there are two key correction factors that must be accounted for before unfolding the neutron spectrum. The first correction factor that must be applied to the passive detector response relates to the anisotropy of the neutron beam within the

thermal column of the MUTR. The calibration energy-dependent response matrix used in the analysis assumes a mono-directional neutron field passing directly along an axis on the face of the detector with the field incident on the acceptance aperture. The anisotropy of the neutron field resulting from a neutron beam thermalized with a graphite moderator must be determined in order to apply the appropriate correction factor to the experimental response matrix selection.[64] Energy-dependent response matrices were calculated for a series of angles and the experimental response matrix used for unfolding is the superposition of the responses of the varying degrees of anisotropy. These angular dependencies were calculated at discrete angles and superimposed as Green's Functions to the solution set. The angular dependence of the neutron field was measured by irradiating neutron foils arranged at 0, 22.5, 45, 77.5, and 90 degree angles with respect to the reactor core face, as shown in Figure 4-9.

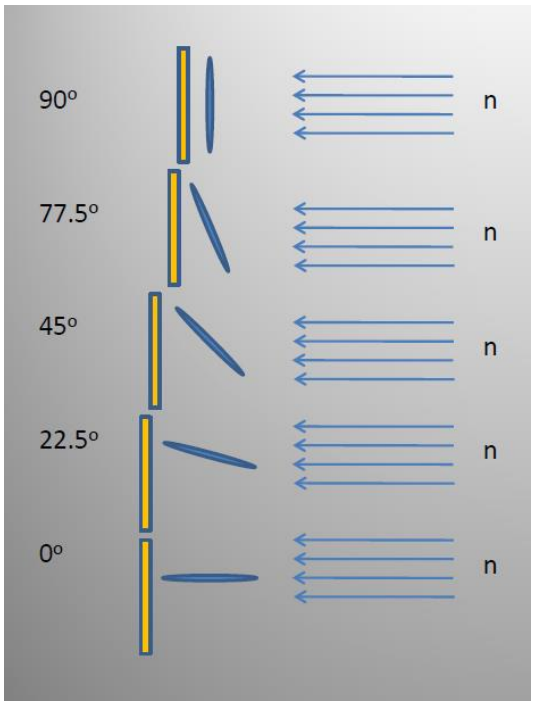

Figure 4-9. Schematic of foil placement to determine angular dependence of the neutron field within the thermal column.

The second correction that must be applied to properly analyze the passive detector response relates to the uniformity of the temporal component of the neutron field throughout the irradiation. Due to the operational nature of the nuclear reactor, a continuous temporal approximation of the reactor power and hence, neutron fluence rate, cannot be applied. The ramp up insertion of reactivity and scram insertion of negative reactivity upon initiation and cessation of the irradiation contribute to a non-uniform neutron field and are not instantaneous. For longer duration irradiations, this uncertainty is relatively small. On the other hand, irradiations of a few minutes are greatly impacted by this ramp up and down. To account for this, a ^{3}He neutron detector was placed in the west beam port experimental facility as a time-integrating power rate meter during the irradiation of the target material and was used to quantify the temporal component of the

neutron fluence rate. Using a piece-wise continuous integration technique, each time bin (binned in 1 s intervals) was used to quantify the temporally-dependent relative neutron fluence rate. Utilizing the power fluctuations recorded by the neutron detector system, the activity responses can be corrected. A sample power history as a function of time is shown in Figure 4-10.

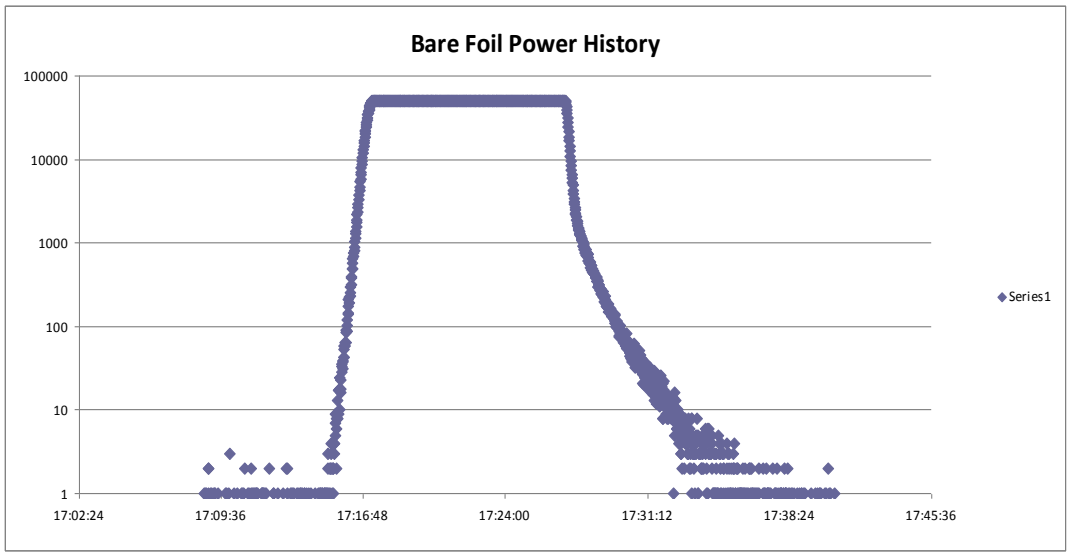

Figure 4-10. Sample power history recorded during the irradiation of detectors in the MUTR thermal column.

The critical concept of few channel neutron spectral unfolding is the use of several selected detector responses (i.e. activation foils) and, through a mathematical process, solving a series of ill-posed problems that result in a multi-channel energy-dependent neutron response. The activation foils themselves do not directly provide the energy-dependent neutron spectra. Each detector is an "integral" detector that has a response which is not unique to only one neutron energy. The output of production rate, (n,γ) reactions, (n,α) reactions, etc. does not provide the energy-dependent response. The

response of a given activation foil, be it moderate and capture or resonance self-shielding, to a given neutron spectrum is given by the first order Fredholm integral equation of the first kind:

$$\dot{P}_i = \int_0^{\infty} R_i(E)\phi(E)dE \qquad i = 1,2,3 \rightarrow N \tag{4-7}$$

where $\dot{P}_i$ = production rate of isotope i from parent x of the ith detector arrangement/position

$R_i(E)$ = response function for the ith detector at energy E

ϕ (E) = energy-dependent neutron fluence rate in n/cm^2/s

This continuous energy distribution form of the Fredholm integral equation can be converted to a more simplistic matrix form of the solution, which can be more easily solved numerically.

$$\dot{P}_i = \sum_{g=1}^{G} R_{i,g} \times \phi_g \qquad i=1,2,3 \rightarrow N \tag{4-8}$$

where ϕ_g = group flux between E_g and E_{g+1} (total measure of neutron fluence between the upper bound energy E_{g+1} and the lower energy bound E_g)

$R_{i,g}$ = multi-group form of the ith detector response

This system can produce a multi-group energy-dependent neutron spectrum. However, this system of equations, namely the number of unknown energy groups compared with

the number of equations (possible unique activation detectors) are such that the matrix equation is underdetermined (i.e. there is no unique solution to the series of equations) because the total number of unknowns (neutron energy bins) outnumbers the number of unique energy-dependent detectors. This is particularly true in the low thermal energy neutron region where there are no unique datasets without further engineering work. This is the dominating reason for combining the moderate and capture technique with the resonance self-shielding technique. Each system provides a unique piece of data with a unique energy-dependent response.

The unique energy-dependent response matrix for each foil in the moderate and capture system, as well as the resonance self-shielding system, were calculated using an industry standard, continuous energy, combinatoric geometry Monte Carlo N-Particle transport code, MCNP version 5 (MCNP5). This code has been used in numerous other works to produce the energy-dependent response matrix.[65-67]

The response matrices calculated in MCNP5 were then loaded into a maximum entropy unfolding program, MaxEd-FC33.[68, 69] Since the above Fredholm integral equations are underdetermined, an iterative solution process is seeded initially with a "starting spectrum". There is significant concern over the starting spectrum imparting too much "information" into the unfolding code sets. This is often considered operator influence. A significant effort by the collaborators on this project was put forth to improve the method to generate this starting spectrum, while removing operator influence. The starting spectrum was calculated using a beta test version of a computer code called

RATE. RATE builds off previous work by Dr. Reginatto on a Bayesian Statistical Estimator (BSE) for predicting starting neutron spectra and was completed by Dr. Burgett in early 2008. RATE utilizes the BSE by employing a Monte Carlo Markov Chain (MCMC) statistical analysis of the responses of the detector data. The MCMC and BSE utilize user supplied physical parameters of the system to constrain the initial spectrum used to seed the maximum entropy unfolding technique. The physical parameters are dictated by the physics of the problem. In any given fission environment, there is a distributions of neutrons known as the chi-nu distribution, which resembles a skewed Gaussian. In an environment with a hydrogenous or light isotope moderator, there is a thermal neutron peak which is approximated as a Gaussian. In fast neutron systems such as cosmic, atmospheric, galactic, and accelerator produced neutron sources, there are two high energy evaporation and spallation peaks which are approximated as skewed Gaussian peaks. Lastly, there is a continuum function which is a smoothed trapezoidal shape of neutrons thermalizing from high energies to thermal energies. In the absence of intense resonance absorbers (significant quantitates of Cd, ^{238}U, Ag), the neutron spectrum must be piecewise continuous and smooth.

Table 4-4. Physical parameters used to fit the RATE code starting neutron spectrum.

Feature	Number of Parameters to Fit	Parameters
Thermal Peak	2	Energy, FWHM
Epithermal Continuum	5	Low Energy, Slope, High Energy, Slope, connection slope
Fast Peak	3	Energy, FWHM, skewness
Evaporation Peak	Not Applicable	
Spallation Peak	Not Applicable	

From Table 4-4, it can be seen that the RATE program needs ten detector responses in order to create a piecewise continuous and smooth starting neutron spectrum which is constrained by physics. In the Figure 4-11, note that Gaussians 1-3 were omitted from consideration, as their presence in the RATE code are for specific accelerator-type spectroscopy applications.

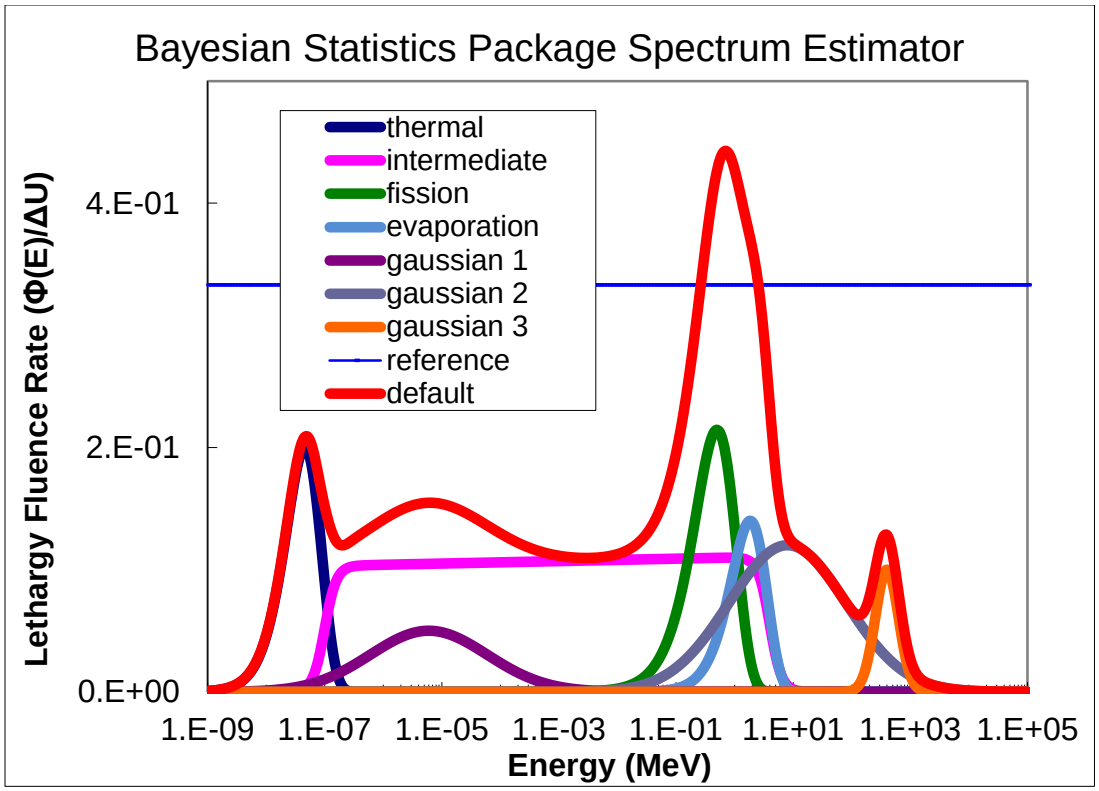

Figure 4-11. Sample starting neutron spectra generated using the RATE code.

The MCNP5 calculated response matrices were prepared for insertion into the MXD_FC33 unfolding code. These matrices were calculated as parallel beams of neutrons as a function of angle with respect to the axis of the detectors. A sample computed response is shown in Figure 4-12. Note the predicted detector response as a function of both incident neutron energy and thickness of moderator between the neutron source and the detector.

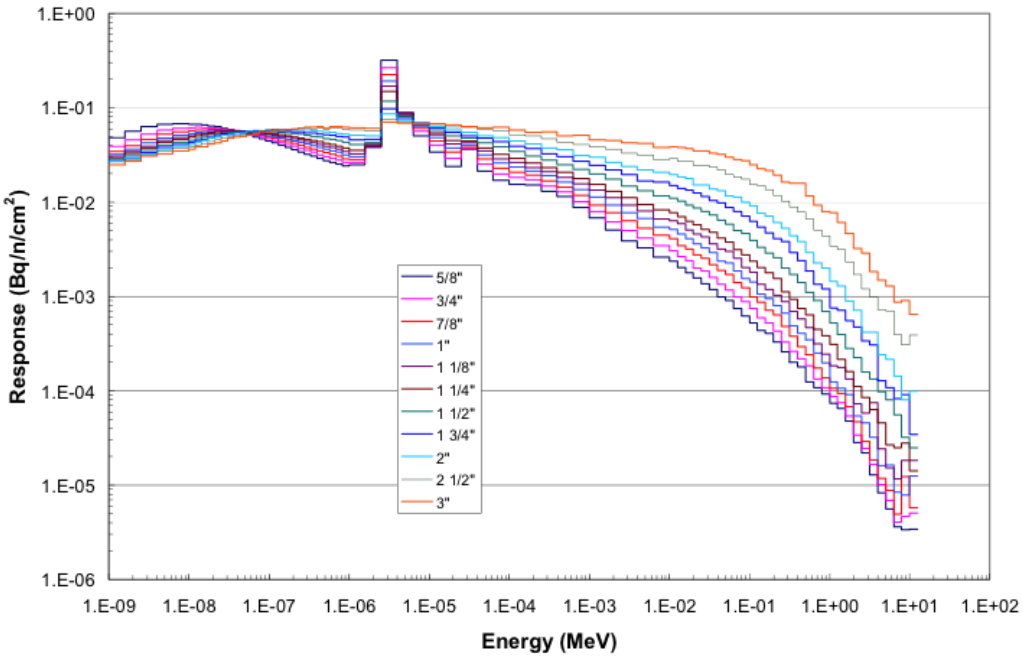

Figure 4-12. Computed energy-dependent neutron spectral responses of the moderate and capture detector system for a parallel beam of neutrons incident on the face of the detector.

The experimentally measured activation rate of the target gold foils as a function of moderator thickness is shown in Figure 4-13. As expected for a highly thermalized neutron field, the activation rate is maximal for the foils closest to the moderate and capture entrance aperture. For a neutron field with a higher proportion of epithermal and fast neutrons, the plot of activation rate as a function of moderator thickness would yield a proportionally higher activation rate for detectors embedded further in the system.

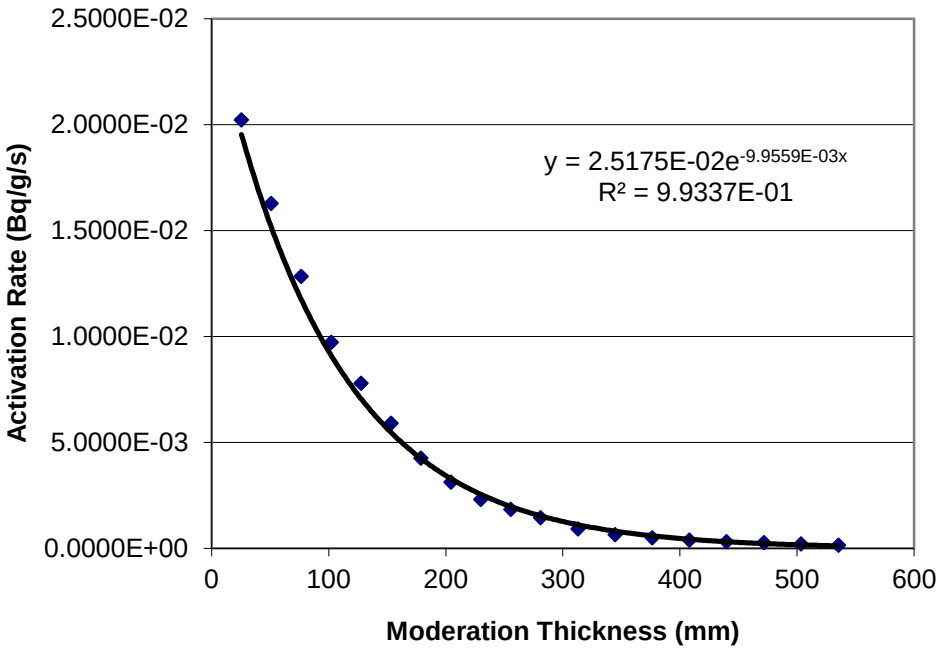

Figure 4-13. Activation rate on the gold foil within the moderate and capture detection system as a function of PMMA moderator thickness.

The starting spectrum from the RATE package and the calculated response matrices from MCNP5 are loaded in MXD-FC33. The problem is then iterated until a smooth response with an overall uncertainty of less than 1% is achieved. This is determined from the chi-squared value of the neutron spectrum and R_{calc}/R_{meas}, and minimizing these values to 1. R_{calc}/R_{meas} is a measure of the calculated response of detector I, if one integrates the unfolded neutron spectrum against the energy-dependent cross section versus the measured value. If the spectrum were perfectly precise, the result would be 1 for every detector. However, this is never the case and the result is usually minimized to within 1%.

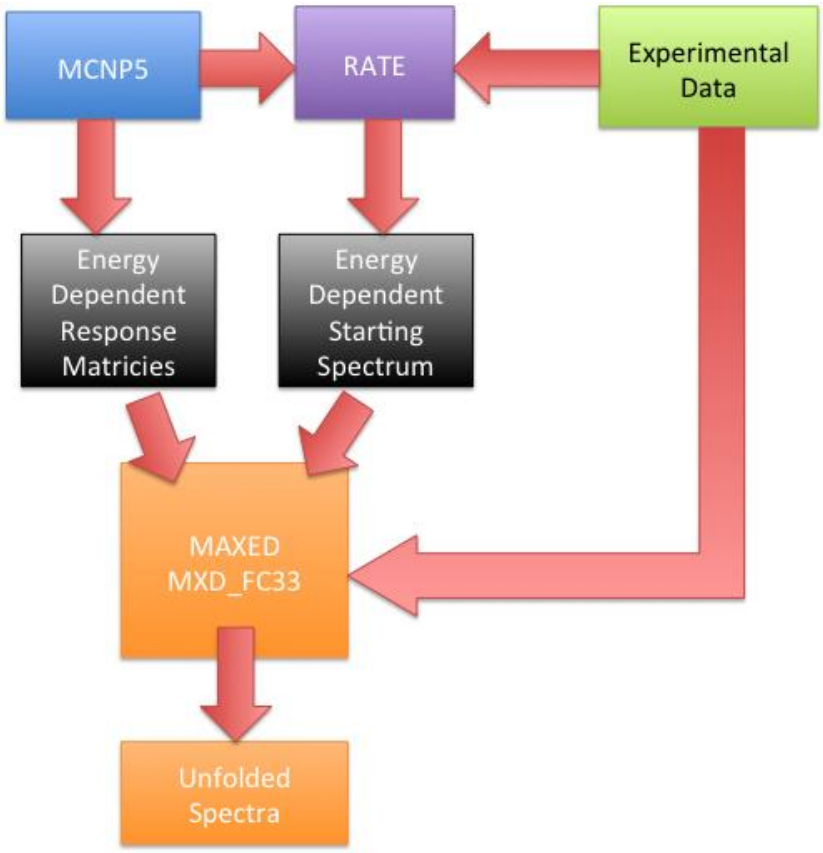

Figure 4-14. Flowchart depicting the progression through MCNP5 modeling to RATE starting spectrum creation, response matrix insertion, MAXED operation, and the resulting unfolded neutron spectrum.

Independent of the detector modeling and experimental analysis, the neutron spectrum within the MUTR thermal column was modeled with MCNP/MCNPX. A detailed description of this model and the uncertainties associated with determination of the neutron fluence rate can be found in the dissertation of Dr. Mohamed.[70]

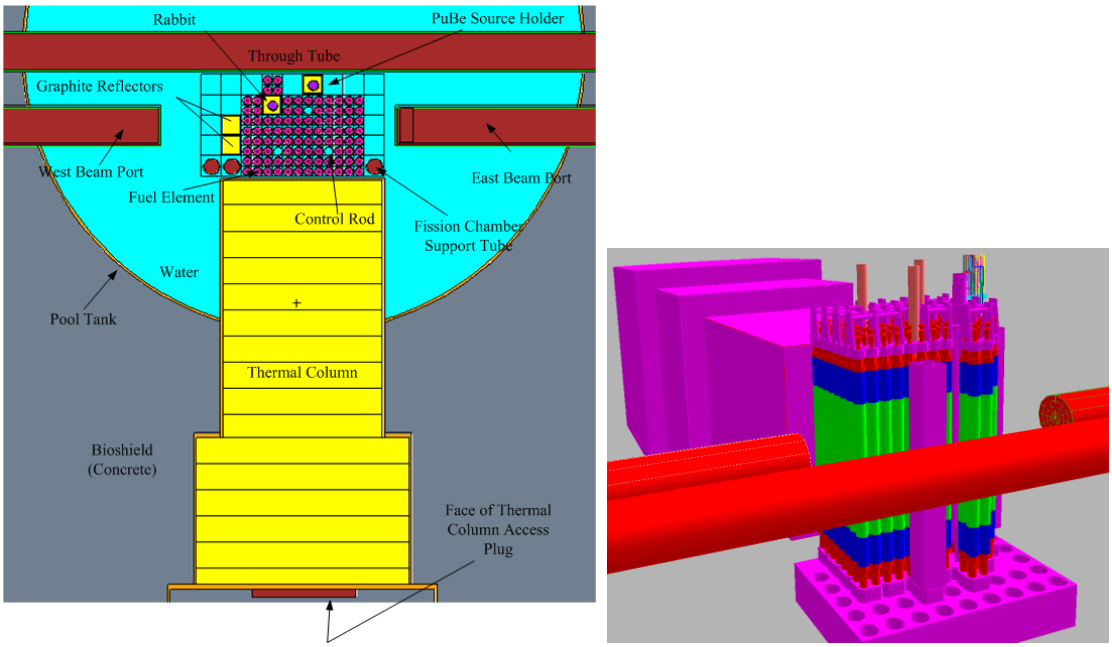

Figure 4-15. MNCP model of the MUTR core and experimental facilities.

In the results section of this chapter, the unfolded neutron spectra generated from the foil activation technique and MCNP model of the MUTR are discussed.

As a point of clarity, it is important to note that there are two distinct MCNP models discussed in the preceding section. The first MCNP model is utilized by the MAXED software package to quantify and unfold the neutron spectrum in conjunction with the experimentally measured detector responses and RATE starting spectrum. The MCNP model simulates the detector responses as a function of a continuous spectrum of neutron energies incident upon the detector. The second MCNP model was created to simulate the entire MUTR core and experimental facilities as a whole. The geometries and materials within the core were programmed and predict the behavior of the neutron population from its origin in a fission event to its eventual capture. Based on cross

sectional data for all material within the reactor core and experimental facilities, the fate of the neutron population is predicted at a final region of interest.

4.1.3 Results

The unfolded neutron spectrum generated by passive detector activation was compared to the MNCP calculated spectrum. As shown in Figure 4-16, the neutron lethargy fluence rates for the two methods are in close agreement. The neutron fluence rate within the entire energy spectrum (10^{-9} – 16 MeV) was within 5%, when comparing the experimental measurements with the MCNP/X computed model. Within the < 3 eV neutron energy range, results of the two methods were also within 5%. The third data set in Figure 4-16 depicts the neutron spectrum as measured within the thermal column sample chamber with the steel cover installed. As expected, the steel cover has a significant impact on the fluence rate magnitude at low neutron energies due to the large $1/\sqrt{E}$ dependence of the iron cross sections. In order to provide equivalent total neutron fluence to a sample within the thermal column plug, irradiation times would have to increase by a factor of 1000 should the cover be installed. With this in mind, thermal neutron irradiation of the BNCT target cells was performed without the cover installed.

When unfolding neutron spectra, it is common to replace the energy variable with neutron lethargy, u. Lethargy is defined as a decrease in neutron energy and is a common term used in the reactor physics community. As a neutron collides with material and loses energy, the neutron lethargy increases.

$$u = \ln(\frac{E_o}{E}) \qquad (4\text{-}9)$$

The total neutron fluence rate within a specific incremental lethargy interval is proportional to the neutron fluence rate in the corresponding energy interval, thus providing a means of converting the unfolded neutron fluence rate per unit lethargy into the neutron fluence rate.

$$\varphi(u) = E\varphi(E) \qquad (4\text{-}10)$$

The comparisons were made in lethargy fluence rates primarily because the reference simulations were reported in units of neutron fluence rate per unit lethargy.

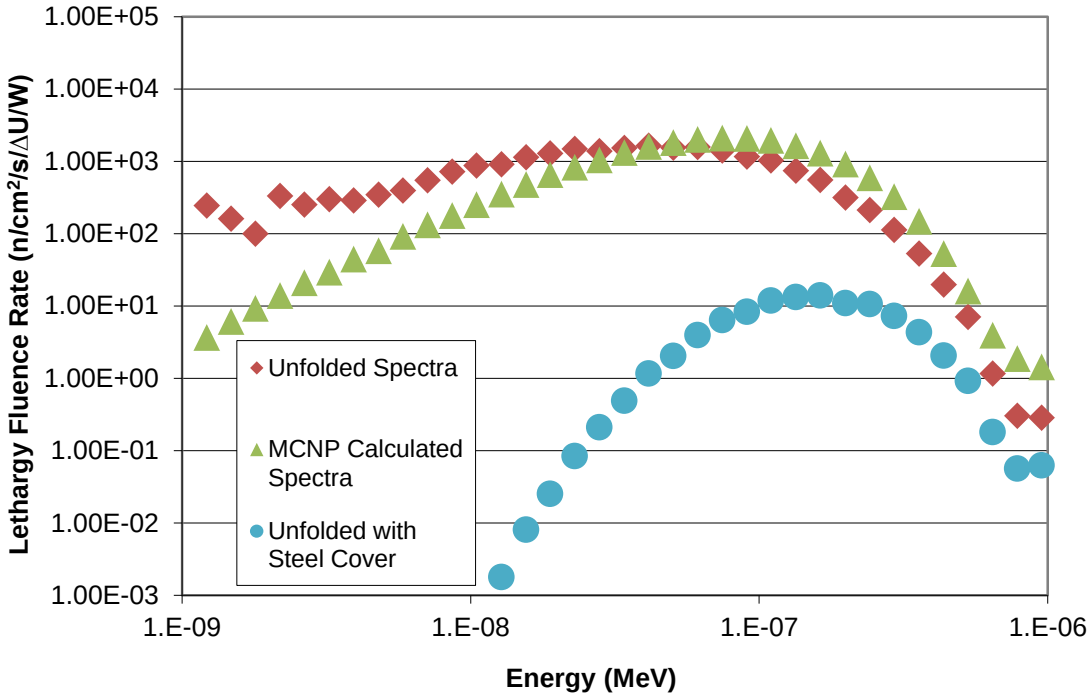

Figure 4-16. Comparison of the experimental unfolded spectrum, MCNP calculated spectrum, and experimental unfolded spectrum with the thermal column shield cover installed.

Figure 4-17 provides a more detailed view of the neutron energy spectrum shift when comparing the MCNP calculated results and the experimental activation unfolding in a log-linear plot. The plot area conversion between lethargy fluence rate and neutron fluence rate is not conserved; however more conveniently presents the data.

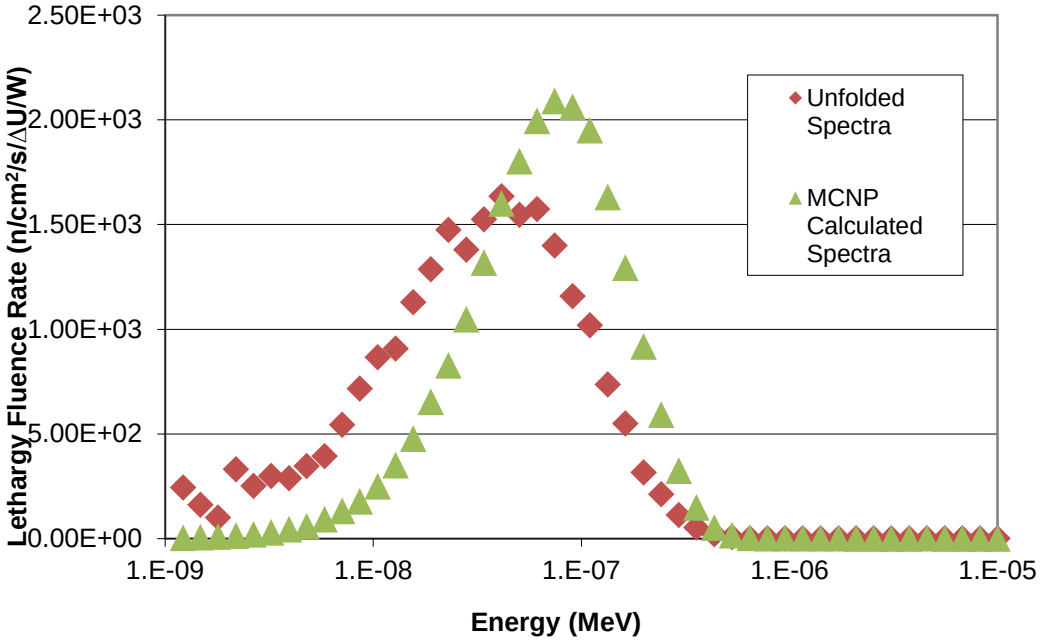

Figure 4-17. Neutron lethargy fluence rate for the MUTR thermal column.

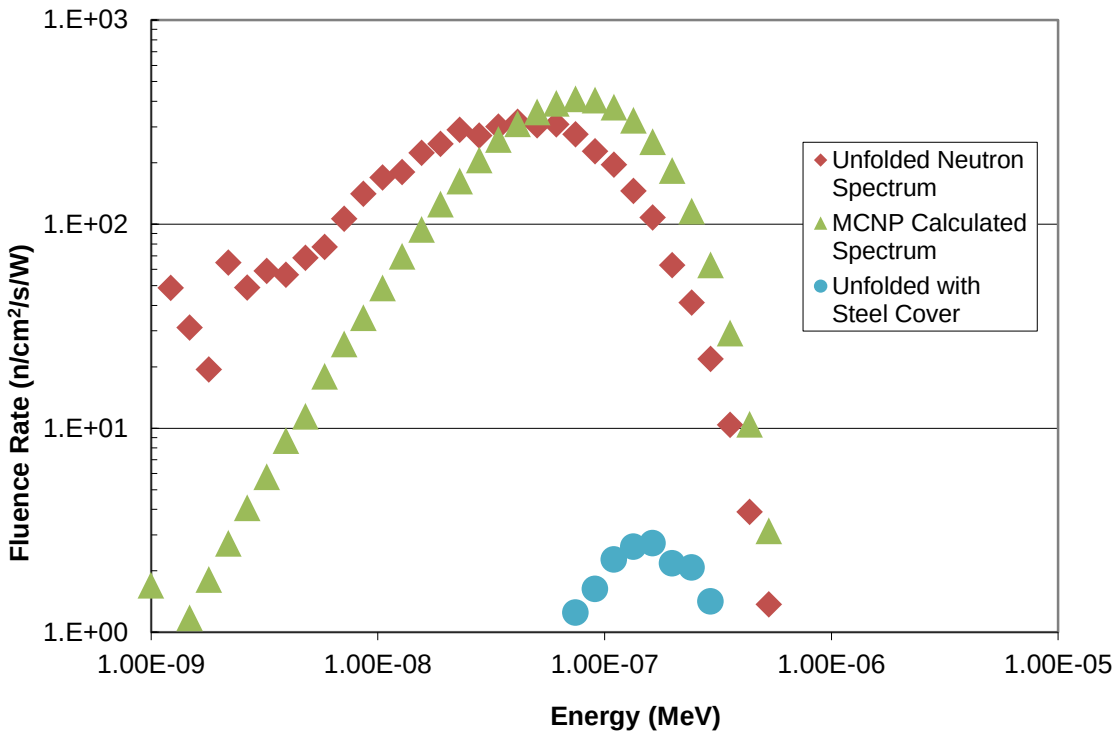

Figure 4-18. Neutron fluence rate spectrum of the MUTR thermal column.

It should be noted that the spectra above show a discrepancy (17% in the 10^{-7}-10^{-6} MeV energy range) between the MCNP calculations and the experimentally obtained results. The experimental results show a slight neutron "cooling" where the thermal peak is shifted slightly to lower energies and is negatively skewed. The presence of a hydrogenous sample chamber surrounding the neutron detectors in the experimental measurement contributed to further thermalization of the neutron field that was not accounted for in the computer model. In addition, neutron scattering within the thermal column experimental facility is largely dependent on the molecular motion of hydrogen, whereby small discrepancies in temperature can shift the Gaussian distribution of thermal neutron energies. These sources of error are present when evaluating narrow energy

bands, however, integral neutron fluences over larger energy regions decrease this uncertainty.

The thermal neutron (< 3 eV) fluence rate at 250 kW in the sample chamber of the thermal column experimental facility of the MUTR is 8.69×10^{8} n/cm^2/s. Thermal neutrons represent 94.6% of all neutrons within the sample chamber. This thermal neutron fluence rate is sufficient to deliver a thermal neutron fluence of approximately 1×10^{12} n/cm^2 in a 20 minute irradiation within the sample chamber.

Uncertainty in the experimental unfolding of the neutron spectrum is dominated by measurement uncertainties associated with detector analysis. Radioactivity decay schemes, determination of target atoms in a foil/wire, energy calibration of the multi-channel analyzers, irradiation and delay times, and cross sectional data all provide their own sources of uncertainty. The IQU_FC33 software package within MAXED permits error propagation throughout the deconvolution process. The relative error in spectral unfolding is estimated to be less than 3%. The experimental unfolding process was performed using NIST-calibrated ^{252}Cf , D_2O moderated ^{252}Cf, and ^{241}AmBe sources and yielded a response within 2% of the accepted value. Further discussion of neutron spectrum unfolding uncertainty is provided by Dr. Burgett.[71] Techniques utilized to minimize uncertainty are discussed in Section 4.1.2.

4.2 Modified Ion Chamber Measurements of Thermal Neutrons

4.2.1 Introduction to Ionization Chambers

Ionization chambers are a type of detector used to measure the direct ionization of gas. As charged particles travel through a gas, positive ions and free electrons (ion pairs) formed in the gaseous molecules are collected on electrodes within the ionization chamber. The electric field in the ionization chamber is created by a voltage potential imposed between the two electrodes. As the ion pairs are collected on the electrodes of opposing polarity, an electrometer is utilized to measure the current within the chamber.

In order for ionization to occur, the incident charged particle must impart sufficient energy to dissociate electrons from the shells of the gas molecule. The magnitude of energy required for the ionization of most gases is in the 10 to 20 eV range. The average energy lost by a charged particle as it travels through gas per ion pair formed, known as W-value, is higher than the ionization energy of the specific gas. This phenomenon is explained by the various mechanisms of energy distribution within the gas. For example, a charged particle may lose energy through an excitation interaction prior to the formation of an ion pair. In this case, the initial energy of the incoming particle must, at a minimum, equal the sum of the energies imparted in the excitation and ionization events. Table 4-5 provides W-values for various gases used in ionization chambers.

Table 4-5. Summary of various W-values for common ionization chamber gases. [72]

	W-value (eV/ion pair)	
Gas	Fast Electrons	Alpha Particles
He	32.5	31.7
H_2	38.0	37.0
N_2	35.8	36.0
Air	35.0	35.2
O_2	32.2	32.2
CH_4	30.2	29.0

A cavity ionization chamber consists of a solid structure surrounding a gas-filled volume. Within the field of cavity chambers, a fully guarded thimble-type chamber is designed with a cylindrical wall (0.1-3 cm^3 volume) surrounding a gas-filled volume and ion collector, as shown in Figure 4-19. A high voltage potential is applied between the chamber wall and ion collector which provides a signal to the electrometer.

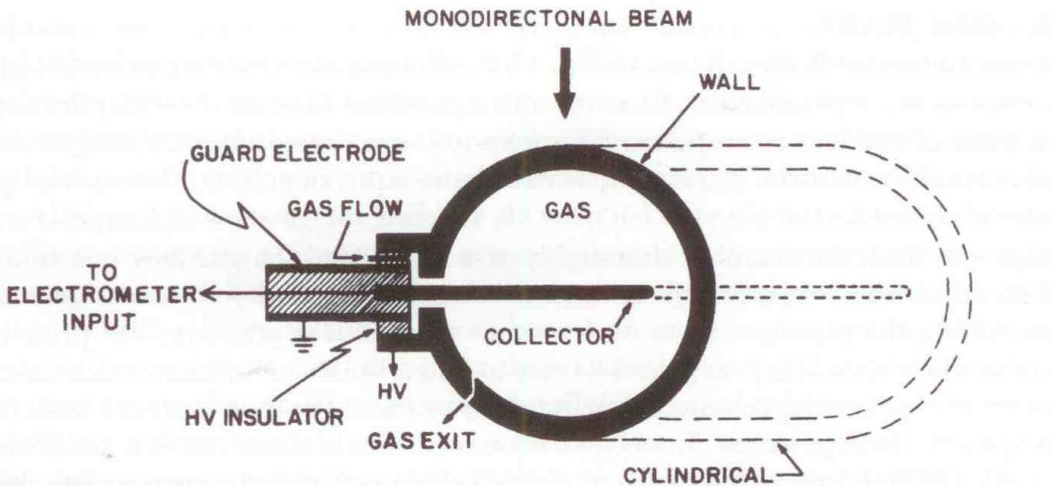

Figure 4-19. Schematic of a fully guarded thimble-type cavity ionization chamber. [73]

4.2.2 Materials and Methods

The measurement of thermal neutron capture by ^{10}B within the MUTR thermal column was investigated with a pair of Exradin ion chambers from the Fermilab Fast Neutron Therapy facility.[74, 75] The ion chambers are Spokas thimble-type with a collecting volume of 0.5 cm^3 and A150 plastic wall material. A150 plastic is designed to simulate the International Commission on Radiation Units and Measurements (ICRU) representation of soft tissue response to irradiation with photons and neutrons of varying energies. The composition of A150 plastic by weight fraction is 10.1% H, 77.6% C, 3.5% N, 5.2% O, 1.7% F, and 1.8% Ca. The two ion chambers are structurally equivalent; however, the wall material of one chamber is loaded with 1000 ppm natural boron (184 ppm ^{10}B). The ion chambers were filled with air and +400 V potential was applied to each during the irradiation. A Keithley 617 electrometer was used to measure the current formed in each chamber.

Within each ion chamber, ion pair formation is the result of interactions between photons, neutrons, and charged particles. For the two ion chambers, photons and fast neutrons produce ion pairs through equivalent interactions. Specifically, recoil nuclei and ions from fast neutrons and secondary electron formation from incident photons and charged particles result in ionizations within the chamber volume. However, the response to thermal neutrons varies between the borated and non-borated chambers. In the borated chamber, a majority of the ionizations are the result of the ions emitted in the $^{10}B(n,\alpha)^7Li$ and $^{14}N(n,p)^{14}C$ reaction. The non-borated ion chamber experiences the same nitrogen

capture reaction with thermal neutrons, but does not contain the boron atoms necessary for production of α particles and ^{7}Li nuclei.

The thermal neutron dose enhancement attributed to the $^{10}B(n,\alpha)^{7}Li$ reaction within the MUTR thermal column was investigated for reactor power levels ranging between 50-250 kW. For each power level, charge collected over 30 seconds was measured in triplicate. The range of power levels provided information about both the presence of thermal neutrons within the thermal column, as well as an indication of the proportional increase in thermal neutrons as reactor power was increased.

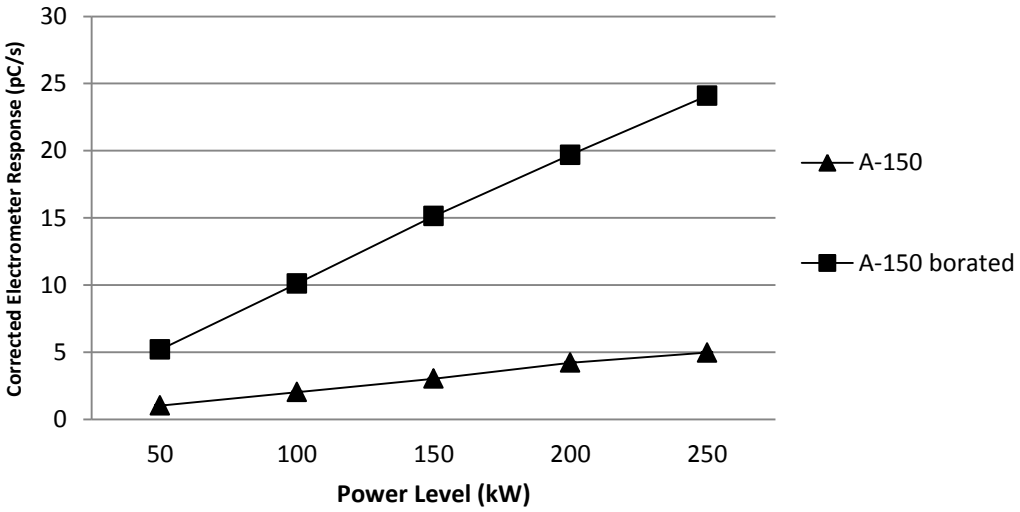

Figure 4-20. Ion pair formation as a function of reactor power for the standard A150 and boron-doped chambers. As reactor power increases, the dose enhancement from boron capture of thermal neutrons remains constant at approximately five times the non-borated response. 30 second measurements were taken in triplicate at each power level. Data points represent the average of n=3 with the RSD <2% for all measurements.

To ensure that the ion chambers have an equivalent response to photons, the chambers were tested in the University of Maryland Gamma Cell. The Gamma Cell provides 1.17

and 1.33 MeV γ–rays emitted from the 2.1 kCi ^{60}Co source. The chambers were placed 91 cm (35.8 in.) from the source top hat. Charge collected over a 30 second interval was measured in triplicate. The responses of the two ion chambers were within 3%, and the variation can largely be attributed to the volume discrepancy between the two chambers.[75]

4.3 Ion Chamber Measurements of Gamma Ray Radiation Field

4.3.1 Gamma Field Dosimetry

The Bragg-Gray cavity theory states that the energy deposited within a gas-filled cavity, assuming the cavity is sufficiently small such that it does not change the distribution of electrons in the medium without the presence of the cavity, results solely from the electrons passing through the cavity itself. This assumption lends to the following equation:

$$E_v = J_v * W * \rho \qquad (4–11)$$

where E_v = energy absorbed per unit volume of the medium

J_v = ionization per unit volume produced in the gas

W = average energy lost by the secondary electrons per ion pair formed in the gas

ρ = ratio of the stopping power of the medium and gas for secondary electrons

The total charge collected by the ion chamber, Q, is directly related to the fill gas within the chamber cavity. The ratio of ionizations in two gases (x and y) can be determined by the following equation[76]:

$$Q_x/Q_y = (S/\rho)_x/(S/\rho)_y * W_y/W_x * \rho_x/\rho_y \qquad (4\text{-}12)$$

where $(S/_r)$ = mass stopping power of the gas

Temperature and pressure must be accounted for when comparing detector responses from the calibration environment to the environment of the experimental measurements. The correction factor, F, for temperature and pressure is calculated by:

$$F = \frac{(273+T)}{295} * \frac{760}{P} \qquad (4\text{-}13)$$

where T = temperature, ^oC

P = pressure, mm Hg (torr)

It is important to note that the relative humidity is not included in the correction factor. This is because the detector response is nearly uniform in the humidity range of 15-80%.[77]

The air kerma calibration coefficient, N_K, for a specific ion chamber is the quotient of the photon kerma, K_{air}, at the location of the center of the chamber to the charge collected

from the chamber, corrected to the density of the air at 1 atm and 22°C. The ion collection efficiency, A_{ion}, is determined using the following equation[78]:

$$A_{ion} = 4/3 - (1/3 * I_1/I_2) \qquad (4\text{-}14)$$

where I_1 and I_2 = ion currents at nominal (300 V) and half (150 V) potential

4.3.2 Materials and Methods

The absorbed dose from γ–rays within the thermal column of the MUTR was measured with an IC-18G ion chamber (Far West Technology, Goleta, CA). The IC-18G is a graphite walled 0.1 cm^3 cylindrical ion chamber with a wall density of 300 mg/cm^2 and thickness of 0.064 cm. Calibration of the ion chamber was performed to NIST-traceable standards in a ^{60}Co field at the University of Wisconsin Accredited Dosimetry Calibration Laboratory. Details of the calibration are found in Table 4-6.

Table 4-6. NIST-traceable calibration values and parameters for the IC-18G ion chamber.

Field Size	10 x 10 cm at 100 cm distance
Collecting Electrode Bias	+300 V
Pre-Irradiation Leakage	-5.0×10^{-15} A
Calibration Uncertainty	1.5%
Ion Collection Efficiency (A_{ion})	1.000
Air Kerma Calibration Coeff.	2.337×10^{8} Gy/C
Exposure Calibration Coeff.	2.659×10^{10} R/C
Temperature	19.2 ^{o}C
Pressure	736.5 Torr
Relative Humidity	22%

The ion chamber was positioned in the thermal column of the MUTR during a 250 kW steady-state operation. CO_2 gas flowed through the chamber volume at 1.5 cc/min.

4.3.3 Results

The results of the gamma dose rate measurements within the MUTR thermal column at 250 kW are summarized in Table 4-7.

Table 4-7. Gamma ray dose measurements within the MUTR thermal column at 250 kW.

Thermal Column MUTR 250 kW		
Nk(g)co_2	1.51E+08	(Gy/C)
Temp	19	^{o}C
Pressure	766.9	Torr
PT Correction	0.988669	
ECP	1.001	
Chamber Current	6.32E-11	(C/min)
Dose Rate	9.43E-03	(Gy/min)

Measurements of the charge collected by the ionization chamber over a 30 second period were performed in triplicate at 250 kW. The average response was 0.0632 $\pm$ 0.004 nC/min.

Chapter 5: Liposomes

Lipids are organic compounds that contain esters of fatty acids and are usually insoluble in water. There are many categories of lipids, including: glycerolipids, glycerophospholipids, sphingolipids, etc. The most common lipids found in cell membranes are phospholipids known as phosphatidylcholines (PC). PCs contain a choline headgroup (hydrophilic) and glycerophosphoric acids bonded to a fatty acid (hydrophobic); and are capable of forming lipid bilayers. When lipids are dispersed in an aqueous solution, vesicles containing an inner volume of aqueous solution surrounded by a lipid bilayer membrane are spontaneously formed. These vesicles are known as liposomes, as shown in Figure 5-1. Within the liposome membrane, a bilayer of lipids forms due to the hydrophobic interactions of the fatty acid chains and the hydrophilic nature of the choline headgroups.

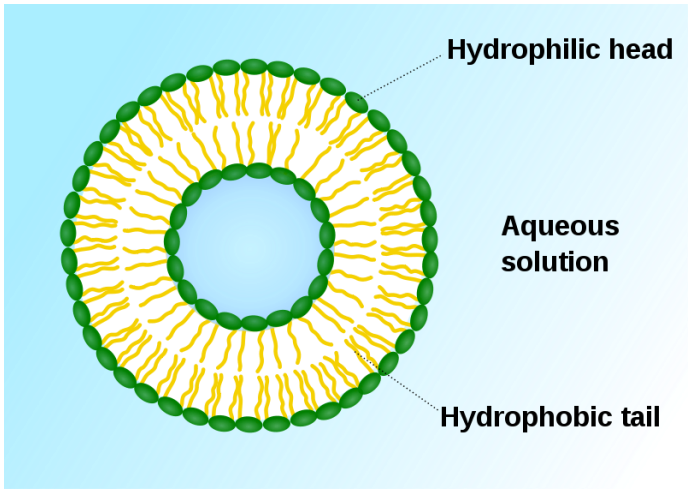

Figure 5-1. Schematic diagram of a liposome illustrating the aqueous inner and outer regions surrounding the lipid bilayer.

As a method of targeted drug delivery, liposomes are capable of facilitating introduction of both hydrophilic and hydrophobic compounds. In the former instance, the drug is added to the aqueous solution and mixed with the lipids during hydration. Hydrophilic compounds are encapsulated in the aqueous inner volume of the liposome and remain within the liposome vesicle until delivery to the target site. In the latter instance, hydrophobic compounds are mixed in with the lipids and entrapped within the lipid bilayer. Due to the hydrophobic nature of BCH, loading into the liposomes occurs during the lipid dissolution phase.

While the formation of liposomes is a spontaneous result of mixing lipids with aqueous solutions, size, structure, and encapsulation efficiency can be greatly impacted by the method of liposome preparation. The various means of preparation rely on a difference in methodology for dispersing the lipids within the aqueous solution and are divided into physical dispersion, two-phase dispersion, and detergent solubilization.[79] Based on previously reported success for intracellular delivery of BCH, compatibility with biological molecules, ease of use, and desired liposome size distribution, the French pressure cell procedure of mechanical dispersion was chosen.[42-44, 79] The French pressure cell was one of the first methods developed for preparing liposomes[80, 81] and facilitates the conversion of large multilamellar vesicles (LMVs) to intermediate-sized unilamellar vesicles (IUVs) and small unilamellar vesicles (SUVs) by pressurizing a liposome solution and slowly forcing the solution through a small outlet orifice. As the solution passes through the orifice, the shear forces fracture the structure of the LMVs and allow the lipid fractions to spontaneously recombine in the aqueous solution.

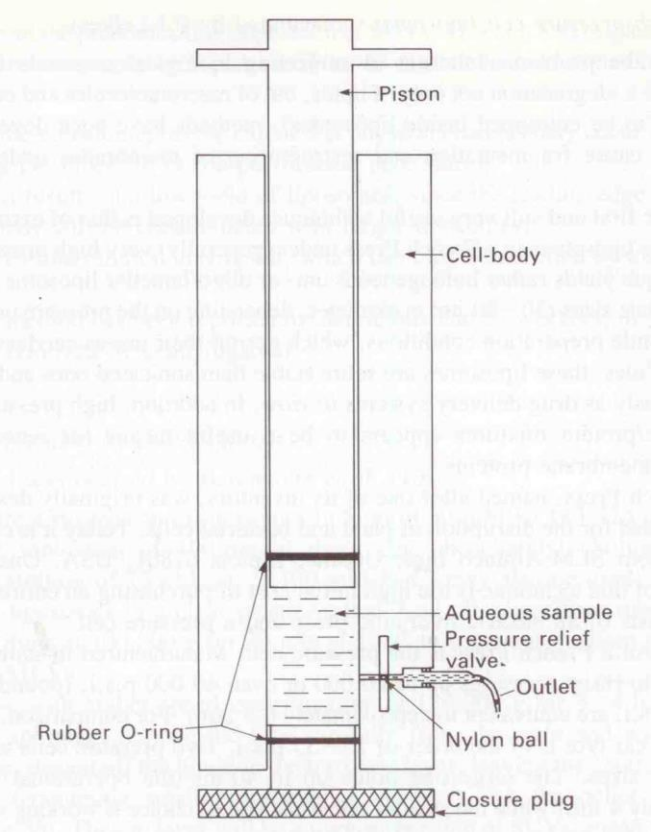

Figure 5-2. Schematic diagram of the French pressure cell used to convert LMVs to IUVs and SUVs.[79]

Throughout this fractionation and reformation, the LMVs are transformed into IUVs and SUVs. This process relies heavily on extreme force applied to the LMVs and because of this is, it vital that the solution be subjected to high pressure. The final size of the reformed liposomes is directly proportional to the pressure exerted as the solution passes through the exit orifice, as shown in Figure 5-3.

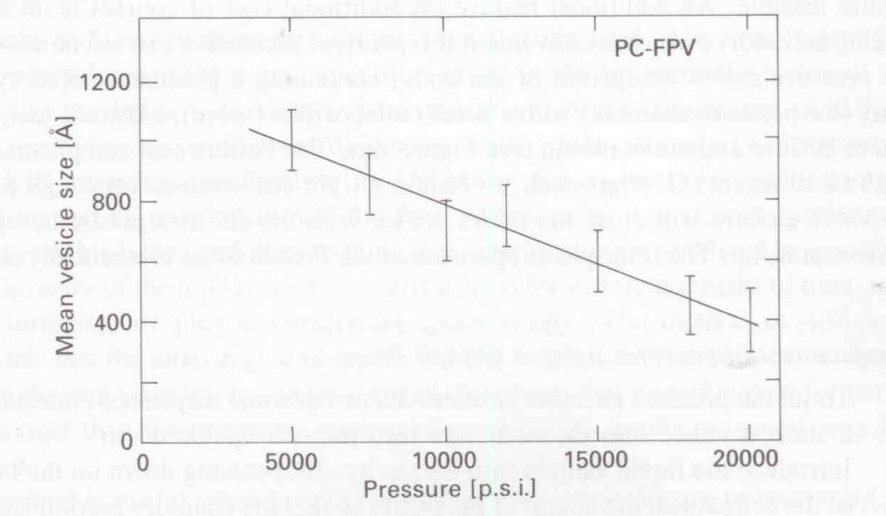

Figure 5-3. The direct relationship between pressure exerted on the liposome at the exit orifice of a French pressure cell and the mean vesicle size. As pressure is increased, the mean vesicle size decreases.[79]

5.1 Synthesis of Liposomes and Size Reduction

Liposomes were prepared using 1,2-dipalmitoyl-*sn*-glycero-3-phosphocholine (DPPC) (850355P, Avanti Polar Lipids Inc., Alabaster, AL), cholesterol (CHOL) (700000P, Avanti Polar Lipids Inc., Alabaster, AL), and cholesteryl 1,12-dicarba-closo-dodecaboranel-carboxylate (BCH). 55.0 mg DPPC, 9.8 mg CHOL, and 5.5 mg BCH were added to a 25 mL round-bottom flask. The 0.33:1 cholesterol:phospholipid molar ratio was selected based on previous experiments for incorporation of BCH into liposome formulations, and research involving the incorporation of lipophilic drugs into lipid bilayers.[79, 82, 83] The lipids were then dissolved in 6 mL of 2:1 (v/v) chloroform:methanol (Sigma-Aldrich, St. Louis, MO). The lipid mixture was dried using a rotary evaporator (Rotavapor R-210, Buchi Labortechnik AG, Switzerland) and heating bath (B-491, Buchi Labortechnik AG, Switzerland) set to 60 rpm for approximately one hour at 60^{o}C. Once a thin film of dried lipid had formed along the walls of the flask, 10

mL of PBS (pre-heated to 60°C) with 500 mg of glass beads (11-312C, Fisher Scientific, Pittsburgh, PA) were added to the flask and stirred in a water bath at 60°C and 120 rpm for two hours. Throughout the hydration process, the mixture was kept at 60°C to avoid falling below the phase transition temperature (T_m) of the lipids.

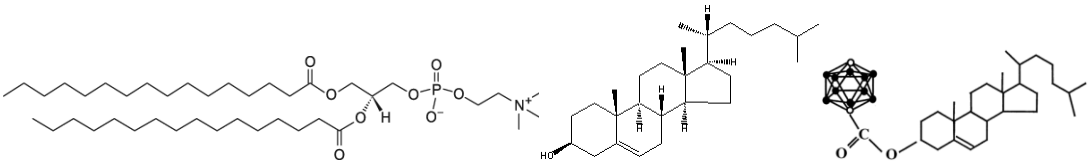

Figure 5-4. Chemical structures of DPPC, cholesterol, and BCH.

The hydrated liposome formulation contains LMVs with a large size distribution. In order to reduce the size of the LMVs and create IUVs and SUVs, the formulation was processed by high-pressure homogenization (EmulsiFlex-B3, Avestin Inc., Ottawa, ON, Canada). In this process, 3.5 mL of liposome formulation was injected into the sample chamber and the chamber was sealed by closing the plug and set cap. The unit was connected to a pressurized air source and set to an inlet pressure of 100 psi using the built-in regulator. This correlates to a hydraulic pressure of 20,000 psi within the sample chamber, as reported by the manufacturer. The homogenizer was placed in "pump" mode and the sample chamber was pressurized. Slowly, the set cap was released to allow the liposome formulation to pass through the discharge tubing. This process results in a slow, steady release of the formulation from the sample chamber, with a manufacturer recommendation of approximately 1-2 minutes to release 3.5 mL of sample solution. Upon completion of the release, the set cap was tightened and the unit was placed in "suck" mode. Releasing the set cap slowly draws the liposome formulation back into the

sample chamber. This process was repeated for 1-2 cycles. Liposomes were stored at 4^{o}C until use.

Figure 5-5. Avestin B3 high-pressure homogenizer.

5.1.1 Lipid Oxidation

Lipid oxidation is a degradation process whereby a hydrogen atom is removed from a carbon atom adjacent to a double bond, resulting in the formation of a free radical (alkyl radical). In the presence of oxygen, this alkyl radical propagates to form a peroxyl radical. Peroxyl radical interaction with another hydrogen atom of a neighboring lipid yields a lipid peroxide molecule and lipid radical, which in turn undergoes the propagation step of peroxyl radical formation. In the absence of radical scavengers, termination of the radical formation occurs when the increased presence of free radicals is sufficient such that the probability of two radicals interacting together results in a radical-radical reaction. The lipid oxidation process is shown in Figure 5-6.

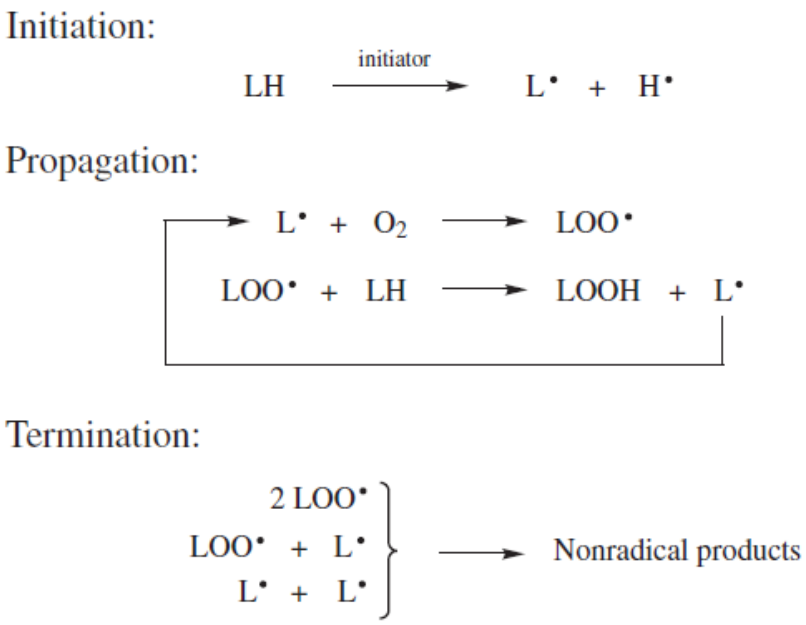

Figure 5-6. Mechanism of autoxidation in unsaturated fatty acids.[84]

Unsaturated fatty acids are most susceptible to the initiation of an alkyl radical due to the delocalization of the hydrogen atom along the fatty acid chain. Because of this, saturated lipids are far less prone to oxidation. Oxidation of cholesterol and cholesteryl esters is possible given the unit of monounsaturation within the carbon 5,6 positions, and occurs by a similar mechanism.

Oxidative damage to the cholesterol and cholesteryl esters can result in the presence of epoxides, peroxides, and diols, as well as decreased stability of the liposome structure. It is important to note that liposome integrity is less critical in drug delivery systems which incorporate the lipophilic drug within the lipid bilayer. Degradation of the lipids by oxidation often results in the leakage of aqueous material from within the encapsulated bilayer, and therefore reduces the efficiency by which encapsulated, aqueous drugs are

delivered to the target system. Lipophilic drugs incorporated in the lipid bilayer, on the other hand, are less likely to release from the liposomes as a result of membrane instability.

The selection of DPPC as the principle lipid within the BCH liposomes minimized the potential for oxidative damage due to the saturation of the fatty acid chains. However, the presence of cholesterol and BCH warrant caution in storage and liposome preparation to minimize oxidation during synthesis of the liposome formulation. Lipids were stored in glass containers at -20^{o}C in the dark. Secondary containers with desiccant were utilized during storage and upon removal for liposome preparation. Dry lipids were warmed to room temperature prior to dissolution in the lipid mixture. Once hydrated, the liposome formulation was sealed and stored in the dark at 4^{o}C prior to incubation in the cell medium. Liposome formulation was prepared no more than 24 hours prior to incubation with the cell cultures. Size analysis with dynamic light scattering of the liposomes did not reveal any change in structure or size after one week in storage. In addition, abiding by proper storage protocol yielded no change in the physical appearance or texture of dry lipids in storage.

5.2 Liposome Size Analysis

5.2.1 Introduction to Dynamic Light Scattering

Size analysis of BCH-containing liposomes was accomplished using light scattering. This technique relies on the Rayleigh scattering of light by a molecule or particle as light passes through and induces a momentary dipole. In dynamic light scattering (DLS), also commonly referred to as photo correlation spectroscopy (PCS) or quasi-elastic light scattering (QELS), a photon beam is incident upon particles in suspension and the intensity of the scattered light is measured as a function of time. Movement of the particles in suspension is a result of Brownian motion and leads to time-dependent fluctuations in the scattered light intensity due to the constructive and destructive interference of the surrounding particles. The fluctuations in scattered light intensity are directly proportional to the diffusion rate of the particles in suspension, and are quantified in a second order correlation function:

$$g^{(2)}(\tau) = \frac{<I(t)I(t+\tau)>}{<I(t)>^2} \qquad (5\text{-}1)$$

where $I(t)$ = intensity of the scattered light at time t

τ = delay time.

For short delay times, there is a very high correlation because the particles have not moved significantly from their initial positions in suspension. However, as the delay

time is increased, the correlation decays exponentially as a result of diffusion of the particles. The correlation function is then used to determine the decay rate:

$$g^{(2)}(\tau) = B + \beta e^{-2\Gamma t} \qquad (5\text{-}2)$$

where B = baseline of the correlation function at infinite delay

β = correlation function amplitude at zero delay

Γ = decay rate

t = time

From the decay rate, the diffusion coefficient, D_t, can be derived with the equation:

$$\Gamma = q^2 D_t \qquad (5\text{-}3)$$

where q = magnitude of the scattering vector

$q = \frac{4\pi n_o}{\lambda_o} \sin(\theta/2)$, with n_o the solvent index of refraction, λ_o the vacuum wavelength of the incident light

θ = scattering angle

From the Stokes-Einstein equation, the diffusion coefficient is used to calculate the hydrodynamic radius, r_h, of the particle:

$$r_h = \frac{kT}{6\pi\eta D_T} \qquad (5\text{-}4)$$

where k = Boltzmann's constant

T = temperature

η = viscosity of the solvent

For samples with a broad size distribution of spheres, the correlation function must be solved for each size within the distribution. Therefore, the equation for the correlation function becomes:

$$g(t) = \int G(\Gamma) e^{-\Gamma t}\, d\Gamma \qquad (5\text{-}5)$$

The solution to this equation is quite complex; however, the Non-negatively constrained Least Squares (NNLS) algorithm was developed and is utilized for multimodal size distribution (MSD) analysis.[85, 86] From the MSD solution, the mean diameter can be calculated by:

$$\overline{d} = \frac{\sum d*G(d)}{\sum G(d)} \qquad (5\text{-}6)$$

where d = diameter

G(d) = weighing factor

The width of the distribution is described by the relative variance.

$$Relative\ Variance = \frac{Variance}{\overline{d}^2} \qquad (5\text{-}7)$$

$$Variance = \frac{\sum(d-\overline{d})^2 * G(d)}{\sum G(d)} \qquad (5\text{-}8)$$

The size distribution is measured as average diameters that are weighed by the intensity, number, volume, or surface area of the sample. Each of these diameters provides a means of describing the size distribution of the sample, and therefore the reported value depends on the particular application. The number average provides information about the relative number of particles of a particular size in a polydisperse solution. This is often used to describe liposomes solutions that have a majority population of SUVs mixed with a small population of LMVs.

5.2.2 Results

Liposome formulations were prepared as described in Section 5.1 and the size distribution was measured by dynamic light scattering (ZetaPALS, Brookhaven Instruments Co., Holtsville, NY) at the National Institute of Standards and Technology (NIST). The size distribution was measured for unhomogenized liposome formulation, formulation homogenized for a single cycle, and formulation homogenized for two cycles. The liposome formulation was analyzed with the following conditions: temperature = 25^{o}C, viscosity = 0.89 cp, fluid refractive index = 1.33, and angle = 90^{o}. The liposomes were modeled as a thin shell with the Mie scattering coefficient independent of the shell's refractive index. Given the relative size of the liposome lipid bilayer in relation to the diameter of the liposomes and the same aqueous solution surrounding and within the liposomes, the thin shell assumption is valid. Size analysis was performed using ZetaPlus Particle Sizing Software version 3.93 (Brookhaven Instruments Corp., Holtsville, NY). All runs were one minute in duration and repeated five times.

The unhomogenized liposome formulation contained a large range of liposome sizes, with aggregates visually evident in the formulation. Given the increased scattering intensity of large particles, the polydispersity of the unhomogenized sample could not be quantified. The correlation function is shown in Figure 5-6. When compared to the homogenized samples presented later in this section, the uncertainty in the exponential decay as delay time is increased along with the equilibrium point above the baseline provide further evidence of the presence of many LMVs.

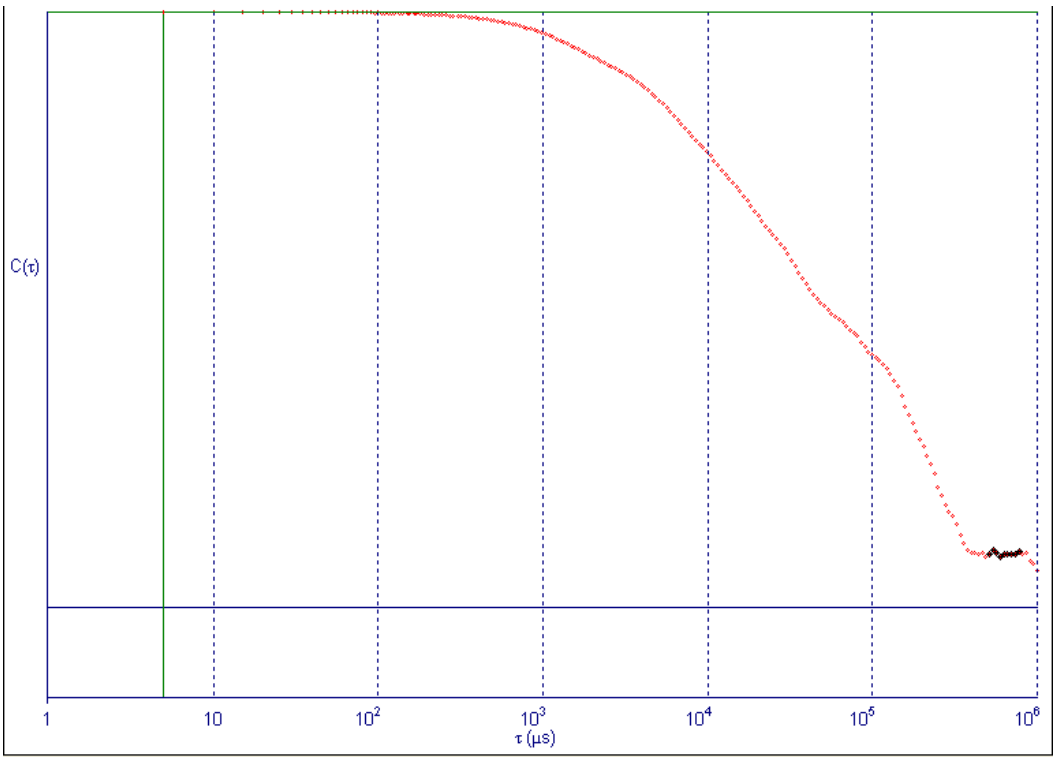

Figure 5-7. The correlation function, C(τ), generated with dynamic light scattering for the unhomogenized liposome formulation as a function of delay time, τ. Note the non-uniform slope within the exponential decay and high baseline equilibrium point.

Following a single pass through the homogenizer at 20,000 psi, aggregation within the liposome formulation decreased significantly. The formulation transformed into a more uniform solution that remained in suspension when allowed time to settle. These visual changes were confirmed when analyzed with DLS. As shown in Figure 5-7, the correlation function has a much smoother exponential decay as the delay time is increased. Additionally, the baseline equilibrium is established closer to zero. Given the higher quality of scattering data, number weighted MSD with NNLS analysis was performed to quantify the liposome size distribution.

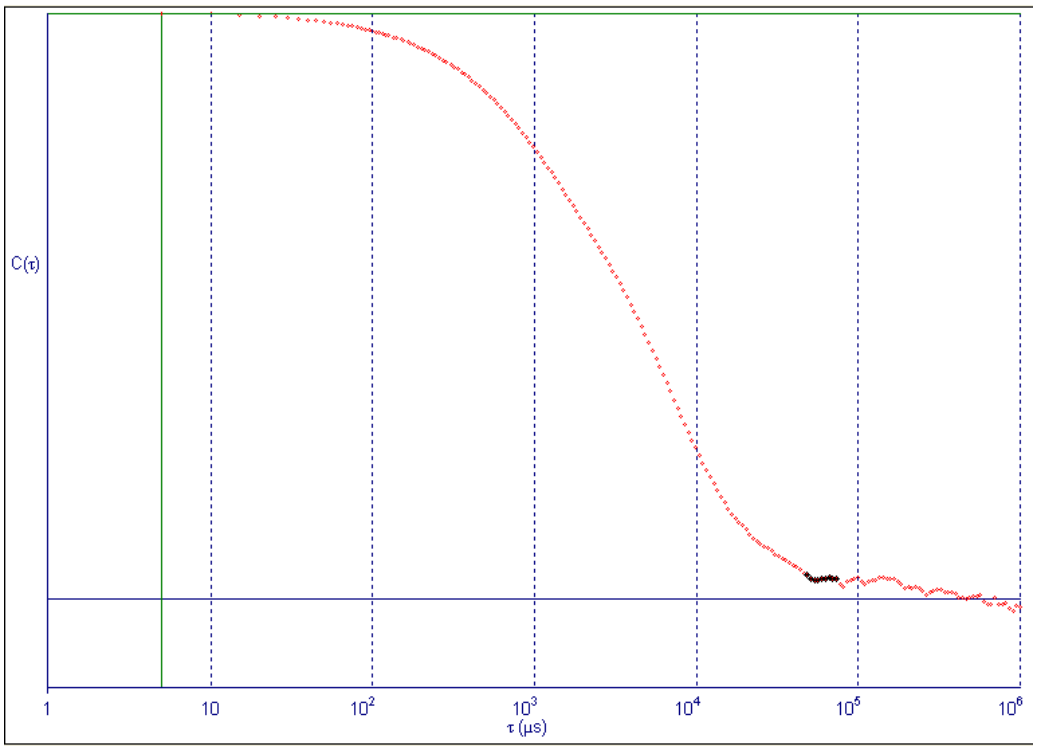

Figure 5-8. The correlation function, C(τ), generated with dynamic light scattering as a function of delay time, τ, following single cycle homogenization of the liposome formulation at 20,000 psi.

A more detailed analysis of the MSD is provided in Table 5-1.

Table 5-1. Number-weighted size distribution of the single cycle homogenized liposome formulation.

Hydrodynamic Diameter (nm)	Relative Abundance (%)
65	0
76.4	19.0
89.9	43.1
105.8	26.3
124.5	10.3
146.4	1.3
172.2	0

The one cycle homogenization resulted in a mean diameter of 98.5 nm with a relative variance of 0.310.

Following a second pass through the homogenizer at 20,000 psi, aggregation within the liposome formulation decreased slightly. As shown in Figure 5-8, the correlation function exhibits a similar exponential decay as the delay time is increased. The baseline equilibrium is less noisy when compared to the single pass.

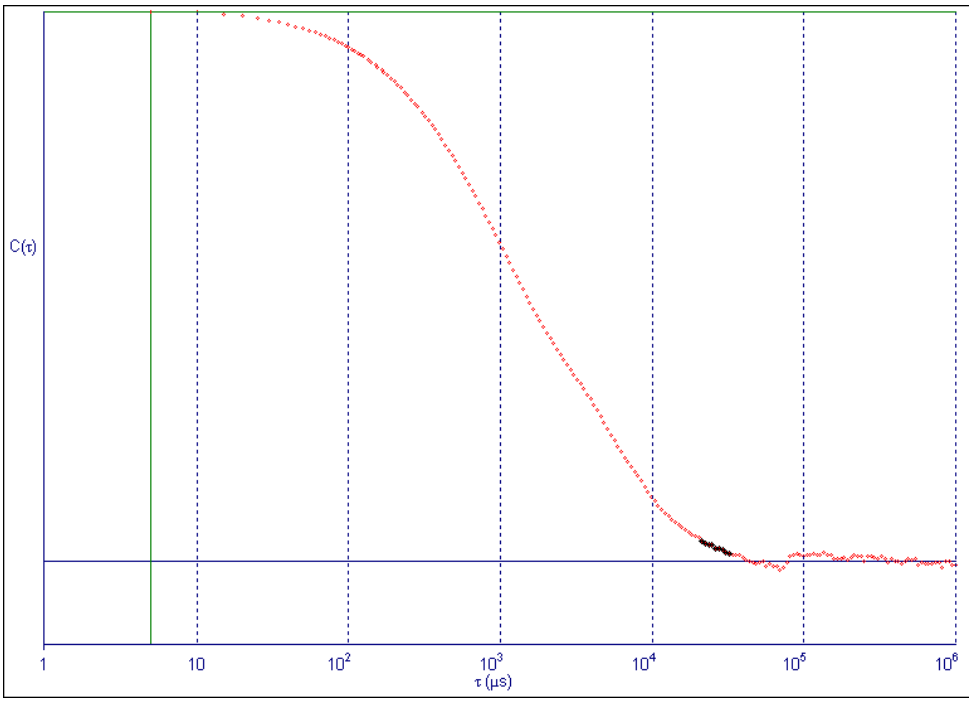

Figure 5-9. The correlation function, C(τ), generated with dynamic light scattering as a function of delay time, τ, following double cycle homogenization of the liposome formulation at 20,000 psi.

A more detailed analysis of the MSD is provided in Table 5-2.

Table 5-2. Number-weighted size distribution of the two cycle homogenized liposome formulation.

Hydrodynamic Diameter (nm)	Relative Abundance (%)
78.8	0
89.8	15.8
102.4	32.3
116.8	27.4
133.2	17.1
151.8	5.8
173.1	1.6
197.4	0

The two cycle homogenization resulted in a mean diameter of 111.5 nm with a relative variance of 0.113.

5.3 BCH Loading Efficiency

Analysis of the liposome formulation following preparation via the thin film hydration method was performed using ICP-MS to measure the BCH loading efficiency. The protocol for ^{10}B analysis in the liposome formulation closely followed the description in Chapter 6. The loading efficiency at two different BCH concentrations was tested, one with 5.5 mg of BCH added to the lipid solution (21.3 μg ^{10}B/mL) and the second with 11.0 mg of BCH added (42.6 μg ^{10}B/mL). The concentration of BCH within the liposome formulation as detected by ICP-MS was 6.3 and 16.8 μg ^{10}B/mL, respectively. Therefore, the loading efficiency for the lower concentration liposome formulation is 29.7% and increases to 39.3% for the higher concentration. The value of 29.7% is comparable to previous report of BCH loading efficiency into a liposome

formulation.[44] After selecting the 5.5 mg BCH liposomes for the BNCT irradiations, the loading efficiency was repeated in triplicate and yielded an efficiency of 32.9 $\pm$ 2.7 %.

To quantify the importance of agitating the liposomes with glass beads during hydration and homogenization, as described in Section 5.1, the impact of each process on BCH loading efficiency was investigated. ^{10}B concentrations in liposome formulations without bead agitation, with bead agitation, and with bead agitation followed by homogenization were studied. The results of each sample are summarized in Table 5-3. The results shown are based on preliminary studies to evaluate the optimal parameters for BCH loading. They are not mean to provide quantitative analysis, and thus no values for uncertainty are provided.

Table 5-3. Loading efficiency of BCH as a function of various preparation schemes.

Liposome Formulation Sample Preparation	**Loading Efficiency (%)**
No glass beads	7
With glass beads	22
With glass beads and homogenization	30

The increase in loading efficiency when glass beads are used to agitate the lipids during thin film hydration is significant. Glass beads increased the loading efficiency by a factor of three, likely due to the strong hydrophobic nature of BCH that is dried on the walls of the round bottom flask prior to hydration in aqueous solution. However, it is important to

note than many glass beads are made of borosilicate glass, a potential source of non-BCH boron. In order to verify that the increase in boron concentration could be attributed to the BCH agitation from the glass wall rather than contamination from the borosilicate glass, the extraction of boron from glass beads was analyzed. Glass beads were placed in DPBS solution for 24 hours at room temperature, DPBS solution for 72 hours at room temperature, 1% nitric acid for 24 hours at room temperature, and 1% nitric acid for 72 hours at room temperature. Following each test, 1 mL of solution was removed and analyzed with ICP-MS. In each sample, the concentration of boron was below the limit of detection.

Chapter 6: Cellular Drug Delivery of BCH

6.1 Cell Culture

Human cancerous prostate PC-3 cells (NCI-PBCF-CRL1435, American Type Culture Collection (ATCC), Manassas, VA) were grown in F-12K medium (Kaighn's modification of Ham's F12 medium supplemented with 2 mM L-glutamine, 1.5 g/L sodium bicarbonate) (30-2004, ATCC, Manassas, VA) and 10% (v/v) fetal bovine serum (FBS) (30-2020, ATCC, Manassas, VA) at 37^{o}C in 5% CO_2 in air. The PC-3 cell line was originally derived from the bone marrow of a 62 year old Caucasian male with grade IV prostatic adenocarcinoma.[87] Cells were grown in Corning® cell culture flasks with vented caps (Sigma-Aldrich, St. Louis, MO). When growing the cells, growth medium was replaced 2-3 times per week and the cells were subcultured when confluency reached 80-90% as determined by microscopic observation.

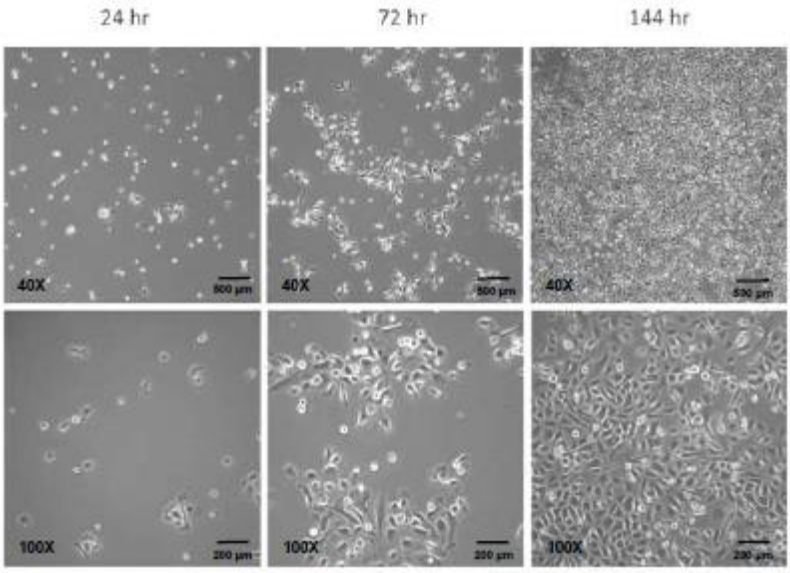

Figure 6-1. PC-3 cells under microscope at various time points with an initial plating density of 3 x 10^4 cells/cm^2.

PC-3 cells were subcultured according to the following protocol (volumes given for T-75 flask): growth medium was aspirated from the cell flask and cell monolayers were washed with 5 mL of Dulbecco's phosphate-buffered saline (DPBS) modified without calcium chloride and without magnesium chloride (30-2200, ATCC, Manassas, VA), 3 mL of 0.25% (w/v) trypsin-0.53 mM EDTA (30-2101, ATCC, Manassas, VA) was added to the flask and incubated for 10 minutes, cell detachment was confirmed under microscope prior to harvesting, trypsin was neutralized with 8 mL growth medium and pipetted up and down for 20 cycles. Approximately 2.5 x 10^6 cells were plated in a new flask and a total volume of 15 mL growth medium was added to the flask.

The growth profile for PC-3 cells is shown in Figure 6-2. The population doubling time (PDT) is approximately 25 hours.[88]

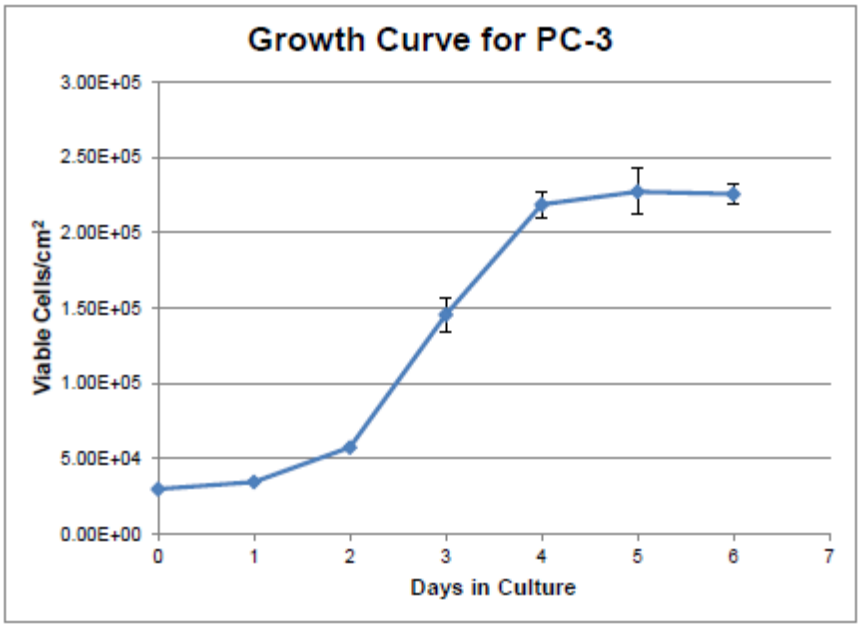

Figure 6-2. Growth profile for PC-3 cells (ATCC).

6.2 Cell Viability

The viability of PC-3 cells after incubation with the BCH-containing liposome formulation was quantified with neutral red, MTS, and LDH cytotoxicity assays. Each assay was analyzed as a means of understanding the disruption of cellular processes for comparison with cells exposed to the BCH-containing liposomes followed by irradiation in a thermal neutron field.

6.2.1 Neutral Red

The neutral red assay system provides a means of measuring living cells through the uptake of vital dye neutral red (toluene red and Basic Red 5).

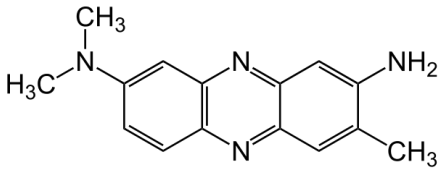

Figure 6-3. Chemical structure of neutral red.

The neutral red method relies on the active transport and incorporation of neutral red dye into the lysosomes by viable cells [89] and has been successfully implemented as a means of testing cytotoxicity in a variety of cell cultures.[90]

Prior to performing the neutral red assay, a cell density-dependent uptake curve was established to determine the proper cell seeding density. The curve was established by plating 0, 1000, 5000, 10000, 50000, and 100000 cells in 100 μL of growth media. Cells were incubated for 24 hours prior to the Neutral Red Based *in vitro* Toxicology Assay Kit (TOX-4, Sigma-Aldrich, St. Louis, MO). Following the incubation phase, 10 μL of 0.33% Neutral Red Solution (N-2889) was added to each well and the plate was returned to the incubator for 2 hours. The media and dye were removed from the wells and the cells rinsed twice with 200 μL of PBS. Following the rinse, 50 μL of Neutral Red Assay Solubilization Solution (N-4395) was added to the wells and kept at room temperature for 10 minutes. The absorbance was measured at 540 nm using a SpectraMax 190 microplate reader with SoftMax Pro 5 GxP software (Molecular Devices Corporation, Sunnyvale, CA). The results are shown in Figure 6-4.

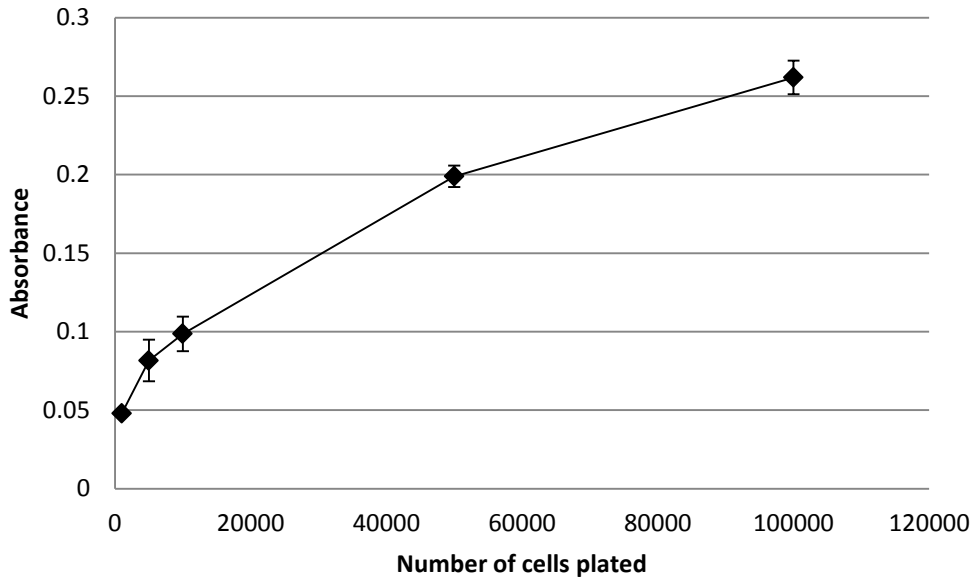

Figure 6-4. Neutral Red uptake curve showing dye concentration in the lysosomes as a function of cells plated. Error bars represent $\pm$ 1 SD.

For the cell cytotoxicity studies, 5000 cells were plated and incubated for 48 hours prior to the addition of liposomes. At the conclusion of the 48 hour incubation period, two different amounts of liposome formulation were added to the wells. For the 1x concentration, 7.7 μL of liposome formulation was added to the 200 μL of cell media in the wells. For the 2x concentration, 15.4 μL of liposome formulation was added to the 200 μL of cell media in the wells.

In order to determine the cytotoxicity of the liposome formulation, 96-well plates were loaded with the following sample sets: (1) cell media, (2) cell media and 1x liposome formulation, (3) cell media and 2x liposome formulation, (4) cell media and cells (control), (5) cell media, cells, and 1x liposome formulation incubated for 24 hours, (6) cell media, cells, and 2x liposome formulation incubated for 24 hours, (7) cell media,

cells, and 1x liposome formulation incubated for 48 hours, and (8) cell media, cells, and 2x liposome formulation incubated for 48 hours.

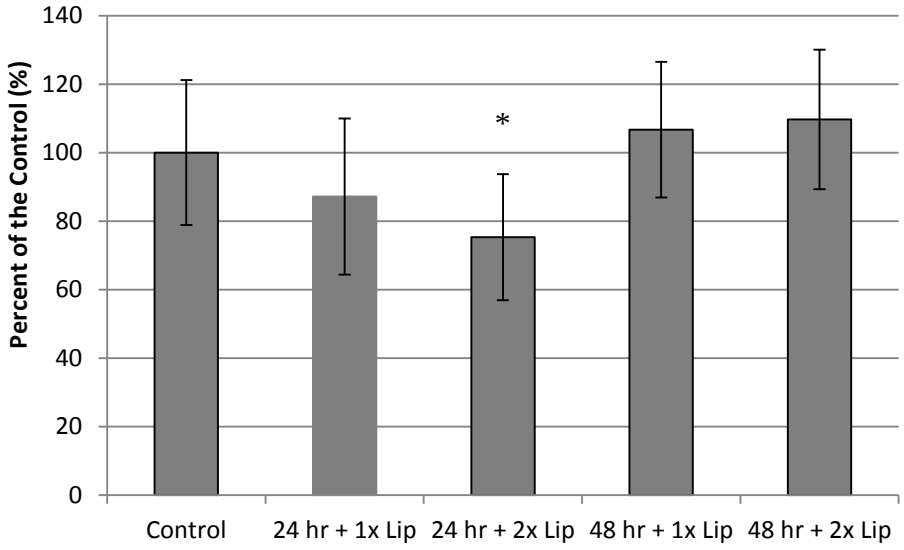

Figure 6-5. Neutral Red assay results for PC-3 cells grown with and without liposomes. Data points represent the average of n=7 and statistical significance was determined using Analysis of Variance (ANOVA) and Dunnett's posttest. Analysis was performed using GraphPad Prism software (GraphPad, Inc. La Jolla, CA). * denotes $p < 0.05$.

As seen in Figure 6-5, the addition of BCH-containing liposomes has no statistically significant impact on PC-3 cells regarding active uptake of neutral red dye into the lysosomes for the 1x liposome concentration experiments. There is a slight decrease in the average cell lysosome concentration capacity of the cells incubated with 2x liposome formulation for 24 hours. The 2x liposome formulation sample set was not performed in the post-irradiation colony formation assay studies presented in Chapter 7 in order to minimize the interruption of cell behavior unrelated to the thermal neutron capture mechanism.

6.2.2 MTS

The CellTiter 96® AQ_{ueous} One Solution Assay (Promega Corp., Madison, WI) is a colorimetric method for measuring the number of viable cells in proliferation within a cell culture.[91] Cell viability within the cell culture is determined by the detection of formazan. Specifically, a tetrazolium compound [3-(4,5-dimethylthaizol-2-yl)-5-(3-carboxymethoxyphenyl)-2-(4-sulfophenyl)-2H-tetrazolium], MTS, is bioreduced by the cells and converted into formazan. A majority of this bioreduction is accomplished by nicotinamide adenine dinucleotide phosphate (NADPH) or nicotinamide adenine dinucleotide dehydrogenase (NADH) products from dehydrogenase enzymes within metabolically active cells.[92]

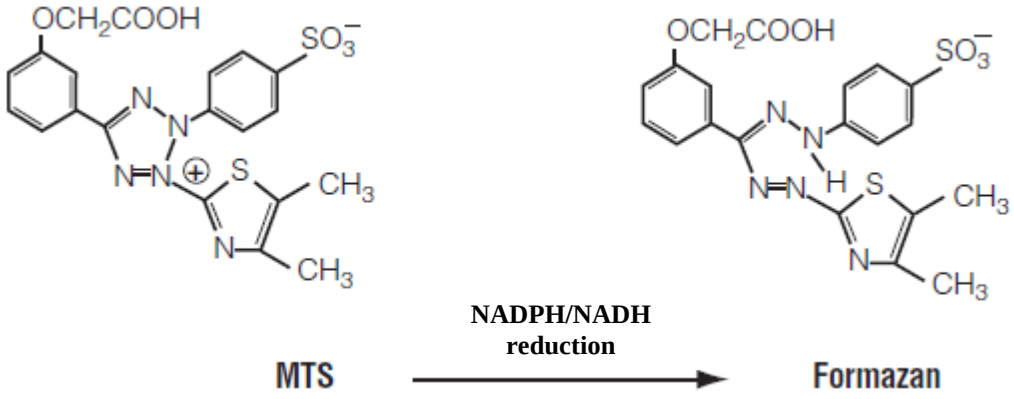

Figure 6-6. Bioreduction of MTS resulting in the formation of formazan.

Prior to performing the MTS assay, an MTS bioreduction curve was established to determine the proper cell seeding density. The curve was established by plating 0, 1000, 5000, 10000, 50000, and 100000 cells in 100 μL of growth media. Cells were incubated for 24 hours prior to performing the assay. Following the incubation period, 10 μL of

CellTiter 96® AQ_{ueous} One Solution Reagent was added to each well and incubated for one and two hour increments. The absorbance was measured at 490 nm using a SpectraMax 190 microplate reader with SoftMax Pro 5 GxP software (Molecular Devices, Sunnyvale, CA).[93, 94] The results are shown in Figure 6-7.

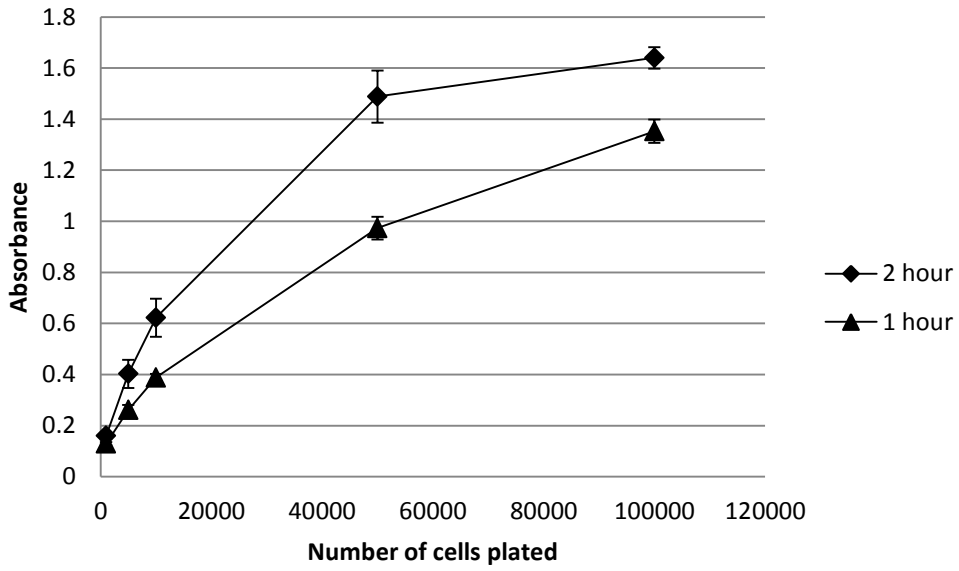

Figure 6-7. MTS response curve showing bioreduction as a function of cells plated. Error bars represent ± 1 SD.

In order to determine the cytotoxicity of the liposome formulation, 96-well plates were loaded with the following sample sets: (1) cell media, (2) cell media and 1x liposome formulation, (3) cell media and 2x liposome formulation, (4) cell media and cells (control), (5) cell media, cells, and 1x liposome formulation incubated for 24 hours, (6) cell media, cells, and 2x liposome formulation incubated for 24 hours, (7) cell media, cells, and 1x liposome formulation incubated for 48 hours, and (8) cell media, cells, and 2x liposome formulation incubated for 48 hours. A two hour incubation period was used for the Solution Reagent.

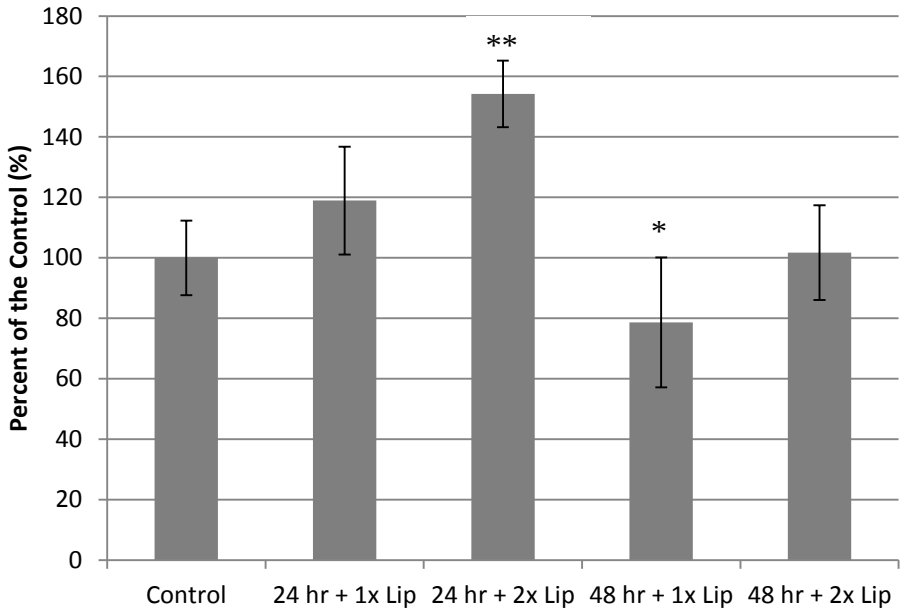

Figure 6-8. MTS assay results for PC-3 cells grown with and without liposomes. Data points represent the average of n=7 and statistical significance was determined using ANOVA and Bonferroni's posttest. Analysis was performed using GraphPad Prism software (GraphPad, Inc. La Jolla, CA). * denotes $p < 0.05$ and ** $p < 0.001$.

As shown in Figure 6-8, the liposome formulation appears to increase the metabolic activity within the PC-3 cells. The 2x concentration of lipsome formulation increases the metabolic activity in both the 24 and 48 hour incubation experiments with respect to the 1x lipsome forumation samples. In addition to this, metabolic activity decreases when the PC-3 cells are incubated with the BCH-containing liposomes for a 48 hour period at both concentrations. This observation contributed to the selection of the 24 hour incubation protocol for cell survial assays following irradiation with thermal neutrons. When determining the efficacy of BCH for the treatment of prostate cancer cells as part of a BNCT regime, isolating the targeted impact of the boron capture reaction from other cytotoxic effects is paramount to the success of the experiment.

6.2.3 LDH

The CytoTox 96® Non-radioactive Cytotoxicity Assay is a colorimetric method for measuring cell lysis within cell culture. The assay measures cell lysis through the detection of lactate dehydrogenase [68] in cell media. LDH is a stable cytosolic enzyme that is released from the cell when lysis occurs. Once released into the cell media, the conversion of a tetrazolium salt into a red formazan product results in a quantifiable measure of cell lysis within a cell culture well.[95-97]

Prior to performing the LDH assay, an LDH release curve was established to determine the proper cell seeding density. The curve was established by plating 0, 1000, 5000, 10000, 50000, and 100000 cells in 100 μL of growth media in a round bottom plate. Cells were incubated for 24 hours prior to performing the assay. Following the incubation period, 10 μL of Lysis Solution was added to the bottom four wells of each sample and incubated for one hour. The plate was centrifuged at 400 rpm for four minutes. In a separate flat bottom 96-well plate, 50 mL of Substrate Mix was added to each well. 50 mL of the supernatant from each well of the round bottom flask was then added to the 50 mL of Substrate Mix. The sample was covered with aluminum foil and left at room temperature for 30 minutes. 50 mL of Stop Solution was added to each well and left at room temperature for 10 minutes. The absorbance was measured at 490 nm using a SpectraMax 190 microplate reader with SoftMax Pro 5 GxP software (Molecular Devices, Sunnyvale, CA). The results are shown in Figure 6-9.

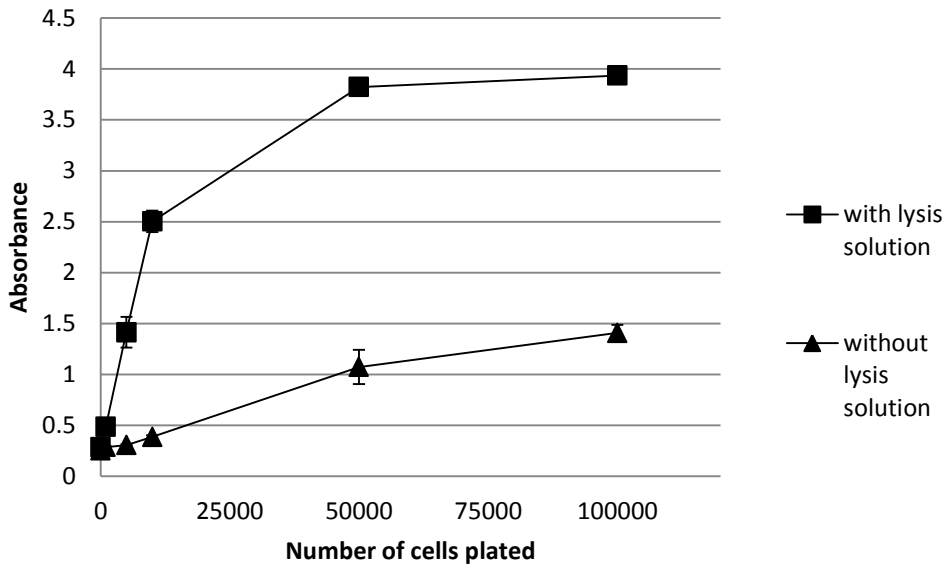

Figure 6-9. LDH response curve showing spontaneous LDH release as a function of cells plated. Error bars represent ± 1 SD.

In order to determine the cytotoxicity of the liposome formulation, 96-well plates were loaded with the following sample sets: (1) cell media, (2) cell media and 1x liposome formulation, (3) cell media and 2x liposome formulation, (4) cell media and cells (control), (5) cell media, cells, and 1x liposome formulation incubated for 24 hours, (6) cell media, cells, and 2x liposome formulation incubated for 24 hours, (7) cell media, cells, and 1x liposome formulation incubated for 48 hours, and (8) cell media, cells, and 2x liposome formulation incubated for 48 hours.

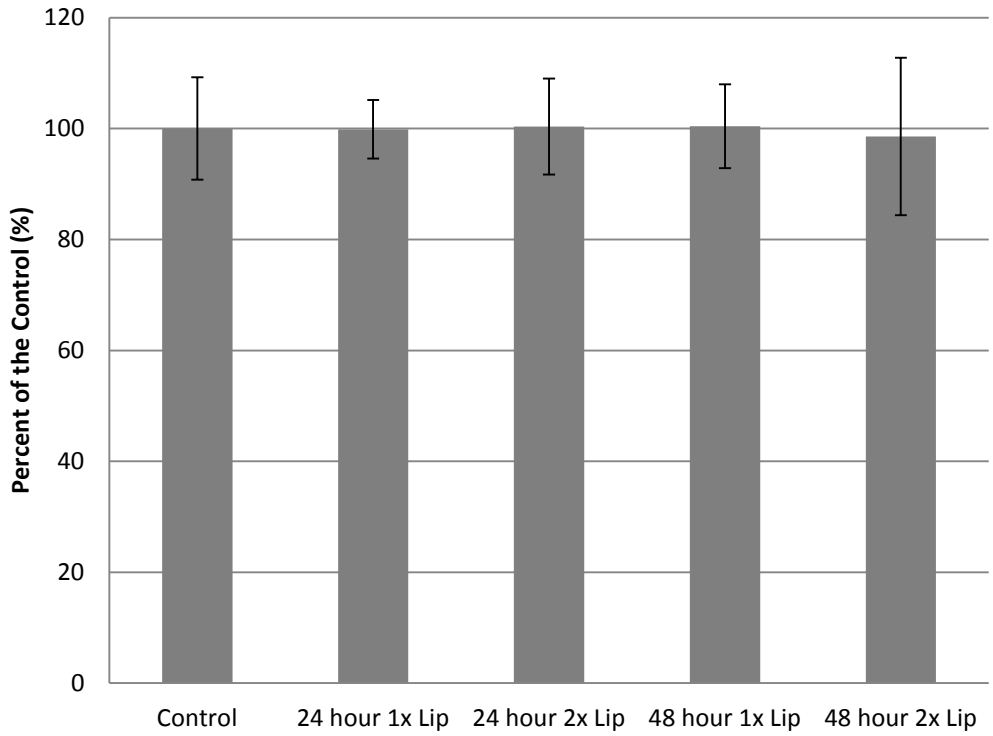

Figure 6-10. LDH assay results for PC-3 cells grown with and without liposomes. Data points represent the average of n=3 and statistical significance was determined using Analysis of Variance (ANOVA) and Dunnett's posttest. Analysis was performed using GraphPad Prism software (GraphPad, Inc. La Jolla, CA). No data sets were statistically significant compared to the control.

As shown in Figure 6-10, cell lysis is not evident in any of the samples incubated with the liposome formulation.

6.3 BCH Uptake Analysis

6.3.1 High-Performance Liquid Chromatography

High-performance liquid chromatography (HPLC) is an analytical chemistry technique for separating, identifying, and quantifying the various components in a sample mixture.

A small volume of sample is mixed with the mobile phase (solvent) and pumped through a chromatography column (stationary phase). As the solvent passes through the stationary phase, the components in the sample separate as they experience varying degrees of dispersive, dipole, and ionic interaction with the stationary phase. The different degrees of interaction within the stationary phase result in a characteristic retention time within the column as a function of the chemical properties of the components within the mixture. As the separated components elute from the stationary phase, ultraviolet detection is used to quantify each component. A schematic of an HPLC system is provided in Figure 6-11.

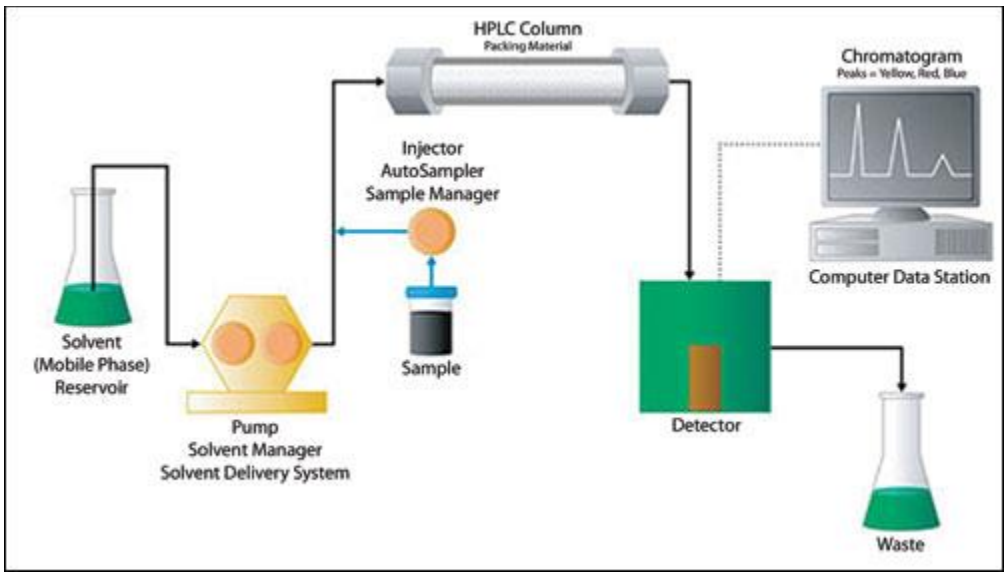

Figure 6-11. Schematic of high-performance liquid chromatography.

There are a number of different types of HPLC separation, such as normal phase, reverse phase, non-aqueous, ion-exchange, size exclusion, etc. Due to the hydrophobicity of the BCH molecule, non-aqueous reverse phase (NARP) chromatography was chosen to promote dissolution in the mobile phase and stationary phase interactions in a

hydrophobic medium. HPLC has been used previously as a method for detecting cholesterol and cholesteryl esters.[98-101]

HPLC was used to analyze the BCH within the cell samples in a method adapted from previous work by Dr. Sidwell.[102] Cell pellets were dried for 15 hours using a SpeedVac on medium heat. A solution of 1:1 (v:v) methanol:isopropanol (HPLC grade, Sigma-Adlrich, St. Louis, MO) was prepared and 1 mL added to the dried cells. The sample was vortexed for 10 seconds and the cells were ruptured to release the BCH using a probe sonicator. Cells were then rotated at 120 rpm for 30 minutes. Following this rotation, cells were centrifuged at 800 rcf for 10 minutes. For HPLC analysis, 50 μL of supernatant was injected in the column. HPLC was performed using a HP Agilent Series 1100 unit equipped with a column heater, UV-Vis photodiode array detector, 7725i manual injector, Agilent ZORBAX C-18 5 μm 150 x 4.6 mm analytical column, and Agilent ZORBAX C-18 5 μm 12.5 x 4.6 mm guard column. All samples were eluted isocratically at a flow rate of 0.5 mL/min and a column temperature of 40^{o}C using a mobile phase of 1:1 (v:v) methanol:isopropanol and detected by UV absorbance at the λ_{max} of BCH (202 nm). The conditions yielded a column back pressure of approximately 25 psi and a retention time for BCH of approximately 13.5 minutes. All sample injection volumes were 50 μL.

As reported previously, BCH uptake within a cell sample can be quantified using HPLC.[43, 102] The calibration curve for BCH detection was established by dissolving 1 mg each of cholesterol, BCH, cholesteryl oleate, and cholesteryl heptadecanoate in 50

mL of 1:1 (v/v) methanol:isopropanol mobile phase solution. A second standard solution was then prepared by diluting 10 mL of the first standard solution to a total volume of 50 mL with 1:1 (v/v) methanol:isopropanol mobile phase solution. The volume of standard solution injected onto the column was varied from 10-100 μL. This resulted in a calibration curve for BCH concentrations ranging from 0.8-40 μg/mL.

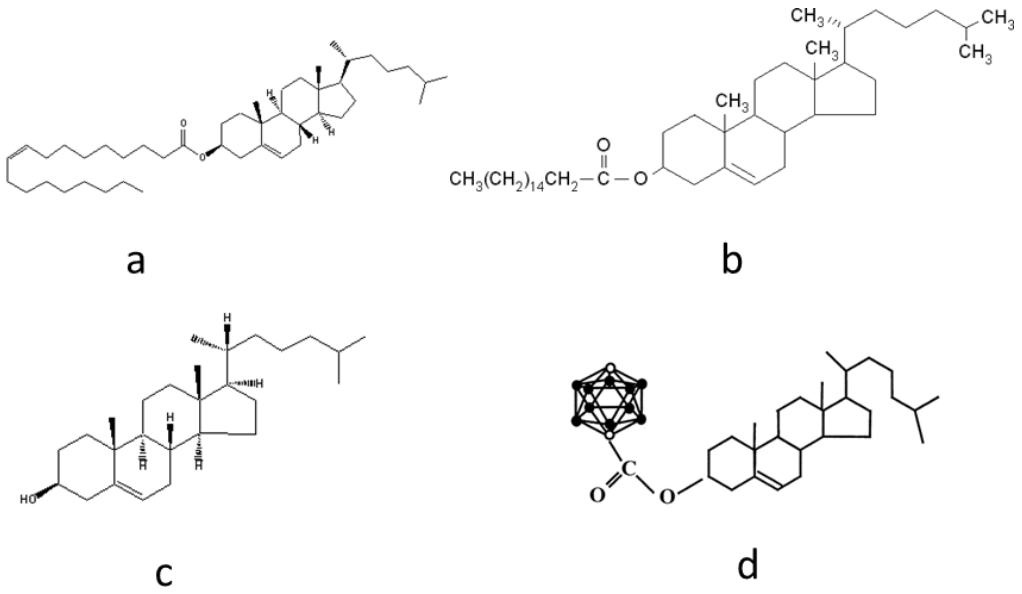

Figure 6-12. Chemical structures of the compounds within the HPLC standard solution (a) cholesteryl oleate, (b) cholesteryl heptadecanoate, (c) cholesterol, and (d) BCH.

As shown in Figure 6-13, a key advantage to using HPLC as a detection method for boron uptake in cells is that the intact BCH molecule can be measured. This allows a differentiation between boron delivered in the form of BCH and native boron within the cell or from contamination of the sample. As previously reported, BCH can successfully be separated from similarly sized compounds within the cell.[102] The HPLC separation spectrum of the standard solution is shown in Figure 6-13. The retention time for BCH

within this separation system is approximately 13.5 minutes. Analysis of PC-3 cells without the addition of BCH-loaded liposomes confirmed that the 13.5 minute peak found in the separation spectrum is unique to BCH.

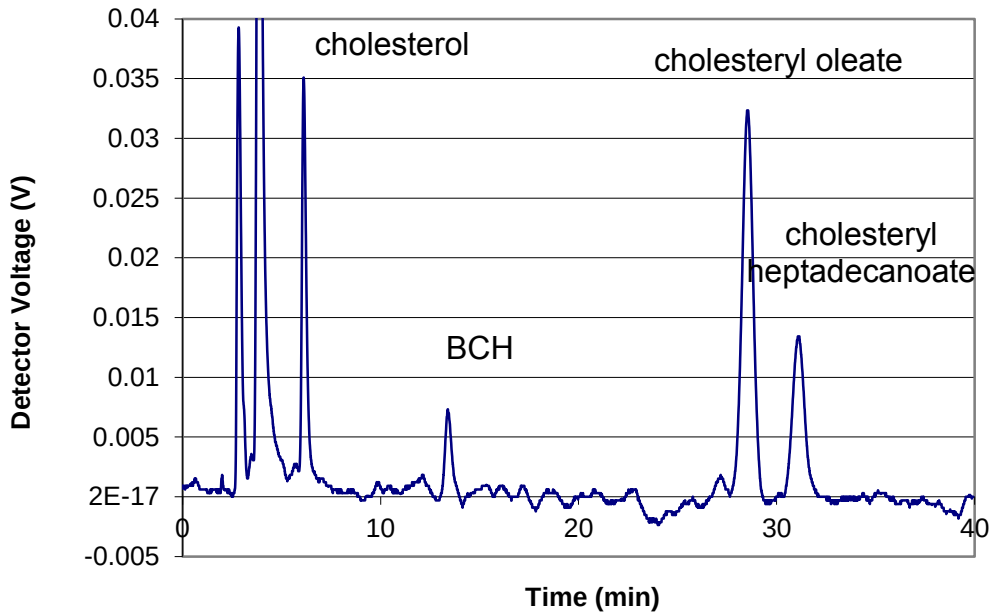

Figure 6-13. HPLC separation spectrum of the standard solution illustrating the separation capabilities of the non-aqueous reverse phase setup.

A more thorough description of the separation parameters, including retention factors and plate numbers, is provided by Dr. Sidwell.[102]

From the analysis of the standard solutions, the calibration curve for BCH detection by HPLC with peak area of the 13.5 minute peak directly proportional to the quantity of BCH injected into the sample port was determined. While the calibration curve remains

relatively linear across a large range of concentrations, the lower end of the range was used to quantify BCH presence in cell samples in order to minimize uncertainty.

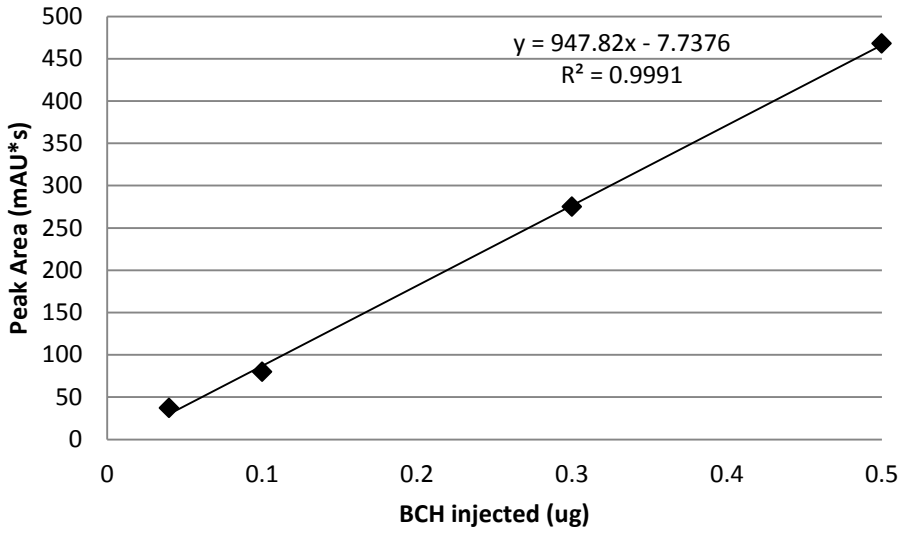

Figure 6-14. Calibration curve for BCH detection using HPLC. Data points represent the average of n=3 with a RSD <5%.

BCH uptake by PC-3 cells was investigated using the following protocol. PC-3 cells were subcultered four times and $5x10^6$ cells were seeded in a T-150 flask. The cells were incubated for 48 hours prior to addition of the liposome formulation. The 48 hours incubation time was selected to ensure that the PC-3 were within the logarithmic growth phase when exposed to the BCH-containing liposomes. Following the initial incbuation phase, the growth medium was aspirated from the flasks and the necessary volume of liposome formulation was added to the flask. Growth medium was added to the flasks to bring the final volume to 26 mL. After the incubation with BCH, the liposome formulation and growth medium were aspirated from the flask and the cells were washed three times with DPBS. Previous studies investigating the adherence of BCH on the cell

exterior reported that washing with DPBS is sufficient to remove non-specific BCH that had not undergone cellular endocytosis.[43] Cells were then trypsinized and pelleted for analysis. Cell pellets were stored at 4^{o}C until analyzed.

6.3.2 Inductively Coupled Plasma-Mass Spectrometry

Inductively coupled plasma-mass spectrometry (ICP-MS) is an analytical technique for determining elemental composition of a sample; and its efficacy in detecting low concentrations of boron has been established.[103-105] The use of ICP-MS in quantifying boron in a variety of biological samples [106-108], as well as the specific detection of boron from BCH in cell culture has been reported[44]. In short, ICP-MS analysis involves the use of a high-temperature plasma discharge to generate positively charged ions within a sample. Following the generation of positive ions, mass spectrometry is utilized to detect the ions and determine the elemental composition of the injected sample. The first process for ICP-MS analysis requires the generation of a fine aerosol using a nebulizer. The liquid sample is injected into the nebulizer as the pneumatic action of a flow gas breaks the sample into small droplets. Following formation of the droplets within the nebulizer, large droplets (> 10 μm) are filtered out in the spray chamber. Large droplets must be filtered out at this stage due to the inefficiency in dissociating them in the plasma discharge. After passing through the spray chamber, the small droplets are transported to the sample injector of the plasma torch. Within the plasma torch, a plasma discharge is created as argon gas flows through a radiofrequency (RF) coil. As the current within the coil oscillates, an electromagnetic

field is created that accelerates electrons formed when a high-voltage spark is applied to the argon gas. These newly formed electrons are accelerated in the magnetic field and collide with other argon atoms, generating a cascade of electrons. The collection of argon atoms, argon ions, and electrons form the inductively coupled plasma discharge. A third carrier gas then flows through the plasma discharge, introducing the aerosolized sample. As the sample droplets pass through the plasma, they undergo a series of changes in the preheating, radiation, and analytical zones. In the preheating zone, the droplet undergoes desolvation and becomes a very small, solid particle. Continuing through the plasma, the solid is converted into a gaseous form and then a ground state atom. At this point, the ground state atoms collide with the electrons in the plasma discharge and are converted into ions. The ions generated in the plasma then enter the interface region for transport to the mass spectrometer. In the interface region, ions pass through the sampler and skimmer cones before entering the ion optics. The ion optics function to transport the analyte ions to the mass spectrometer while filtering out as much of the matrix components as possible. This is accomplished by electrostatically controlled lens components which discriminate matrix ions and preferentially direct analyte ions to the mass spectrometer. Ions are separated by mass-to-charge ratio by the quadrupole mass filter. The quadrupole mass filter consists of four cylindrical rods, one pair imparted with a direct current (DC) field and the other pair with a RF. Working in concert, these four rods steer the ions of a particular mass-to-charge ratio to the detector. Manipulating the DC-RF voltage within the quadrupole mass filter permits the detection of a range of mass-to-charge ratios. After emerging from the mass analyzer, the ions are directed toward a discrete dynode electron multiplier for detection. In this process, the

ion flowing from the quadrupole mass filter is directed toward and strikes a dynode. Secondary electrons are liberated from the dynode and accelerated to the subsequent dynode, where more electrons are liberated. This process repeats itself in cascading fashion until the electrons are collected on the anode. The pulse created from the electrons at the anode is detected by a preamplifier and sent to a digital discriminator and counting circuitry. A schematic of ICP-MS is provided in Figure 6-15. Further discussion of ICP-MS can be found in a tutorial by Dr. Thomas.[109]

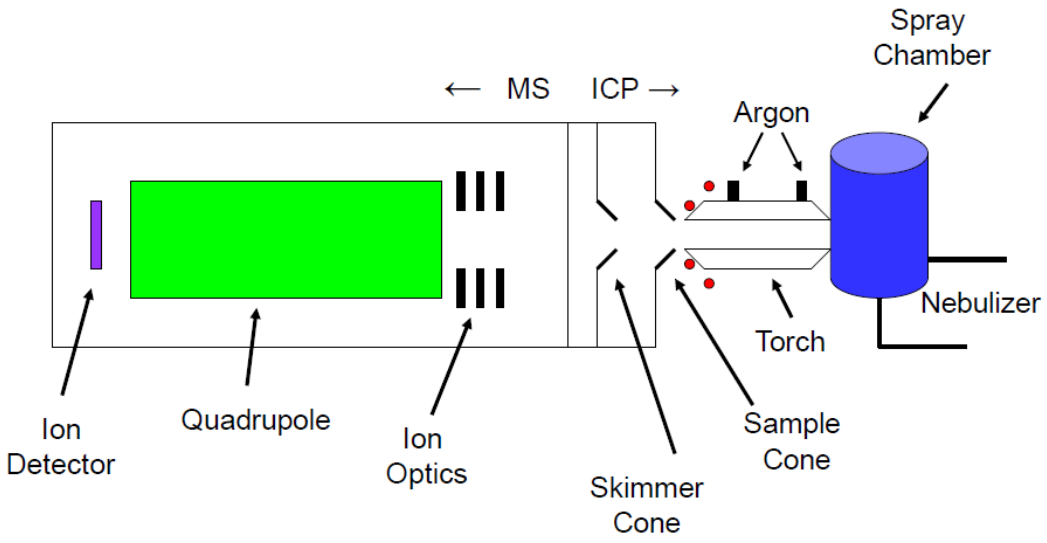

Figure 6-15. Schematic of ICP-MS.

The first step in detecting boron with ICP-MS is to establish a protocol for solubilizing the boron into a liquid for injection. Nitric acid is commonly used as a delivery agent. ^{10}B, ^{11}B, and natural boron standards were mixed in a series of nitric acid dilutions to determine the optimal method of introducing the boron into the sample chamber. Because the goal of BNCT is the targeted intracellular delivery of ^{10}B, the methodologies

were optimized for this measurement. Figure 6-16 shows the ^{10}B standard curve generated using the boron standard in nitric acid.

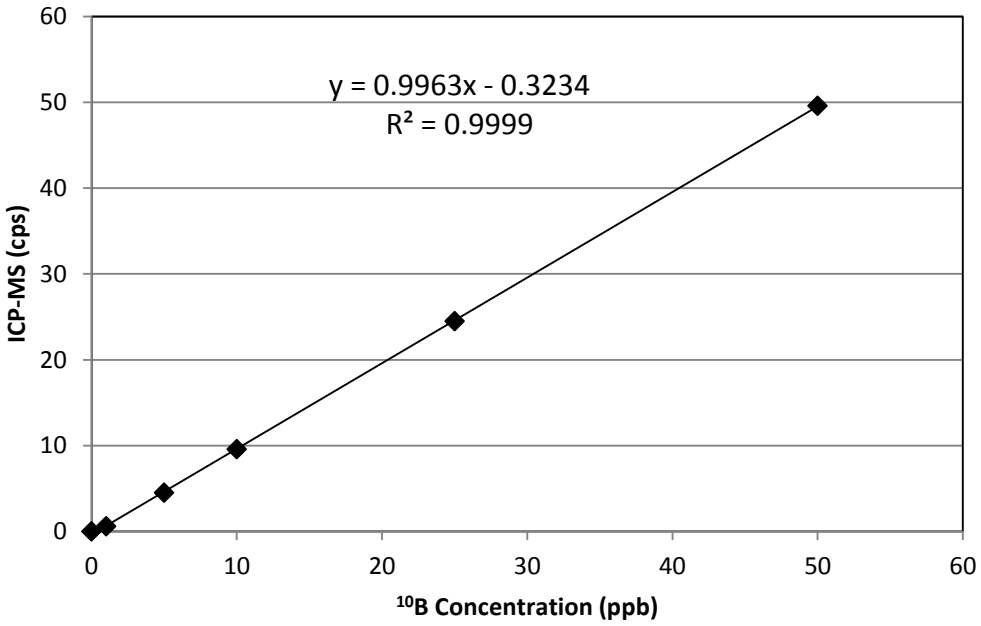

Figure 6-16. Standard curve for ^{10}B detection using ICP-MS. Data points represent the average of n=10 with a RSD <2% for all points above the LoQ.

The limit of blank (LoB), limit of detection (LoD), and limit of quantitation (LoQ) were calculated to be 0.710, 0.976, and 1.626 ppb, respectively. These limits correspond with other published results.[110]

Upon successfully measuring ^{10}B and generating a linear standard curve, a method was established for analyzing ^{10}B in *m*-carborane (Sigma-Aldrich, St. Louis, MO) and BCH. Combinations of nitric acid concentration (10, 40, and 70%) with incubation times (4, 8, 24, 48, and 72 hours) were investigated. ^{10}B in *m*-carborane was detected using the 70% nitric acid concentration and incubation times of at least 8 hours. On the other hand, the

BCH remained undigested even after 72 hours of incubation in 70% nitric acid. In order to facilitate the digestion of the BCH, a heating step was added to the method. Digestion temperatures of 50, 75, 110, and 150^{o}C were tested. At this point, a few additional variables were considered. Initially, 15mL Falcon polypropylene tubes were utilized in the digestion procedures. However, the structural integrity of the caps could not withstand the 150^{o}C heating step. Without a reliable cap to prevent sample loss during the digestion, this method was not viable. The next step was to perform the heated digestions in Teflon tubes. While the Teflon tubes were capable of withstanding the temperatures during the digestion, the pressure buildup within the tube dislodged the caps. Absent a means of securing the Teflon caps, the next test was performed with the digestion in Parr Acid Digestion Vessels. Combining the ntiric acid with a heated digestion in the Parr Acid Digestion Vessels provided an adequate methodology for the detection of ^{10}B in both the *m*-carborane and BCH samples.[111]

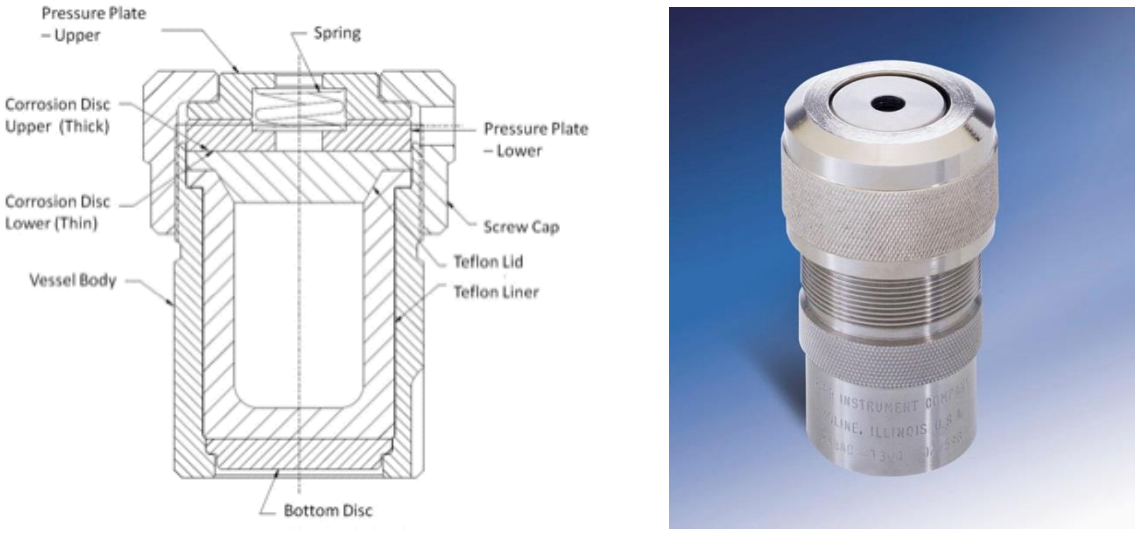

Figure 6-17. Schematic and image of Parr Acid Digestion Vessel used in the digestion of the PC-3 cell samples containing BCH for ICP-MS analysis.

Once the detection of ^{10}B in BCH with ICP-MS was established, the next step was to develop a protocol for digesting the PC-3 cells. This would allow the establishment of a background ^{10}B level within the human prostate cancer cells. In addition to dissolving the ^{10}B, the addition of biological material required another digestion component. A 30% hydrogen peroxide solution with 70% nitric acid was selected as the first trial with cell pellets of 10^6-10^8 cells. The cell pellets were also spike with ^{10}B standard, *m*-carborane, and BCH to test the ability and efficiency of boron detection in a matrix of biological material.

There are two key parameters that must be accounted for when digesting and analyzing the PC-3 ^{10}B uptake. First, boron tends to form micro-precipitates in the presence of highly concentrated nitric acid.[104] ICP-MS is unable to detect such precipitates, yielding an artificially low ^{10}B uptake in the sample. Therefore, it is recommended that the final nitric acid concentration in the ICP-MS injection sample be kept below 2%. Second, the final dilution of the sample must be kept sufficiently concentrated for the ^{10}B concentration to remain within the linear range of the ^{10}B calibration curve and above the lower limit of quantitation. With these two competing parameters in mind, a broad variety of testing conditions were investigated. After analyzing the various conditions, the optimum procedure was determined to include: (1) transferring the cell pellet to the Teflon insert of the Parr Acid digestion vessel (Parr Instrument Co., Moline, IL) with 0.1 mL of Dulbecco's phosphate-buffered saline (D-PBS, Invitrogen Corp., Carlsbad, CA), 0.29 mL of 70% nitric acid (Optima Ultrapure Grade, Fisher Scientific, Pittsburgh, PA), 0.1 mL of 30% hydrogen peroxide (Semiconductor Grade, Sigma Chemical Co., St.

Louis, MO), and 0.01 mL of the ^{103}Rh recovery standard (10 mg/mL, SPEX CertiPrep, Methuchen, NJ), (2) capping the digestion vessel and allowing 24 hours of room temperature digestion, (3) transferring the digestion vessel to a muffle furnace (Fisher Isotemp Muffle Furnace, Fisher Scientific, Pittsburgh, PA) for a 8 hour heated digestion at 150^{o}C, (4) transferring the digestion solution to a 15 mL conical polypropylene tube (B-D Falcon, Franklin Lakes, NJ) and diluting to a final volume of 10 mL with Milli-Q ultrapure water (18.2 MΩ-cm, Milli-Q Ultrapure Water System, Millipore Corp., Billerica, MA). Samples were then analyzed using ICP-MS (X-Series II ICP-MS System, ThermoScientific, Waltham, MA) equipped with an autosampler (Cetac ASX520 Autosampler, Omaha, NE) flowing 99.997% pure high-pressure liquid argon as the plasma gas with the following settings:

Table 6-1. Instrument settings for ICP-MS analysis of the BCH uptake in PC-3 cells.

Instrument Model: Thermo X-Series II		
Nebulizer	Concentric	
Spray chamber	Conical	
Torch injector	Quartz (1.5 mm)	
Forward power	1400 W	
Gas flow rates (L/min)	Nebulizer	0.87-0.92
	Cooling	13.0
	Auxiliary	0.7
Interface	Nickel cones	
	Sampler	1.0 mm
	Skimmer	0.9 mm
ICP-MS (standard mode)		
Analyte	^{10}B	
Recovery standard	^{103}Rh	
Internal standard	^{115}In	
Scanning mode	Peak jumping	
Acquisition time	4 s	
Replicates	3	
Sweeps	100	
Dwell time	10 ms	
Sample uptake rate (mL/min)	1.0	
Washout time	180 s	

The instrument was calibrated with external standards of the appropriate metal standard in 2% nitric acid. The sample probe was washed with a constant flow of 2% nitric acid between measurements. Quantitative analysis was obtained by reference to the slope of the calibration curve (counts per second/ng per liter), as well as an internal standard.

BCH uptake by PC-3 cells was investigated using the following protocol. PC-3 cells were subcultered four times and cells were seeded in a T-150 flask. The cells were incubated for 48 hours prior to addition of the liposome formulation. The 48 hours incubation time was selected to ensure that the PC-3 were within the logarithmic growth phase when exposed to the BCH-containing liposomes. Following the initial incbuation phase, the growth medium was aspirated from the flasks and the necessary volume of liposome formulation was added to the flask. Growth medium was added to the flasks to bring the final volume to 26 mL. After incubation with BCH, the liposome formulation and growth medium were aspirated from the flask and the cells were washed three times with DPBS. Cells were then trypsinized and pelleted for analysis. Cell pellets were stored at 4^{o}C until analyzed.

6.4 BCH Uptake Results

The uptake of BCH in PC-3 cells was investigated using HPLC and ICP-MS, as described in Sections 6.3. The primary goal for delivery of BCH is to load sufficient boron (20-35 μg/g cell) into the cells while minimizing toxicity. Toxicity effects of BCH have been reported, and therefore a lower concentration of BCH within the cell growth

medium was chosen.[44, 112] Cytotoxicity of the PC-3 cells was investigated and discussed in Section 6.2. Three main variables that were investigated for cellular uptake of BCH are incubation time, BCH concentration in the growth medium, and cell plating density.

It is important to note that the results shown in Figures 6-18 through 6-21 are based on preliminary studies to narrow the broad range of potential drug delivery parameters. They are not meant to provide quantitative analysis, and thus no values for uncertainty are provided. The trends observed factored into the optimization of the drug delivery parameters. Once the drug delivery protocol was established, quantification of BCH uptake in the PC-3 cells was analyzed with associated uncertainty discussed at the conclusion of this chapter. In addition to this, the BCH compound used in this research was synthesized with natural boron. In natural boron, the isotopic abundance of ^{10}B and ^{11}B are 19.9 and 80.1%, respectively. When used in a clinical setting, boron-containing BNCT compounds are synthesized with enriched ^{10}B. Therefore, for BNCT analysis of BCH in this research the total boron (^{10}B and ^{11}B) uptake is reported to allow comparison.

The initial studies performed to identify the relationship between BCH uptake and incubation time were performed using 1 mL of liposome formulation (1.3 μg boron/mL growth medium). In the first set of experiments, PC-3 cells were plated at a seeding density of $3.3x10^4$ cells/cm^2 and grown for 48 hours prior to the addition of the BCH-containing liposome formulation. The cells were then incubated for 4 and 24 hours prior

to harvesting of the cell samples for HPLC analysis as described in Section 6.3. In the second set of experiments, PC-3 cells were plated at a seeding density of $1.3x10^4$ cells/cm^2 and grown for 48 hours prior to the addition of the BCH-containing liposome formulation. The cells were then incubated for 6, 16, and 24 hours prior to harvesting of the cell samples for ICP-MS analysis as described in Section 6.4. The results of the boron uptake as a function of incubation time are shown in Figure 6-18 and all uptake results are reported in μg of total boron (^{10}B and ^{11}B) per g of cell (10^9 cells = 1 g).

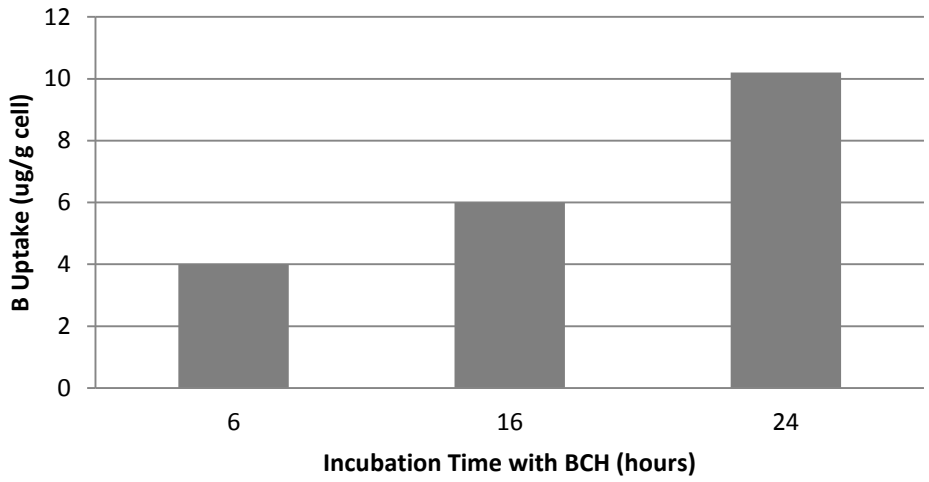

Figure 6-18. Boron uptake in PC-3 cells as a function of incubation time with ICP-MS as the detection method. Cells seeded at $1.3x10^4$ cells/cm^2 and grown for 48 hours prior to the addition of the liposome formulation. Cells were incubated with BCH for 6-24 hours and harvested for analysis. Uptake results are reported in μg of total boron (^{10}B and ^{11}B) per g of cell (10^9 cells = 1 g).

BCH uptake for the 4 and 24 hour incubation times as measured with HPLC were 8.6 μg/g cell and 34.2 μg/g cell, respectively.

The general trend in boron uptake as a function of incubation time is evident in both analyses. However, there is a significant decrease in boron uptake for the samples analyzed with ICP-MS. When comparing the uptake after 24 hours, the HPLC analysis yielded a value of 34.2 μg/g cell compared to 10.2 μg/g cell for the ICP-MS analysis. This can be explained by the difference in cell plating density of the two experiments. Although the growth characteristics of the PC-3 cells did not appear to vary significantly with the change in plating density from $1.3x10^4$ to $3.3x10^4$ cells/cm^2, there is a clear dependence for BCH uptake. To further investigate this matter, the experiment with ICP-MS was repeated using the same $3.3x10^4$ cells/cm^2 plating density as in the HPLC experiments. The results of this are shown in Figure 6-19.

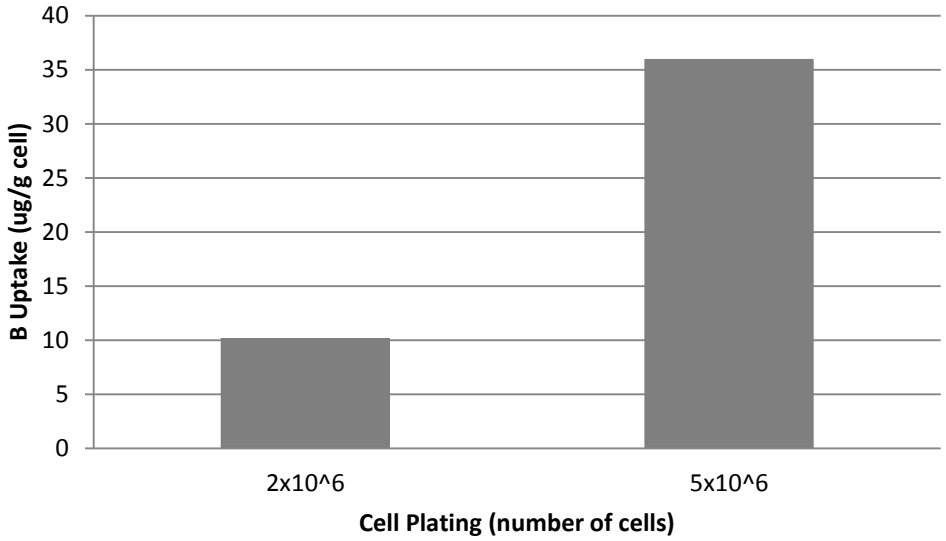

Figure 6-19. Boron uptake in PC-3 cells as a function of initial cell plating density with ICP-MS as the detection method. Cells seeded at $1.3x10^4$ and $3.3x10^4$ cells/cm^2 and grown for 48 hours prior to the addition of the liposome formulation. Cells were incubated with BCH for 24 hours and harvested for analysis. Uptake results are reported in μg of total boron (^{10}B and ^{11}B) per g of cell (10^9 cells = 1 g).

By increasing the plating density from $2x10^6$ total cells in a T-150 flask to $5x10^6$ total cells, the boron uptake increased from 10.2 to 36.0 μg/g cell. Because the boron uptake is corrected to cell number in the final calculation, this change is not simply explained by comparing the raw number of cells within the flask. The cell density within a *in vitro* growth environment plays a vital role in biological processes. Secretion of growth factors, cell-cell communication, enzymatic acticity, and protein expression, are examples of cellular behavior that are impacted by plating density. Variations in cell plating density have been shown to impact drug delivery in a number of cellular systems and must be accounted for when analyzing drug uptake and toxicology.[113-115] Further investigation into the mechanisms of boron uptake in relation to cell signalling and cell-cell contact interaction is beyond the scope of this research, however, warrants attention as a future extention.

When the cell plating densities was kept constant between the two experimental methods, boron uptake for PC-3 cells incubated for 24 hours in 1.3 μg boron/mL growth medium was measured with HPLC at 34.2 μg/g cell and 36.0 μg/g cell with ICP-MS.

The dependence of BCH uptake on the concentration of boron within the growth medium was also studied. For this set of experiments, cell cultures were prepared as described above and 1 or 2 mL of liposome formulation was added, yielding boron concentrations of 1.3 and 2.6 μg/mL in growth medium. The cells were incubated with the liposomes for 24 hours prior to harvesting for analysis with HPLC. In the second set of

experiments, cell cultures were prepared and 0.5, 1.0, and 1.5 mL of liposome formulation yeilding boron concentrations of 0.6, 1.3, and 1.9 μg/mL of growth medium. The results of the ICP-MS boron uptake as a function of boron concentration within the growth medium are shown in Figure 6-20.

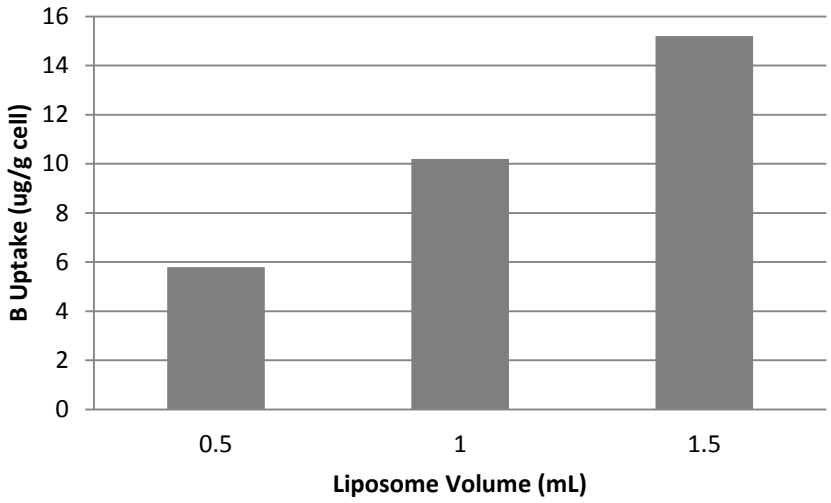

Figure 6-20. Boron uptake in PC-3 cells as a function of liposome concentration within the cell growth medium with ICP-MS as the detection method. Cells seeded at $1.3x10^4$ cells/cm^2 and grown for 48 hours prior to the addition of the liposome formulation. Cells were incubated with BCH for 24 hours and harvested for analysis. Uptake results are reported in μg of total boron (^{10}B and ^{11}B) per g of cell (10^9 cells = 1 g).

HPLC analysis of BCH uptake for the 1 and 2 mL liposome formulations yielded an uptake of 39.8 μg/g cell and 71.2 μg/g cell, respectively.

The general trend in boron uptake as a function of boron concentration in the growth medium is evident in both analyses. As discussed previuosly, the quantitative difference in uptake measured with HPLC and ICP-MS is attributed to the difference cell seeding densities for each experiment.

The dependence of BCH uptake on extended incubation times at the higher seeding density was then studied with ICP-MS. For this set of experiments, cell cultures were prepared as described above with a seeding density of $3.3x10^4$ cells/cm^2 and the incubation time following addition of the BCH-containing liposomes was observed at 24, 36, and 48 hours following the addition of 1.3 mg boron/ mL growth medium. The results of the boron uptake as a function of incubation time are shown in Figure 6-21.

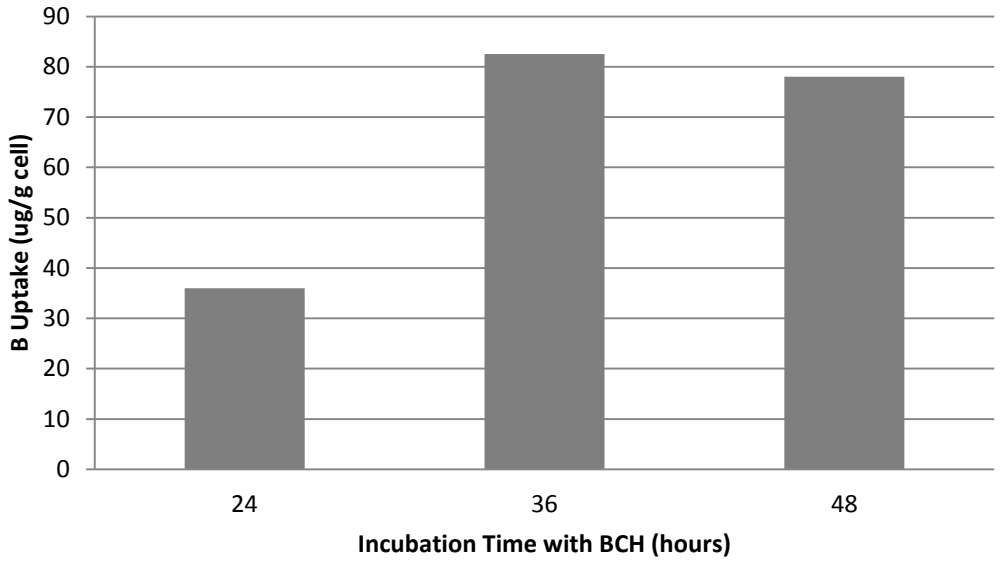

Figure 6-21. Boron uptake in PC-3 cells as a function of incubation time with ICP-MS as the detection method. Cells seeded at $3.3x10^4$ cells/cm^2 and grown for 48 hours prior to the addition of the liposome formulation. Cells were incubated with BCH for 24, 36, and 48 hours and harvested for analysis. Uptake results are reported in μg of total boron (^{10}B and ^{11}B) per g of cell (10^9 cells = 1 g).

Unlike previous experiments focusing on the boron uptake relationship as a function of incubation time for 0-24 hours, there appears to be a plateau forming as the cells are exposed to the BCH-containing liposomes in excess of 36 hours. The fairly linear

relationship from 0-24 hours is replaced with a levelling off, and possibly slight decline, in boron uptake for the longer incubation times. While this observation is interesting in its own right, it is important to note another key observation during this set of experiments. The MTS viability assay described in Section 6.2 indicated a decrease in metabolic activity for the PC-3 cells exposed to BCH-containing liposomes for 48 hours when compared to those incubated for the 24 hour increment. When observed under microscope, the cells incubated with BCH for 48 hours had a drastically different appearance than those incubated for 24 hours or less. Cloudiness in the growth medium and grainy cell membrane outlines were observed. Most importantly, clonogenic assays for the 48 hour incubation yielded cell survival percentages that were orders of magnitude less than expected. This observation was also noted, but to a lesser extent, in the 36 hour incubation sample. While cell appearance and growth medium clarity were not as significantly different from normal conditions, clonogenic assays revealed a decrease in survivability. Whether the decrease in proliferative capacity was due to boron toxicity, phospholipid toxicity, pH changes within the growth medium due to prolonged exposure to the liposome formulation, or another cause is unknown. Similarly, the cause and effect relationship between cell death and boron uptake are also unknown. As a future extension of this research, an investigation into whether the boron uptake resulted in the loss of proliferative capacity or whether the increase in born uptake was mediated by the distressed cell growth environment is of vital importance. Nonetheless, as a result of this set of experiments, future boron uptake experiments were limited to a maximum 24 hour incubation time and samples were collected for clonogenic assays following BCH exposure to ensure preservation of proliferative capacity.

In addition to the experiments outlined previuosly, representative studies investigating cell growth time prior to addition of the liposome formulation, variations in BCH concentration within the liposome formulation, and the addition of unhomogenized versus homogenized liposome formulation were performed. There are a seemingly endless combination of conditions to study when determining the optimal delivery protocol for BCH within a cellular system. However, when weighing the maximization of boron uptake with the desire to maintain cellular function, metabolism, and proliferative capacity the optimal conditions for this research were determined to be a $3.3x10^4$ cell/cm^2 cell plating density, grown for 48 hours prior to the addition of BCH-containing liposome formulation at a concentration of 1.3 μg boron/mL of growth medium, and incubated for 24 hours.

After identifying this specific boron delivery protocol, the experiment was repeated using various cell bank batches of PC-3 cells, separate liposome preparation samples, and both HPLC and ICP-MS boron detection methods to ensure the repeatability of the protocol. The six independent measurements resulted in a measured boron uptake of 35.2 ± 4.3 μg boron/g cell. This uptake is within the range discussed in the Chapter 2 for the boron presence in cells targeted for BNCT and provides proof-of-principle that BCH is a viable candidate for further investigation as a BNCT agent for the treatment of prostate cancer.

Chapter 7: Neutron Irradiation and Cell Survival

7.1 DNA Damage

The biological effects of radiation damage are principally observed as damage to deoxyribonucleic acid (DNA). This damage is in the form of base damage, strand breaks, sugar damage, and DNA cross-links, and can be the result of either direct or indirect action of radiation. In direct action, radiation interacts with the target DNA molecule, causing ionization or excitation that manifests as biological change. While direct action can be initiated by any form of radiation (x-rays, γ-rays, charged and uncharged particles), it is most often the result of radiation with high-LET. LET is the amount of energy that is transferred to a material per unit length of the radiation track, and is a function of the size, charge, and energy of the radiation. Particles that are large in size and carry a charge (i.e. α particles) are known as densely ionizing, while low-LET radiation (i.e. x-rays) is referred to as sparsely ionizing. Indirect action, on the other hand, occurs as radiation is absorbed by matter (typically water) surrounding the target DNA molecule, leading to the formation of free radicals (i.e. hydroxyl radicals). These free radicals then diffuse to the DNA and interact with the target molecule. Indirect action resulting in damage to DNA is predominantly due to hydroxyl radicals. The G value (yield of species per 100 eV) for hydroxyl radical formation in water by α particles, such as those released in ^{10}B capture of a thermal neutron, is approximately 0.25.[116]

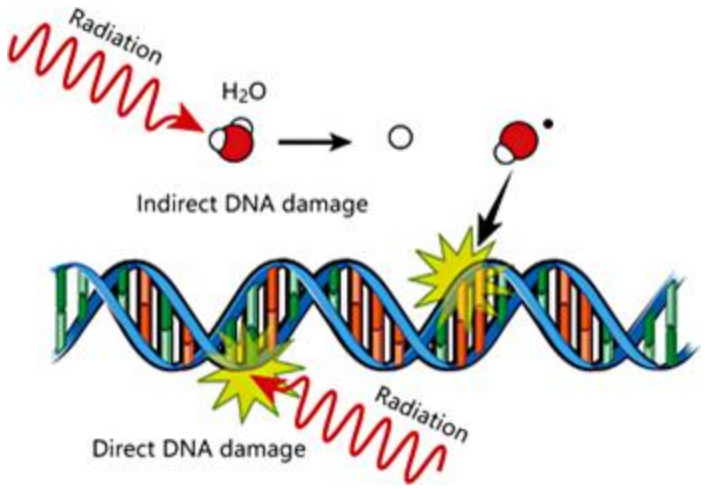

Figure 7-1. Diagram illustrating the mechanisms of indirect and direct DNA damage from radiation. Indirect damage results from formation of free radicals surrounding the DNA molecule. Direct damage results from damage imparted by charged particles.[117]

While both densely and sparsely ionizing radiation induce DNA damage, this damage is manifested in different ways. In order to properly relate the fundamental differences in DNA damage, it is important to briefly describe the structure of a DNA molecule. DNA is a large molecule consisting of two strands in a double-helical configuration held together by hydrogen bonding between the pyrimidine and purine bases. There are four bases and hydrogen bonding occurs between adenine/thymine and guanine/cytosine. These bases are connected along each strand by a sugar and phosphate backbone.

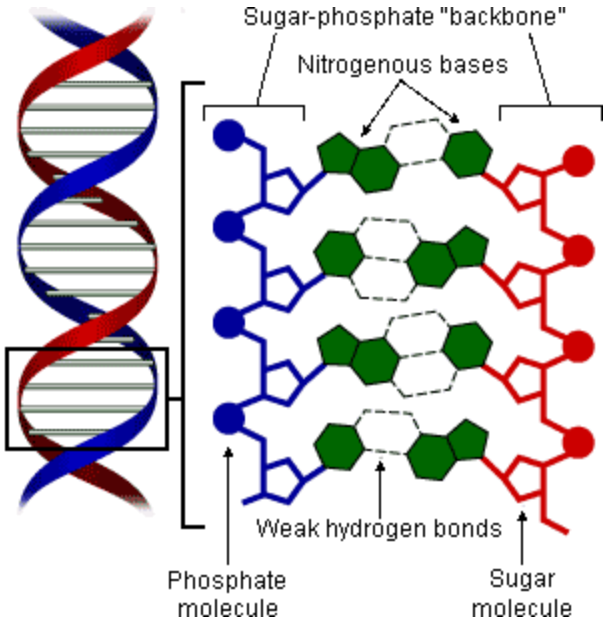

Figure 7-2. Structure of DNA molecule highlighting the hydrogen bonding between the base pairs bound to the sugar-phosphate backbones.

Damage most frequently occurs in two ways: (1) single-strand breaks (SSBs) and (2) double-strand breaks (DSBs). SSBs are readily repaired as the cell utilizes the corresponding strand as a template for replacing the damaged section. Similarly, concurrent SSBs that are well separated along the helix are repaired using the opposite strand as a template. However, base damage to strands opposite one another or only separated by a few bases often lead to DSBs. Because the template repair mechanism utilized for SSBs is not available, DSBs are a far more critical form of DNA damage and result in increased probability of cell death.

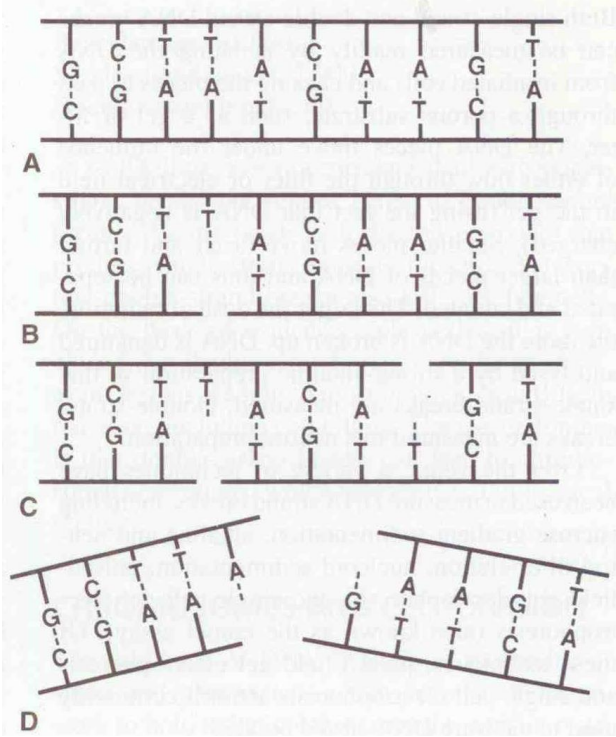

Figure 7-3. Diagrams presenting (A) normal DNA, (B) SSB that can be readily repaired using the remaining thymine as a template, (C) SSBs of sufficient separation that repair is relatively probable, and (D) DSB in which damage within adjacent base pairs results in separation of the chromatin.[118]

The ratio of SSB and DSB formation is a direct result of the radiation LET imposing damage to the DNA. Sparsely ionizing radiation commonly results in SSBs due to the release of "spurs" of energy (<100 eV in a 4 nm diameter sphere) along the radiation track. DSBs are dominated by densely ionizing radiation that results in "blobs" of energy (100-550 eV in a 7 nm diameter sphere).[118] Clearly, there is a much larger amount of energy released in a local area for densely ionizing radiation. This results in higher concentrations of DNA damage, leading to an increase in the probability of DSBs. The increase in DNA damage, and resulting cell death, as a function of radiation type is referred to as relative biologic effectiveness (RBE). RBE is determined by analyzing the equivalent absorbed dose required to induce a measured biologic effect compared to a

standard 250-kV x-ray. Carrying this concept further, it is understood that low-LET radiation will have a smaller RBE when compared to high-LET radiation due to the increased probability of DSBs observed in densely ionizing radiation. RBE as a function of LET is depicted in Figure 7-4.

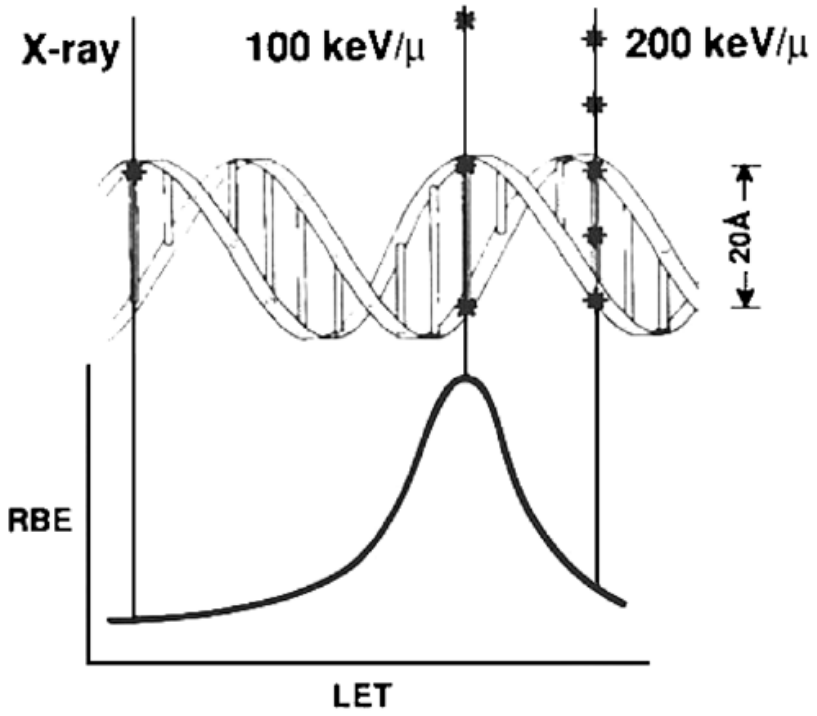

Figure 7-4 Relative biologic effectiveness as a function of varying LET radiation. The density of the imparted energy compared to the physical dimensions of the DNA molecule provides insight into the formation of SSBs and DSBs.[118]

Mammalian cells are quite efficient at repairing DNA damage, with an average of 10,000 lesions per day requiring repair due to replication errors, chemical degradation, exposure to ionizing radiation, or interactions with reactive oxygen species.[118] The two main mechanisms for repairing the DSBs found in high-LET radiation damage are nonhomologous end joining (NHEJ) and homologous recombination repair (HRR). In HRR, the presence of an undamaged chromosome allows for high-fidelity repair in the

S/G2 phases of the cell cycle. In the event that an undamaged chromosome is not available, such as in the G1 phase of the cell cycle, NHEJ facilitates ligation of two end joints.[118, 119] This process is prone to errors given the absence of a template and is likely the reason DSBs from ionizing radiation are often lethal.[120]

For cells preferentially loaded with BCH, the high-LET α particle and ^{7}Li nuclei yielded from the thermal neutron capture reaction result in densely ionizing radiation tracks traveling within the PC-3 cells. Section 7.2 of this chapter highlights the enhanced cell damage resulting from this high-LET irradiation when compared to the cell proliferative capacity response of control cells without boron.

7.2 Colony Formation Assays

While there are many assays for determining the proliferative capacity of cells in culture, the gold standard for quantifying cell reproductive capacity following exposure to ionizing radiation remains the colony formation, or clonogenic, assay.[121] The colony formation assay provides a means of detecting the cellular ability to produce a large number of progeny following exposure to radiation or other treatment method that can cause cell reproductive death due to chromosomal damage, apoptosis, etc.[122]

In order to evaluate the cell reproductive capacity of the PC-3 cells following irradiation with thermal neutrons, a clonogenic assay was performed as follows. Cells were removed from the incubator and washed with 3 mL DPBS. 1 mL of 0.25% (w/v)

Trypsin-0.53 mM EDTA was added to each flask and incubated for 10 minutes. The cell suspension was neutralized with 4 mL of complete growth medium (F12-K with 10% FBS) and pipetted up and down for 20 cycles. Cell concentration in solution was determined from a 10 μL sample volume using a hemocytometer. Cell solutions were diluted to the target plating concentrations. Dilutions were performed in 1:10 and 1:5 ratios and verified with a hemocytometer to ensure reliable cell concentrations in the diluted samples. After accounting for plating efficiency, cells were plated in T-25, T-75, and T-150 flasks with a target number of surviving colonies of approximately 50, 150, and 300, respectively. Complete growth medium was added to each flask and placed in an incubator for 10 days. At the completion of the 10-day growth period, growth medium was aspirated from the flasks and the cells were washed twice with DPBS. The cells were then preconditioned for fixation with 5 mL/25 cm^2 of 1:1 DPBS:methanol for 2 minutes. The DPBS:methanol was aspirated from the flask and 5 mL/25 cm^2 of methanol was added for 10 minutes for cell fixation. Following aspiration of the methanol, cells were stained with 5 mL/25 cm^2 crystal violet for 10 minutes. The crystal violet stain solution was aspirated from the cell flask, cells were washed with tap water, and rinsed one final time with deionized water. The cell flasks were dried at room temperature prior to counting. Colonies consisting of at least 50 cells were counted.

Figure 7-5. PC-3 colonies stained with crystal violet for quantifying the survival fraction in a colony forming assay.

7.2.1 Clonogenic Analysis

When determining the efficacy of a bimodal drug-radiation therapy, it is vital to understand the impact on proliferative capacity of the individual drug and radiation treatments. Therefore, for each experiment, radiation treatments were performed with and without the BCH and parallel clonogenic assays were performed for unirradiated cells treated with BCH at identical concentrations and incubation times. By combining each of these control experiments, the efficacy of the complete bimodal treatment can be properly evaluated.

The surviving fraction (SF) is calculated as follows:

$$SF = \frac{\#\ of\ colonies\ formed\ after\ treamtment}{\#\ of\ cells\ seeded * PE} \qquad (7\text{-}1)$$

The results of the clonogenic assays are shown in Figure 7-6. The cell survival percentages were corrected for plating efficiency (PE) and normalized to account for the proliferative impact of treatment with BCH alone (no radiation). A thermal neutron fluence-dependent decrease in survival of PC-3 cells targeted with BCH was observed when compared to the control. Colony formation assays demonstrated a 20-25% decrease in clonogenic capacity for PC-3 cells containing 35.2 $\pm$ 4.3 μg boron/10^9 cells (6.9 μg ^{10}B/10^9 cells) exposed to a thermal neutron fluence of 9.4x10^{11} n/cm^2.

The shape of the cell survival curve reveals further information regarding the mechanism of cell damage within the ^{10}B loaded cells. As discussed previously in Section 7.1, repair mechanisms for low and high-LET radiation damage exhibit different behavior within the cell. Briefly, low-LET radiation results in SSBs that are often repaired within the cell. Evidence of predominant low-LET damage manifests in a significant "shoulder" for low dose irradiations. As the total dose is increased, repair mechanisms are less effective and the cell survival curve slope increases. For high-LET radiation, however, the initial low dose "shoulder" is much less pronounced, if present at all. The dense distribution of energy in high-LET radiation results in a much higher probability of lethal DSBs without effective DNA repair.

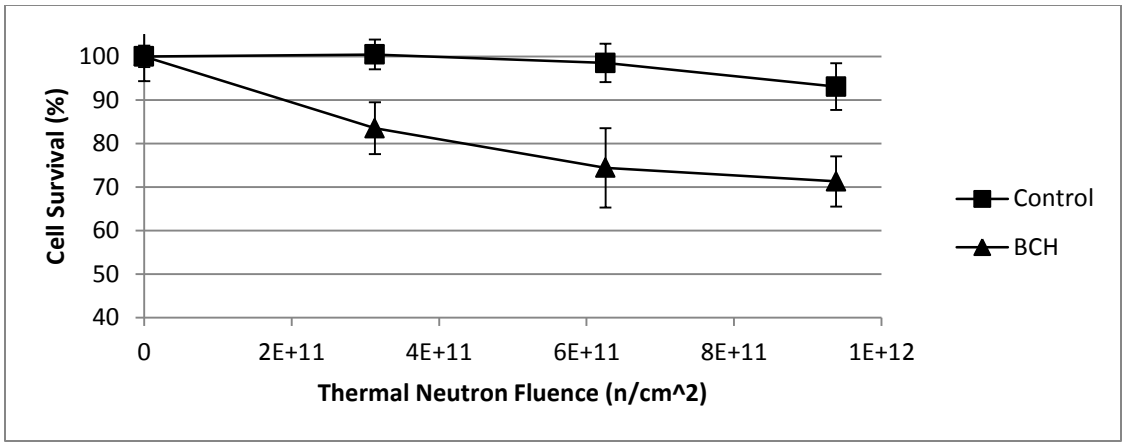

Figure 7-6. Cell survival analysis of PC-3 cells with and without BCH and irradiated with thermal neutrons. Error bars represent $\pm$ 1 SD. Irradiations performed in triplicate.

Chapter 8: Conclusions and Future Work

8.1 Conclusions

In conclusion, the generation of high-LET α particles and ^{7}Li nuclei generated from intracellular ^{10}B thermal neutron capture reactions within human prostate cancer cells preferentially loaded with boron-containing cholesteryl esters is an effective method of targeted cancer therapy. Irradiation of treated PC-3 cells with a thermal neutron fluence of 9.4 x10^{11} n/cm^2 resulted in a 20-25% decrease in cell proliferation capacity. The decrease in cell proliferative capacity, as quantified by colony formation assays, is dose-dependent and proportional to the thermal neutron fluence in the 0 – 9.4 x10^{11} n/cm^2 range. The densely ionizing radiation emitted from the capture reaction induces DNA damage through direct and indirect action. Direct action from high-LET radiation produces double-strand DNA breaks with high probability due to the pattern of energy deposited along the ionization tracks. Indirect action is the result of free radical formation and diffusion within the aqueous environment surrounding DNA, causing single-strand and double-strand DNA damage. Although the distinction between direct and indirect mechanisms of DNA damage was not specifically evaluated, it is predicted that a majority of the lethal double-strand breaks are due to the direct action of the high-LET particles. The radiation-chemical yield of hydroxyl radical formation (G ($^{\bullet}$OH) < 0.5 per 100 eV) from 1.5 MeV α particles in water is relatively low compared to hydroxyl radical yields from low-LET radiation (G ($^{\bullet}$OH) > 2.5 per 100 eV). The low hydroxyl radical yield from α particles is due to free radical recombination along the densely concentrated particle tracks.

Capitalizing on the lack of feedback regulation of low-density lipoprotein (LDL) receptors by human prostate cancer PC-3 cells, a cholesteryl ester mimic containing carborane was selected as a promising BNCT agent. Due to the hydrophobicity of the BCH compound, it was concluded that encapsulation within the lipid bilayer of DPPC and cholesterol-based liposomes was necessary to enhance intracellular delivery. Encapsulation in the lipophilic region of the liposomes likely facilitated the transfer of BCH into the cholesteryl ester-based core of LDL, resulting in intracellular delivery of the boron through receptor-mediated endocytosis. This drug delivery technique provided a means of selectively targeting PC-3 cells by utilizing an inherent biological pathway, and without which uptake of BCH into the cancer cells would have been unachievable at the quantities required for BNCT. BCH-containing liposome formulations were prepared by the thin film hydration method and subsequently exposed to high-pressure homogenization to convert the large multilamellar vesicles (LMV) into small (SUV) and intermediate-sized unilamellar vesicles (IUV). Dynamic light scattering (DLS) size analysis of the liposome formulation yielded a mean liposome diameter of 111.5 nm with a 0.113 relative variance using the non-negatively constrained least squares (NNLS) algorithm for multimodal size distribution analysis. Conversion of the LMV to SUV/IUV enhances the transfer of BCH cholesteryl ester compounds to LDL within the cell media.

The cytotoxic effect of the BCH-containing liposome formulation was analyzed using neutral red, MTS, LDH, and colony formation assays. Variations in incubation time and

liposome concentration within the cell growth medium were evaluated to ensure cell damage to the target population was attributable to the ^{10}B thermal neutron capture. Active uptake and concentration of neutral red dye into the lysosomes remained comparable to the control study for all conditions except the 24 hour incubation with 2x liposome concentration in the cell growth medium, where a statistically significant decrease to 75% of the control was measured. Metabolic activity related to bioreduction was evaluated based on the MTS assay. Addition of BCH-containing liposomes to the PC-3 cells resulted in increased metabolic activity over a 24 hour time period in a concentration-dependent manner. After 48 hours, however, metabolic activity returned to equal (1x) or decreased (2x) values compared to the control. A disruption in bioreduction is an indication of the onset of toxicity effects within the PC-3 cells for the prolonged drug exposure. The integrity of the cell membrane following incubation with the liposomes was evaluated via the LDH assay. In each sample, no significant increase in membrane leakage of cytosolic material was observed. In a final method to evaluate the cytotoxic effect of BCH, colony formation assays were performed to quantify the long term clonogenic capacity of the cells. For samples exposed to the BCH-containing liposomes in excess of 24 hours, a reduction in proliferation of a few orders of magnitude was observed. The results of a range of assays to detect changes in cell behavior, including transport mechanisms, metabolic activity, structural integrity, and clonogenic capacity, were used to evaluate the drug delivery conditions for boron delivery to the PC-3 cells. Based on the data collected, a 24 hour incubation time with 1x liposome formulation was selected for BNCT irradiations in a thermal neutron field.

Cellular uptake of boron by the PC-3 cells was quantified by high-performance liquid chromatography (HPLC) and inductively coupled plasma-mass spectrometry (ICP-MS). HPLC provides direct measurement of the intact BCH compound, while the ICP-MS methodology measures the presence of ^{10}B within the sample. Drug delivery conditions selected to minimize cytotoxic effects of the liposome formulation, as characterized with the assays listed above, resulted in a boron uptake of 35.2 $\pm$ 4.3 μg/g cell. This value exceeds the recommended therapeutic specification of ~20 μg/g cell for successful BNCT treatment.

Because the thermal neutron capture cross section of ^{10}B is dependent on the energy of the incident neutron, it was determined that direct measurement and computational modeling of the neutron spectrum within the thermal column experimental facility was required to adequately evaluate the efficacy of ^{10}B capture in BNCT treatment. Measurements of the neutron spectrum were achieved through a combination of experimental measurements, deconvolution of detector responses, and MCNP modeling of the MUTR core and surrounding facilities. Experimental neutron measurements were accomplished by passive neutron detection combined with resonance absorptions, threshold reactions, and moderate and capture techniques. The increase in detector responses afforded by the diverse range of neutron detection methods resulted in high spectral resolution of the thermal neutron energy range. Deconvolution of the detector responses was performed based on the maximum entropy principle encoded into "MAXED" with a RATE-generated starting spectrum and MCNP5 response matrices. Results of this spectrum unfolding were compared to an MCNP/X computed model of the

MUTR for benchmarking and verification. The neutron fluence rate within the entire energy spectrum (10^{-9} – 16 MeV) was within 5% when comparing the experimental measurements with the MCNP/X computed model. Within the < 3 eV neutron energy range, results of the two methods were also within 5%. The greatest variation (17%) between the experimental and computed results in the 10^{-7} – 10^{-6} MeV energy range can be attributed to a spectrum shift resulting from variations in the final sample chamber configuration compared to the modeled chamber, and temperature modeling within the thermal column. The presence of a hydrogenous sample chamber surrounding the neutron detectors in the experimental measurement contributed to further thermalization of the neutron field that was not accounted for in the computer model. In addition, neutron scattering within the thermal column experimental facility is largely dependent on the molecular motion of hydrogen, whereby small discrepancies in temperature can shift the Gaussian distribution of thermal neutron energies. These sources of error are present when evaluating narrow energy bands, however, integral neutron fluences over larger energy regions decrease this uncertainty. Accounting for fluctuations in nuclear reactor power with real-time monitoring, anisotropy in the neutron beam, fluence rate uniformity across the sample chamber plane, and starting spectrum bias in deconvolution were integral in attaining accurate unfolding of the neutron spectrum. The thermal neutron fluence rate at 250 kW reactor power within the sample chamber was determined to be 8.69 x 10^{8} n/cm^{2}/s, with the < 3 eV thermal neutron energy region representing 94.6% of the total neutron field. Thermal neutron moderation within the thermal column facilitating ^{10}B thermal neutron capture resulted in a factor of five dose enhancement, confirmed using dual A150 tissue equivalent ionization chambers (one doped with 184

ppm ^{10}B). The gamma ray dose rate of 0.94 $\pm$ 0.6 cGy/min was measured within the thermal column experimental facility at 250 kW using an ionization chamber. This gamma ray dose rate is within the recommended specification of 1 Gy/hr for BNCT facilities.

8.2 Future Work

The development of a nuclear reactor experimental facility and subsequent analysis of a boron-containing agent for BNCT leads to further research directions. Several questions remain regarding optimization of thermal neutron irradiation and intracellular delivery of BCH.

Thermal neutron irradiation within the MUTR thermal column is capable of providing sufficient thermal neutron fluence rates for the evaluation of the BCH compound; however, enhancement of the fluence rate is possible through modification of the graphite assembly. The current configuration allows for customized graphite stringer arrangements within the moderator array. Through computer modeling and experimental measurements, location of the sample chamber in closer proximity to the reactor core in combination with various moderator/shielding materials could increase the thermal fluence rate while maintaining a low gamma ray and fast neutron contribution to the delivered dose. In addition to increasing the thermal fluence rate, the epithermal neutron ratio could also be increased. This would allow a variety of sample chamber caps to be installed, enhancing environmental control within the chamber while providing sufficient penetration of the neutron field. Upgrading the licensed reactor thermal power limit to

500 kW or 1 MW would also enhance research capabilities within the thermal column of the MUTR, as neutron fluence is directly proportional to thermal power.

Future evaluation of the BCH compound for delivery to PC-3 cells is also important. By investigating the transfer of BCH cholesteryl ester mimics from liposomes to LDL, it is possible that increased ^{10}B uptake can be achieved. Variations in liposome size and BCH concentration within the lipid bilayers should be studied to determine optimal transfer conditions. In addition, further understanding of the cytotoxic mechanisms related to boron delivery to PC-3 cells would be a valuable contribution to the BNCT drug delivery field of research. The mechanisms related to observed metabolic stimulation following exposure to BCH-containing liposomes and significant reduction in long-term proliferative capacity for exposure times in excess of 24 hours should be investigated further.

And finally, continuing this research to include the BCH-related compounds incorporating fatty acid chains bound to the cholesteryl ester would provide a more thorough understanding of the potential for targeted delivery of boron within cancer cells systems. Once proof-of-principle has been established, the use of ^{10}B-enriched carborane with the BCH family of cholesteryl esters for treatment of cancer systems provides an opportunity for significant contribution to the field of neutron capture radiobiology.

Appendix A

MARYLAND UNIVERSITY TRAINING REACTOR

PROPOSAL TO REMOVE THE ACCESS PLUG TO THE THERMAL COLUMN

Table of Contents

PURPOSE

The purpose of this proposal is to provide a detailed procedure on how to remove the access plug from the thermal column of the Maryland University Training Reactor. Removing the access plug will allow personnel to place experiments near or in the thermal column in order to obtain thermal neutrons.

PRECAUTIONS AND REQUIREMENTS

Removing the access plug is classified as a Special Experiment. Therefore this proposal requires the approval of the Reactor Safety Committee and the Reactor Director. This proposal must also comply with the guidelines set by 10 CFR 50.59.

The access plug to the thermal column has never been removed, so the dose rate that one may receive from activated particles in the thermal column is unknown.

The access plug must be removed in intervals, and radiation readings must be taken at each interval. These readings will be recorded and analyzed to predict trends before the next incremental withdrawal.

The withdrawal intervals should be approximately 1 inch. By keeping the intervals very small, the access plug can be easily inserted if radiation levels reach an unacceptable level.

If at any time during the withdrawal process the radiation exceeds 100 mrem/hr, removal of the access plug will cease and exposure times evaluated with the assistance of the Radiation Safety Officer [76].

According to the technical drawings, the weight of the access plug is 800 lb. Therefore, a manually operated lever hoist rated at 2000 lbs will be used to remove the plug. This provides a safety factor of 2.5.

The reactor must be secured and shutdown at least 5 days prior to the experiment and during the withdrawal and insertion of the shielding plug and/or graphite stringers.

The calibration of all radiation monitoring devices utilized in the removal process shall be verified within 24 hours of plug removal.

REQUIRED MATERIALS AND PREPARATIONS

Chain to mark off high radiation area

Lever Hoist – Columbus McKinnon Model 5318, rated at 2000 lbs or equivalent.

Leather gloves for personnel involved in removing the access plug

Safety goggles for all personal involved in the removal or replacement

Neutron detectors and gamma/beta detectors to monitor radiation near the face of the access plug.

Table rated at 2000 lbs. to support the access plug once it has been removed. What is significant about this cart is that the surface consists of casters which will enable workers to easily guide the access plug back into the thermal column. The sides of the cart will contain lips to ensure that the plug does not fall off the cart.

Full body protective suit for all personnel entering the confines of room 1308 while the insert is either in transit or removed from the fully inserted position.

Radiation monitoring as recommended by the Radiation Safety Officer or their appointed representative.

PROCEDURE

Review the control room log book to ensure that the reactor has been shutdown for at least 5 days.

Mark off the area with tape. There should only be 3 personnel allowed in the radiation area during the removal of the access plug. One will remove the plug, one will monitor the radiation levels, and one will ensure that the plug is pulled on the top of the cart.

The entire plug will be enclosed by means of a modified glove bag or equivalent barrier to minimize the effects of disturbing the dust and or contaminants that may have accumulated since the plug was last removed. Radiation levels will be monitored by a RSO representative who shall maintain air monitoring within the glove bag and will evaluate the readings every quarter hour. This information will be recorded and maintained with the final report for this project.

Set up a neutron detector and a gamma/beta detector near the face of the access plug. Take neutron and gamma/beta readings at this time and record the readings.

Attach the lever hoist to the hook on the face of the south wall. Attach the other end of the lever hoist to the hook on the access plug. Make sure that you have attached the lever hoist to the access plug and not to the thermal column plug.

Position the cart so that the access plug will be pulled onto the top of the cart.

All members in the radiation area must don leather gloves, safety goggles, and be equipped with a self-reading dosimeter which will be evaluated and recorded every 15 minutes to monitor radiation exposure.

Using the lever hoist, slowly remove the plug approximately 1 inch and stop. Take radiation measurements and record them.

NOTE: *If at any time the radiation readings exceed 100 mrem/hr, immediately cease removal of the plug and notify the RSO representative of the readings so that exposure times may be calculated.*

Repeat Step 4.7 until the access plug is completely removed and is safely secured on the cart. Photograph and perform radiation wipe test on all interior faces with assistance from the RSO.

Look into the void where the access plug normally occupies and observe the face of the thermal column. There should be 4 exposed graphite stringers. Record and photograph their condition and report any damage or abnormalities.

RECOVERY AND REPLACEMENT OF PLUG

The plug shall be fully inserted before the reactor is removed from a secured condition as defined by the Technical Specifications.

No operations of the reactor shall resume until such time that the radiation levels are demonstrated to be that of pre-removal levels. A review of these levels shall be forwarded to the Reactor Director who shall review the results and provide recommendations as to whether the Chair of the Reactor Safety Committee should authorize a return to unrestricted operation.

10CFR50.59 REVIEW

The removal of the thermal column does not require a License Amendment Request (LAR) as allowed under 10CFR50.59 for the following reasons:

This removal of the plug does not require a modification of the Technical Specifications. (10CFR50.59(c)(1)(i)

The proposed experiment has been evaluated and does not meet the criteria set forth in 10CFR50.59(c)(2)

EMERGENCY RECOVERY

In the event that the radiation levels exceed the limits set forth previously, the measurement process will cease immediately. At this point the plug will be inserted fully into the core. In the event that the insertion may not be accomplished either due to binding of the plug or failure of components of the withdrawal/insertion system, the plug shall be inserted manually. This manual insertion shall be accomplished by use of eight foot long rigid bar stretched across the face of the plug and inserted by using two staff members on each end that will physically push the plug into place. The plug shall remain in this position until such time that the Reactor Director is satisfied that the failure mode has been corrected. The Reactor Director shall produce a written plan that describes the failure mode and measures taken to mitigate the possibility of a subsequent failure.

In the event that the plug shall shift or fall resulting in physical injury to personnel, MUTR personnel shall contact the UMDPS via the UMPD supplied emergency radio

system. This radio shall be kept within 2 meters of the thermal column at all times when the insert is either in motion or any other condition where the plug is not fully inserted into the reactor vessel. In the event that the plug is damaged, the reactor shall be placed into a shutdown and secured condition. The Reactor Director shall take possession of the console key and a sign placed upon the console indicating that operations are suspended until such time that the plug is either repaired or a replacement may be fabricated.

Appendix B

MARYLAND UNIVERSITY TRAINING REACTOR

PROPOSAL TO USE ION CHAMBERS FOR DOSE MAPPING

WITHIN THE THERMAL COLUMN

Table of Contents

PURPOSE

The purpose of this proposal is to provide a detailed procedure on how to measure the neutron and gamma-ray dose rates using ion chambers at various locations within the thermal column of the Maryland University Training Reactor. Measuring the dose rates will provide valuable information about the types of experiments that can be performed within the thermal column, especially in the field of nuclear medicine.

PRECAUTIONS AND REQUIREMENTS

Removing the access plug is classified as a Special Experiment. Therefore this proposal requires the approval of the Reactor Safety Committee and the Reactor Director. This proposal must also comply with the guidelines set by 10 CFR 50.59.

The Maryland University Training Reactor has never been run at power with the thermal column open, so the exposure of individuals working in the reactor building while measuring dose rates within the thermal column are unknown.

The dose rates must be measured while running at various power levels. These readings will be recorded and analyzed to predict trends before operating at the next highest power level.

If at any time during the radiation measurement process the radiation exceeds 100 mrem/hr outside of the thermal column, a high radiation area will be established and marked allowing positive control over individual access to the area in accordance with 10 CFR 20.1601.

Neutron detectors and gamma/beta detectors will be used to monitor the radiation levels at the face of the thermal column, as well as in the area where the ion chamber readings are being recorded.

In order to house the ion chambers at a stable location within the thermal column, an aluminum casing will be designed and fabricated so that no personnel is required to be near the opening of the thermal column when the reactor is operating.

After placement of the ion chambers in the thermal column, the access plug will be partially inserted into the thermal column to shield as much radiation as possible. Care will be taken to ensure that the integrity of the ion chambers and corresponding wires are not compromised by the insertion of the access plug.

Stay times will be calculated before removing the ion chamber housing, made of aluminum, to limit exposure to personnel.

The calibration of all radiation monitoring devices utilized in the removal process shall be verified within 24 hours of dose rate measurements.

Communication between the personnel on the ground floor taking dose rate measurements and reactor operator in the console will be through radio.

REQUIRED MATERIALS AND PREPARATIONS

Chain to mark off radiation area.

Lever Hoist – Columbus McKinnon Model 5318, rated at 3000 lbs or equivalent.

Neutron detectors and gamma/beta detectors to monitor radiation. (2 each)

Binoculars for monitoring detectors from South balcony.

Table rated at 2000 lbs. to support the access plug once it has been removed. The sides of the cart will contain lips to ensure that the plug does not fall off the cart.

Far West Technology Model IC-18, 0.1 cc ion chambers (2)

Keithley 6514 System Electrometer

Keithley low noise cable kits (2)

Canberra 3002 D power supply

Custom aluminum ion chamber housing

Radiation monitoring as recommended by the Radiation Safety Officer or their appointed representative.

PROCEDURE

Connect the cables from the electrometer to the ion chambers and place the ion chambers secured in the aluminum housing at the face of the lead bricks within the thermal column closest to the core.

Partially insert the access plug into the thermal column without touching the ion chambers or the cables.

Set up the neutron and gamma/beta detectors at the thermal column face and on the south balcony.

Notify the operator at the console that the ion chambers and access plug are in place and direct all personnel to the south balcony.

Increase reactor power and record dose rates from the ion chambers.

Secure the reactor for at least 24 hours prior to second round of measurements.

After 24 hours has passed, remove the access plug and place the ion chambers in the aluminum housing at the furthest end (away from the core) of the thermal column.

Set up the neutron and gamma/beta detectors at the thermal column face and on the south balcony.

Notify the operator that the ion chambers are in place and direct all personnel to the south balcony.

Increase reactor power and record the dose rates from the ion chambers.

Secure the reactor and wait for at least 24 hours before removing the ion chambers and inserting the access plug into the thermal column.

10CFR50.59 REVIEW

The removal of the thermal column does not require a License Amendment Request (LAR) as allowed under 10CFR50.59 for the following reasons:

This removal of the plug does not require a modification of the technical Specifications. (10CFR50.59(c)(1)(i)

The proposed experiment has been evaluated and does not meet the criteria set forth in 10CFR50.59(c)(2)

EMERGENCY RECOVERY

In the event that the radiation levels exceed the limits set forth previously as a high radiation area and becomes a very high radiation area, the measurement process will cease immediately. The reactor will be secured and all individuals will evacuate. Once the radiation levels have returned within the limits, personnel will insert the access plug into the thermal column. The Reactor Director will produce a new plan for dose rate measurements which includes measure taken to mitigate the possibility of another failure.

Appendix C

MARYLAND UNIVERSITY TRAINING REACTOR

PROPOSAL FOR IN VITRO CELL IRRADIATIONS WITHIN THE THERMAL COLUMN ENVIRONMENTAL CONTROL ACCESS PLUG

Table of Contents

PURPOSE

The purpose of this proposal is to request approval by the Reactor Safety Committee to perform irradiations of biological samples inside the thermal column of the MUTR using the protocol described in the following sections of this document. Previously, an environmental control thermal column access plug was designed and fabricated to house samples within the thermal column for exposure to thermal neutrons from the MUTR. The neutron spectrum and gamma dose rates have been measured and can now be used to develop radiation protocols for the *in vitro* irradiation of biological samples. The goal of this set of experiments is to determine the efficacy of a boron-containing cholesteryl ester mimic as an agent for Boron Neutron Capture Therapy (BNCT) of human prostate cancer.

MATERIALS TO BE IRRADIATED

The irradiated samples will include T-25 polystyrene tissue culture flasks containing human prostate cancer PC-3 cells, 5 mL of cell media (90% F12K and 10% fetal bovine serum), and 0.2 mL of boron-containing liposomal formulation (contains DL-α-dipalmitoylphosphatidylcholine (DPPC), cholesterol, and a boron-containing cholesteryl carborane ester compound(BCH)). The specification sheets for F12K and FBS are attached with this proposal.[1,2]

PRECAUTIONS AND REQUIREMENTS

Removing the access plug is classified as a Special Experiment. Therefore this experiment requires the approval of the Reactor Safety Committee and the Reactor Director. This proposal must also comply with the guidelines set by 10 CFR 50.59.

The Maryland University Training Reactor has previously been run at power with the thermal column partially open, thus the exposure of individuals working in the reactor building while measuring dose rates within the thermal column has been performed and is understood. For the *in vitro* irradiations, the thermal column access plug will be fully inserted into the reactor thermal column during operation, significantly reducing the dose rates around the reactor area.

Additionally, the neutron spectrum and gamma dose rates have been measured within the thermal column and thermal column access plug using ion chambers and foils. This allows the user to predict activation of experimental material and also provides insight into the activation of reactor structure, including the thermal column access plug, following exposure to a neutron flux.

Special consideration and planning was considered in the design and fabrication of the new thermal column access plug to ensure that adequate shielding is provided for protection of the radiation workers utilizing this experimental feature. The design of the

new plug is very similar to the existing setup, with a stepped feature approximately half way down the plug to prevent streaming from the reactor core. The construction of the plug consists of ½ inch carbon steel plates. Additionally, all pipe fittings are specially ordered carbon steel. Caution was taken to eliminate stainless steel components from the plug to limit the ^{60}Co created from thermal neutron irradiation of the plug components. The piping which delivers the water and gas to the sample chamber is copper. In order to account for creation of ^{16}N within the water and air channels, 50 feet of copper tubing was coiled on the outlet paths to increase the time required to exit the plug shielding. Given the half-life of ^{16}N as 7 seconds, this will provide adequate decay of the isotope within the plug. Once the internal components were tested, the access plug was backfilled with concrete for shielding. While pouring the concrete, care was taken to mix thoroughly to avoid air gaps. As a final measure, the length of the plug was extended 2 inches to increase the shielding planar to the sample chamber. During this particular set of experiments, there will be no gas or water flow through the thermal column plug.

If at any time during the sample irradiation the radiation level exceeds 100 mrem/hr outside of the thermal column, the operation will be paused and a high radiation area will be established and marked, allowing positive control over individual access to the area in accordance with 10 CFR 20.1601. The establishment of a high radiation area, if necessary, will be done under the approval of the Reactor Director.

Neutron detectors and gamma/beta detectors will be used to monitor the radiation levels at the face of the thermal column while loading, irradiating, and unloading samples in the thermal column.

The materials beings used in this set of experiments have been reviewed and no degradation that could cause an unanticipated increase to the hazards of experimental personnel is expected under the required operating conditions. Polystyrene tissue culture flasks have previously been exposed to significantly higher mixed neutron/gamma fields with no signs of physical degradation or long-lived activation. The break-down of styrene into its degradation products is not expected to result in a significant chemical-based risk to personnel handling the irradiated materials.

Previous experience with irradiated cell cultures has shown that there is very little activation of the cells or cell media. The polystyrene flasks tend to become slightly activated. It is estimated that a majority of the activation comes from the dyes used in the caps for the flasks and plasticizers. Activation products from previous irradiations of these flasks at AFRRI include Na-22, Na-24, Zn-96m, As-76 and Ru-106. The presence of Na-24 can be drastically reduced by handling the flasks with gloves rather than bare hands. Attached to this proposal is a gamma spectroscopy analysis of a Corning tissue culture flask that was irradiated at AFRRI in 2009 for 5 hours at 1 MW, 40 cm from the core.[3]

Communication between the personnel and reactor operator in the console will be through radio.

Radiation safety personnel will survey the samples after they are removed from the sample holder prior to release to the cell laboratory.

The liquid cell media that has been irradiated will be transferred to a bottle with a cap in the biological safety cabinet (BSC). This bottle will be labeled as radioactive material and be placed on an absorbing pad to ensure any spills are contained. There are two ways that the liquid can be treated from this point: 1) The bottles can be surveyed and if they are below background they can be treated as normal biological waste (neutralized with bleach and poured down the drain) or 2) Plaster of Paris can be added to the liquid to convert it to a solid.

Solid samples (cell culture flasks) will be disposed of into a radioactive waste container. The radioactive waste bags will be held in storage until they are at background levels with no removable contamination. At that point they can be autoclaved prior to disposal with other biological waste. On the other hand, the samples could also be transferred to a waste disposal contractor. Final determinations on the method of waste storage and removal will be made by Radiation Safety.

REQUIRED MATERIALS AND PREPARATIONS

Plastic chain, posts, and appropriate signage to mark off radiation area.

Lever Hoist – Columbus McKinnon Model 5318, rated at 3000 lbs or equivalent.

Neutron detectors and gamma/beta detectors to monitor radiation.

Table rated at 2000 lbs. to support the access plug once it has been removed.

Radiation monitoring as recommended by the Radiation Safety Officer or their appointed representative.

Cart for transfer of samples to and from 2325A and the reactor room.

PROCEDURE

Irradiation Procedure:

In vitro cell culture samples will be grown in T-25 Corning polystyrene tissue culture flasks prior to irradiation in the thermal column. The irradiated material will include a T-25 polystyrene tissue culture flask, 5 mL of cell media (90% F12K and 10% fetal bovine serum), 0.2 mL liposomal formulation (containing BCH, DPPC, and cholesterol), and human prostate cells PC-3.

Cells will be transported from the tissue culture laboratory and washed prior to securing the samples in the thermal column. Washing the flasks prior to irradiation will minimize the contaminants that can be activated by the neutron flux during the irradiation. Flasks will be handled with gloves at all times.

Flasks will be placed in the sample chamber of the thermal column access plug and the plug will be fully inserted into the thermal column.

Samples will be irradiated in the thermal column with the reactor at 250 kW for up to 20 minutes.

The reactor will be scrammed and the end of the desired irradiation time and allowed to decay for 10 minutes.

While monitoring the radiation levels with neutron and gamma detectors, the thermal column access plug will be removed and the samples will be retrieved from the plug.

The samples will be surveyed with radiation monitoring instruments to ensure that they can safely be transferred to the tissue culture laboratory for analysis. In addition, the samples will be swiped to test for removable contamination.

Upon completion of the experiment, the standard thermal column access plug will be fully inserted into the thermal column after the reactor is in a shutdown condition.

Post-irradiation Cell Colony Forming Assay Procedure:

Transfer cells to the cell culture laboratory.

Remove cell flask from the transfer container and place in the biological safety cabinet (BSC).

Remove irradiated cell flask cap and replace with new cap. Dispose of irradiated cap in dry Rad Waste Bin.

Discard irradiated media into liquid Rad Waste Container located in the BSC. Liquid Rad Waste Container is placed on absorbing pad to ensure any spills are contained.

Add 0.5 mL of trypsin-EDTA (25%) to the cell flask and incubate for 10 min.

Transfer cell flask to BSC and add 5 mL of medium to the flask. Using a pipette, mix the solution thoroughly.

Transfer desired volume of cell solution to new cell flasks, add 5 mL of media, and incubate for 10-14 days.

Dispose of irradiated flask in the dry Rad Waste Bin.

After incubation for 10-14 days, transfer cell flask to BSC.

Discard media into liquid Rad Waste Container.

Rinse the cells with 5 mL PBS and discard PBS into liquid Rad Waste Container.

Add 10 mL of 50:50 methanol:PBS solution to the cells and rinse. Discard solution in liquid Rad Waste Container.

Add 5 mL methanol to the flask and fix for 10 min.

Discard methanol in liquid Rad Waste Container.

Add 3 mL crystal violet to the flask and stain for 10 min.

Discard crystal violet into liquid Rad Waste Container.

Rinse cells with water and let dry.

Count colonies.

10CFR50.59 REVIEW

The removal of the thermal column does not require a License Amendment Request (LAR) as allowed under 10CFR50.59 for the following reasons:

This removal of the plug does not require a modification of the technical Specifications. (10CFR50.59(c)(1)(i)

The proposed experiment has been evaluated and does not meet the criteria set forth in 10CFR50.59(c)(2)

REFERENCES

[1]"F12K Kaighn's Modification Nutrient Mixture" Manufactured by CELLGRO (10-025).

http://cellgro.com/products/classical-media/f-12k-nutrient-mixture/f-12k-nutrient-mixture-kaighn-s-mod.html

[2]"Fetal Bovine Serum" Manufactured by CELLGRO (35-010).

http://cellgro.com/fetal-bovine-serum-regular.html

[3]"AFRRI Gamma Spectroscopy Analysis 09-008 Polystyrene Cell Culture Flask" Armed Forces Radiobiology Research Institute, Bethesda, MD. February 2009.

List of Abbreviations

ABNS: accelerator based neutron source

ANOVA: analysis of variance

BCH: cholesteryl 1,12-dicarba-closo-dodecaboranel-carboxylate

BNCT: boron neutron capture therapy

BNL: Brookhaven National Laboratory

BPA: 4-dihydroxyborylphenyl-alanine

BSE: Bayesian statistical estimator

BSH: borocaptate sodium Na_2[*closo*-$B_{12}H_{11}SH$]

CHOL: cholesterol

DC: direct current

DLS: dynamic light scattering

DNA: deoxyribonucleic acid

DPBS: Dulbecco's Phosphate Buffered Saline

DPPC: 1,2-dipalmitoyl-*sn*-glycero-3-phosphocholine

DSB: double-strand break

eV: electron volt

FDA: Food and Drug Administration

FWHM: full width at half maximum

GB-10: polyhedral borane dianion [*closo*-$B_{10}H_{10}$]$^{2-}$

GBM: glioblastoma multiforme

HPGe: high-purity germanium

HPLC: high-performance liquid chromatography

HRR: homologous recombination repair

ICP-MS: inductively couple plasma mass spectrometry

IUV: intermediate-sized unilamellar vesicle

LDH: lactate dehydrogenase

LDL: low-density lipoprotein

LET: linear energy transfer

LMV: large multilamellar vesicle

LoB: limit of blank

LoD: limit of detection

LoQ: limit of quantitation

MCMC: Monte Carlo Markov Chain

MCNP: Monte Carlo N-Particle

MDS: multimodal size distribution

MITR: Massachusetts Institute of Technology Reactor

MUTR: Maryland University Training Reactor

MTS: 3-(4,5-dimethylthaizol-2-yl)-5-(3-carboxymethoxyphenyl)-2-(4-sulfophenyl)-2H-tetrazolium

NADH: nicotinamide adenine dinucleotide dehydrogenase

NADPH: nicotinamide adenine dinucleotide phosphate

NARP: non-aqueous reverse phase

NHEJ: nonhomologous end joining

NIST: National Institute of Standards and Technology

NNLS: non-negatively constrained least squares

PC-3: human prostate cancer cell line

PC: phosphatidylcholine

PCS: photon correlation spectroscopy

PDT: population doubling time

PE: plating efficiency

PMMA: poly(methyl methacrylate)

QELS: quasi-elastic light scattering

RBE: relative biologic effectiveness

RF: radiofrequency

RSD: relative standard deviation

SF: surviving fraction

SSB: single-strand break

SUV: small unilamellar vesicle

TC: thermal column

TLD: thermal luminescent detector

TRIGA: Test, Research, Isotope production General Atomic

UZrH: uranium zirconium hydride

Bibliography

1. Siegel, R., D. Naishadham, and A. Jemal, *Cancer statistics, 2013.* CA Cancer J Clin, 2013. **63**(1): p. 11-30.

2. Chen, Y.F. and M. Hughes-Fulford, *Human prostate cancer cells lack feedback regulation of low-density lipoprotein receptor and its regulator, SREBP2.* International Journal of Cancer, 2001. **91**(1): p. 41-45.

3. Ji, B., G. Peacock, and D.R. Lu, *Synthesis of cholesterol-carborane conjugate for targeted drug delivery.* Bioorg Med Chem Lett, 2002. **12**(17): p. 2455-8.

4. Alanazi, F., et al., *Synthesis, preformulation and liposomal formulation of cholesteryl carborane esters with various fatty chains.* International Journal of Pharmaceutics, 2003. **255**(1-2): p. 189-197.

5. Mehta, S.C. and D.R. Lu, *Targeted drug delivery for boron neutron capture therapy.* Pharmaceutical Research, 1996. **13**(3): p. 344-351.

6. Barth, R.F., et al., *Boron neutron capture therapy of brain tumors: An emerging therapeutic modality.* Neurosurgery, 1999. **44**(3): p. 433-450.

7. Soloway, A.H., et al., *The chemistry of neutron capture therapy.* Chemical Reviews, 1998. **98**(4): p. 1515-1562.

8. Chen, W., S.C. Mehta, and D.R. Lu, *Selective boron drug delivery to brain tumors for boron neutron capture therapy.* Advanced Drug Delivery Reviews, 1997. **26**(2-3): p. 231-247.

9. Davis, M.A., et al., *Relative Biological Effectiveness of B-10(N, Alpha)7 Li Reaction in Hela Cells.* Radiation Research, 1970. **43**(3): p. 534.

10. Shaw, J.M., et al., *Delivery of Lipophilic Drugs Using Lipoproteins.* Annals of the New York Academy of Sciences, 1987. **507**: p. 252-271.

11. Asbury, A.K., et al., *Neuropathologic Study of 14 Cases of Malignant Brain Tumor Treated by Boron-10 Slow-Neutron Capture Radiation.* Journal of Neuropathology and Experimental Neurology, 1972. **3**(2): p. 278.

12. Farr, L.E., et al., *Neutron Capture Therapy with Boron in the Treatment of Glioblastoma Multiforme.* American Journal of Roentgenology, 1954. **71**(2): p. 279-293.

13. Sweet, W.H., Soloway, A.H., Brownell, G.L., *Boron-slow neutron capture therapy of gliomas.* Acta Radiol, 1963. **1**: p. 114-121.

14. Hatanaka, H. and Y. Nakagawa, *Clinical-Results of Long-Surviving Brain-Tumor Patients Who Underwent Boron Neutron-Capture Therapy.* International Journal of Radiation Oncology Biology Physics, 1994. **28**(5): p. 1061-1066.

15. Nakagawa, Y. and H. Hatanaka, *Boron neutron capture therapy: Clinical brain tumor studies.* J Neurooncol, 1997. **33**(1-2): p. 105-115.

16. Mishima, Y., et al., *Treatment of malignant melanoma by single thermal neutron capture therapy with melanoma-seeking 10B-compound.* Lancet, 1989. **2**(8659): p. 388-9.

17. Diaz, A.Z., *Assessment of the results from the phase I/II boron neutron capture therapy trials at the Brookhaven National Laboratory from a clinician's point of view.* J Neurooncol, 2003. **62**(1-2): p. 101-9.

18. Barth, R., et al., *Current status of boron neutron capture therapy of high grade gliomas and recurrent head and neck cancer.* Radiation Oncology, 2012. **7**(1): p. 1-21.

19. Curran, W.J., et al., *Recursive Partitioning Analysis of Prognostic Factors in 3 Radiation-Therapy Oncology Group Malignant Glioma Trials.* Journal of the National Cancer Institute, 1993. **85**(9): p. 704-710.

20. Barth, R.F., et al., *Boron neutron capture therapy of cancer: Current status and future prospects.* Clinical Cancer Research, 2005. **11**(11): p. 3987-4002.

21. Gabel, D., S. Foster, and R.G. Fairchild, *The Monte-Carlo Simulation of the Biological Effect of the B-10(N,Alpha)Li-7 Reaction in Cells and Tissue and Its Implication for Boron Neutron-Capture Therapy.* Radiation Research, 1987. **111**(1): p. 14-25.

22. Javid, M., G.L. Brownell, and W.H. Sweet, *The possible use of neutron-capturing isotopes such as boron 10 in the treatment of neoplasms. II. Computation of the radiation energies and estimates of effects in normal and neoplastic brain.* J Clin Invest, 1952. **31**(6): p. 604-10.

23. Barth, R.F., et al., *Boron Neutron-Capture Therapy for Cancer - Realities and Prospects.* Cancer, 1992. **70**(12): p. 2995-3007.

24. Barth, R.F., A.H. Soloway, and R.G. Fairchild, *Boron Neutron-Capture Therapy for Cancer.* Scientific American, 1990. **263**(4): p. 100.

25. Gabel, D., *Present Status and Perspectives of Boron Neutron-Capture Therapy.* Radiotherapy and Oncology, 1994. **30**(3): p. 199-205.

26. Kraft, S.L., et al., *Borocaptate sodium: a potential boron delivery compound for boron neutron capture therapy evaluated in dogs with spontaneous intracranial tumors.* Proc Natl Acad Sci U S A, 1992. **89**(24): p. 11973-7.

27. Mehta, S.C. and D.R. Lu, *Interspecies Pharmacokinetic Scaling of Bsh in Mice, Rats, Rabbits, and Humans.* Biopharmaceutics & Drug Disposition, 1995. **16**(9): p. 735-744.

28. Grafstein, D. and J. Dvorak, *Neoca]Boranes, a New Family of Stable Organoboranes Isomeric with Carboranes.* Inorganic Chemistry, 1963. **2**(6): p. 1128.

29. Coderre, J.A., et al., *Boron Neutron-Capture Therapy of a Murine Melanoma.* Cancer Research, 1988. **48**(22): p. 6313-6316.

30. Coderre, J.A., et al., *Selective Delivery of Boron by the Melanin Precursor Analog Para-Boronophenylalanine to Tumors Other Than Melanoma.* Cancer Research, 1990. **50**(1): p. 138-141.

31. Snyder, H.R., A.J. Reedy, and W.J. Lennarz, *Synthesis of Aromatic Boronic Acids - Aldehydo Boronic Acids and a Boronic Acid Analog of Tyrosine.* Journal of the American Chemical Society, 1958. **80**(4): p. 835-838.

32. Soloway, A.H., R.L. Wright, and J.R. Messer, *Evaluation of Boron Compounds for Use in Neutron Capture Therapy of Brain Tumors .1. Animal Investigations.* Journal of Pharmacology and Experimental Therapeutics, 1961. **134**(1): p. 117.

33. Ichihashi, M., T. Nakanishi, and Y. Mishima, *Specific Killing Effect of B-10(1)-Para-Boronophenylalanine in Thermal-Neutron Capture Therapy of Malignant-Melanoma - Invitro Radiobiological Evaluation.* Journal of Investigative Dermatology, 1982. **78**(3): p. 215-218.

34. Sweet, W.H., A.H. Soloway, and R.L. Wright, *Evaluation of Boron Compounds for Use in Neutron Capture Therapy of Brain Tumors .2. Studies in Man.* Journal of Pharmacology and Experimental Therapeutics, 1962. **137**(2): p. 263.

35. Soloway, A.H., H. Hatanaka, and M.A. Davis, *Penetration of Brain and Brain Tumor .7. Tumor-Binding Sulfhydryl Boron Compounds.* Journal of Medicinal Chemistry, 1967. **10**(4): p. 714.

36. Barth, R.F., *Boron neutron capture therapy at the crossroads: Challenges and opportunities.* Applied Radiation and Isotopes, 2009. **67**(7–8, Supplement): p. S3-S6.

37. Barth, R.F., *A critical assessment of boron neutron capture therapy: an overview.* Journal of Neuro-Oncology, 2003. **62**(1): p. 1-5.

38. Ji, B.Q., G. Peacock, and D.R. Lu, *Synthesis of cholesterol-carborane conjugate for targeted drug delivery.* Bioorganic & Medicinal Chemistry Letters, 2002. **12**(17): p. 2455-2458.

39. Versluis, A.J., et al., *Synthesis of a lipophilic daunorubicin derivative and its incorporation into lipidic carriers developed for LDL receptor-mediated tumor therapy.* Pharmaceutical Research, 1998. **15**(4): p. 531-537.

40. Kader, A., et al., *Drug targeting using low density lipoprotein (LDL): Physicochemical factors affecting drug loading into LDL particles.* Journal of Controlled Release, 1998. **55**(2-3): p. 231-243.

41. Krieger, M., et al., *Replacement of Neutral Lipids of Low-Density Lipoprotein with Esters of Long-Chain Unsaturated Fatty-Acids.* Journal of Biological Chemistry, 1979. **254**(10): p. 3845-3853.

42. Pan, G.L., S. Oie, and D.R. Lu, *Uptake of the carborane derivative of cholesteryl ester by glioma cancer cells is mediated through LDL receptors.* Pharmaceutical Research, 2004. **21**(7): p. 1257-1262.

43. Peacock, G., et al., *In vitro uptake of a new cholesteryl carborane ester compound by human glioma cell lines.* J Pharm Sci, 2004. **93**(1): p. 13-9.

44. Peacock, G.F., et al., *Cell culture studies of a carborane cholesteryl ester with conventional and PEG liposomes.* Drug Deliv, 2003. **10**(1): p. 29-34.

45. Caruso, M.G., et al., *Prognostic value of low density lipoprotein receptor expression in colorectal carcinoma.* Oncology Reports, 1998. **5**(4): p. 927-930.

46. Maletinska, L., et al., *Human glioblastoma cell lines: Levels of low-density lipoprotein receptor and low-density lipoprotein receptor-related protein.* Cancer Research, 2000. **60**(8): p. 2300-2303.

47. Laster, B.H., et al., *Biological Efficacy of Boronated Low-Density-Lipoprotein for Boron Neutron-Capture Therapy as Measured in Cell-Culture.* Cancer Research, 1991. **51**(17): p. 4588-4593.

48. Ho, Y.K., et al., *Low-density lipoprotein (LDL) receptor activity in human acute myelogenous leukemia cells.* Blood, 1978. **52**(6): p. 1099-114.

49. Lestavel-Delattre, S., et al., *Low-density lipoprotein for delivery of an acrylophenone antineoplastic molecule into malignant cells.* Cancer Res, 1992. **52**(13): p. 3629-35.

50. Maxfield, F.R. and I. Tabas, *Role of cholesterol and lipid organization in disease.* Nature, 2005. **438**(7068): p. 612-21.

51. Lasic, D.D., *Doxorubicin in sterically stabilized liposomes (vol 380, pg 562, 1996).* Nature, 1996. **381**(6583): p. 630-630.

52. Harling, O. and K. Riley, *Fission reactor neutron sources for neutron capture therapy — a critical review.* J Neurooncol, 2003. **62**(1-2): p. 7-17.

53. Moss, R.L., et al., *The requirements and development of neutron beams for neutron capture therapy of brain cancer.* J Neurooncol, 1997. **33**(1-2): p. 27-40.

54. Riley, K.J., P.J. Binns, and O.K. Harling, *A state-of-the-art epithermal neutron irradiation facility for neutron capture therapy.* Physics in Medicine and Biology, 2004. **49**(16): p. 3725-3735.

55. Coderre, J.A., et al., *Boron neutron capture therapy for glioblastoma multiforme using p-boronophenylalanine and epithermal neutrons: Trial design and early clinical results.* Journal of Neuro-Oncology, 1997. **33**(1-2): p. 141-152.

56. Wang, C.K.C., T.E. Blue, and R. Gahbauer, *A Neutronic Study of an Accelerator-Based Neutron-Irradiation Facility for Boron Neutron-Capture Therapy.* Nuclear Technology, 1989. **84**(1): p. 93-107.

57. Yanch, J.C., et al., *Accelerator-Based Epithermal Neutron Beam Design for Neutron-Capture Therapy.* Medical Physics, 1992. **19**(3): p. 709-721.

58. Blue, T.E. and J.C. Yanch, *Accelerator-based epithermal neutron sources for boron neutron capture therapy of brain tumors.* J Neurooncol, 2003. **62**(1-2): p. 19-31.

59. *Technical Foundations of TRIGA*, 1958, General Atomic: San Diego, CA.

60. Shaw, J.M., et al., *Delivery of lipophilic drugs using lipoproteins.* Ann N Y Acad Sci, 1987. **507**: p. 252-71.

61. Knoll, G.F., *Radiation Detection and Measurement*. 4th ed2010: John Wiley &Sons, Inc.

62. Hobbie, R.K.a.R., B.J., *Intermediate Physics for Medicine and Biology*. 4th ed2007, New York, NY: Springer.

63. Bramblett, R.L., R.I. Ewing, and T.W. Bonner, *A new type of neutron spectrometer.* Nuclear Instruments and Methods, 1960. **9**(1): p. 1-12.

64. Bell, G.I.a.G., S., *Nuclear Reactor Theory*1970: Van Nostrand Reinhold, Inc.

65. Burgett, E., et al., *Neutron spectral measurement of the Ohio state research reactor pneumatic tube.* Journal of Radioanalytical and Nuclear Chemistry, 2009. **282**(1): p. 187-191.

66. Wang, C.K., et al., *Experimental validation of the new nanodosimetry-based cell survival model for mixed neutron and gamma-ray irradiation.* Phys Med Biol, 2007. **52**(17): p. 367-74.

67. Scarboro, S., et al., *Validation of a Monte Carlo simulation of a thyroid uptake system using various sources and a slab phantom*. Nuclear Technology, 2009. **168**(1): p. 169-172.

68. Reginatto, M. and P. Goldhagen, *Maxed, a computer code for maximum entropy deconvolution of multisphere neutron spectrometer data.* Health Physics, 1999. **77**(5): p. 579-583.

69. Reginatto, M., *The "Few Channel" Unfolding Programs in the UMG Package MXD_C33, GRV_FC33, and IQU_FC33 UMG Package 3.3*, 2004.

70. Mohamed, A.B., *Flux Maps Obtained from Core Geometry Approximations: Monte Carlo Simulations and Benchmark Measurements for a 250 kW TRIGA Reator*, in *Graduate Program in Materials Science and Engineering* 2009, University of Maryland: College Park, MD.

71. Burgett. E., B., K., Blaylock, D., Hertel, N. *Uncertainty Analysis in the Determination of a Site-Specific TLD Neutron Factor*. in *American Nuclear Society*. 2007. Boston, MA.

72. Curran, S.C., *Proportional Counter Spectrometry*. Beta and Gamma-Ray Spectroscopy, K. Siegbahn 1955, Holland, Amsterdam: Elsevier-North.

73. Attix, F.H., *Introduction to Radiological Physics and Radiation Dosimetry* 2004, Weinheim: Wiley-VCH Verlag GmbH & Co. KGaA.

74. Wang, Z., Hertel, N.E., and Lennox, A., *Calibration of the borated ion chamber at NIST reactor thermal column.* Radiation Protection Dosimetry, 2007. **126**(1-4): p. 626-630.

75. Sweezy, J.E., *Development of a Boron Neutron Capture Enhanced Fast Neutron Therapy Beam*, in *Nuclear and Radiological Engineering*2002, The Georgia Institute of Technology: Atlanta, GA.

76. Attix, F.H., Pearson, D.W., DeLuca, P.M., and Goetsch, S.J., *Comparison of the Bragg-Gray theory corollaries to fast-neutron cavity ionization measurements at 14.8 MeV.* Health Physics, 1980. **38**(4): p. 623-633.

77. Rogers, D.W.O.a.R., C.K., *The role of humidity and other correction factors in the AAPM TG-21 dosimetry protocol.* Medical Physics, 1988. **15**(1): p. 40-49.

78. Attix, F.H., *Determination of the Aion and Pion in the new AAPM radiotherapy dosimetry protocol.* Medical Physics, 1984. **11**(5): p. 714-716.

79. New, R.R.C., *Liposomes*. A Pratical Approach, ed. D.a.H. Rickwood, B.D.1990, New York: Oxford University Press.

80. Hamilton, R.L., Jr., et al., *Unilamellar liposomes made with the French pressure cell: a simple preparative and semiquantitative technique.* J Lipid Res, 1980. **21**(8): p. 981-92.

81. Barenholtz, Y., Amselem, S., and Lichtenberg, D., *A new method for preparation of phospholipid vesicles (liposomes) - French press.* FEBS Lett., 1979. **99**: p. 210-214.

82. Sampedro, F., et al., *Liposomes as carriers of different new lipophilic antitumour drugs: a preliminary report.* J Microencapsul, 1994. **11**(3): p. 309-18.

83. Lai, M.Z., N. Duzgunes, and F.C. Szoka, *Effects of replacement of the hydroxyl group of cholesterol and tocopherol on the thermotropic behavior of phospholipid membranes.* Biochemistry, 1985. **24**(7): p. 1646-53.

84. Shahidi, F.a.Z., Y., *Lipid Oxidation: Measurement Methods*, in *Bailey's Industrial Oil and Fat Products*, F. Shahidi, Editor 2005, John Wiley & Sons, Inc.

85. Pike, E.R., *The Analysis of Polydisperse Scattering Data*. Scattering Techniques Applied to Supramolecular and Nonequilibrium Systems, ed. S.H. Chen, Chu, B., Nossal, R.1981, New York, New York: Plenum Press.

86. Grabowski, E.a.M., I., *Particle Size Distributions from Analysis of Quasi-Elastic Light Scattering Data*. Measurements of Suspended Particles by Quasi-Elastic Light Scattering, Dahneke 1983, New York: Wiley-Interscience.

87. Kaighn, M.E., et al., *Establishment and characterization of a human prostatic carcinoma cell line (PC-3).* Invest Urol, 1979. **17**(1): p. 16-23.

88. *Thawing, Propagating, and Cryoporeserving Protocol NCI-PBCF-CRL1435 (PC-3) Prostate Adenocarcinoma*, A.T.C.C. (ATCC), Editor 2012.

89. Borenfreund, E.a.P., J., *Toxicity determined in vitro by morphological alterations and neutral red absorption.* Toxicol. Lett., 1985. **24**: p. 119-124.

90. Repetto, G., del Peso, A., and Zurita, J.L., *Neutral red uptake assay for the estimation of cell viability/cytotoxicity.* Nat. Protoc., 2008. **3**(7): p. 1125-1131.

91. Barltrop, A.J., Owen, C.T., Cory, H.A., and Cory, G.J., *5-(3-Carboxylmethoxyphenyl)-2-(4,5-dimethylthiazolyl)-3-(4-sulfophenyl) tetrazolium, inner salt (MTS) and related analogs of 3-(4,5-dimethylthiazolyl)-2,5-diphenyltetrazolium bromide (MTT) reducing to purple water-soluble formazans as cell-vi-ability indicators.* Bioorg. Med. Chem. Lett., 1991. **1**: p. 611-614.

92. Berridge, M.V.a.T., A.S., *Characterization of the cellular reduction of 3-(4,5-dimethylthiazol-2-yl)-2,5-diphenyltetrazolium bromide (MTT): subcellular localization, substrate dependence, and involvement of mitochondrial electron transport in MTT reduction.* Arch. Biochem. Biophys., 1993. **303**: p. 474-482.

93. Riss, T.L.a.M., R.M., *Comparison of MTT, XTT, and a novel tetrazolium compound MTS for in vitro proliferation and chemosensitivity assays.*, in *Molecular Biology of the Cell* 1992.

94. Cory, A.H., Owen, T.C., Barltrop, J.A., and Cory, J.G., *Use of an aqueous soluble tetrazolium/formazan assay for cell growth assays in culture.* Cancer Commun., 1991. **3**(7): p. 207-212.

95. Nachlas, M.M., et al., *THE DETERMINATION OF LACTIC DEHYDROGENASE WITH A TETRAZOLIUM SALT.* Analytical Biochemistry, 1960. **1**(4-5): p. 317-326.

96. Decker, T. and M.L. Lohmann-Matthes, *A quick and simple method for the quantitation of lactate dehydrogenase release in measurements of cellular cytotoxicity and tumor necrosis factor (TNF) activity.* J Immunol Methods, 1988. **115**(1): p. 61-9.

97. Korzeniewski, C. and D.M. Callewaert, *An enzyme-release assay for natural cytotoxicity.* J Immunol Methods, 1983. **64**(3): p. 313-20.

98. Cullen, P., et al., *An improved method for quantification of cholesterol and cholesteryl esters in human monocyte-derived macrophages by high performance liquid chromatography with identification of unassigned cholesteryl ester species by means of secondary ion mass spectrometry.* J Lipid Res, 1997. **38**(2): p. 401-9.

99. Araki, N., et al., *Microquantification of cholesterol and cholesteryl esters in rat peritoneal macrophages by reverse-phase high-performance liquid chromatography.* Anal Biochem, 1990. **185**(2): p. 339-45.

100. Vercaemst, R., A. Union, and M. Rosseneu, *Separation and quantitation of free cholesterol and cholesteryl esters in a macrophage cell line by high-performance liquid chromatography*. J Chromatogr, 1989. **494**: p. 43-52.

101. Greenspan, M.D., et al., *Separation and identification of triglycerides, cholesteryl esters, cholesterol, 7-dehydrocholesterol, dolichol, ubiquinone, alpha-tocopherol, and retinol by high performance liquid chromatography with a diode array detector.* J Lipid Res, 1988. **29**(7): p. 971-6.

102. Sidwell, R.A., *Extraction and Analysis by HPLC of the Novel Compound BCH in Formulations, Cell Culture, and Animal Tissue.*, 2002, University of Georgia.

103. Sah, R.N. and P.H. Brown, *Isotope ratio determination in boron analysis.* Biol Trace Elem Res, 1998. **66**(1-3): p. 39-53.

104. Downing, R.G., et al., *Considerations in the determination of boron at low concentrations.* Biol Trace Elem Res, 1998. **66**(1-3): p. 3-21.

105. Vanderpool, R.A., D. Hoff, and P.E. Johnson, *Use of inductively coupled plasma-mass spectrometry in boron-10 stable isotope experiments with plants, rats, and humans.* Environ Health Perspect, 1994. **102 Suppl 7**: p. 13-20.

106. Linko, S., et al., *Boron detection from blood samples by ICP-AES and ICP-MS during boron neutron capture therapy.* Scand J Clin Lab Invest, 2008. **68**(8): p. 696-702.

107. Heber, E.M., et al., *Boron delivery with liposomes for boron neutron capture therapy (BNCT): biodistribution studies in an experimental model of oral cancer demonstrating therapeutic potential.* Radiat Environ Biophys, 2012. **51**(2): p. 195-204.

108. Wittig, A., et al., *Boron analysis and boron imaging in biological materials for Boron Neutron Capture Therapy (BNCT).* Crit Rev Oncol Hematol, 2008. **68**(1): p. 66-90.

109. Thomas, R., *A Beginner's Guide to ICP-MS.* Spectroscopy, 2001. **16**.

110. Smith, F.G., et al., *Measurement of boron concentration and isotope ratios in biological samples by inductivey coupled plasma mass spectrometry with direct injection nebulization.* Analytica Chimica Acta, 1991. **248**(1): p. 229-234.

111. *Theory of Sample Preparation Using Acid Digestion, Pressure Digestion and Microwave Digestion (Microwave Decomposition)*, Berghof Products and Instruments GmbH: Germany.

112. Peacock, G., et al., *In vitro uptake of a new cholesteryl carborane ester compound by human glioma cell lines.* Journal of Pharmaceutical Sciences, 2004. **93**(1): p. 13-19.

113. Vital-Reyes, V.S., et al., *Cell density influences the effect of celecoxib in two carcinoma cell lines.* Biotech Histochem, 2006. **81**(1): p. 51-4.

114. Graves, R., et al., *Noninvasive, real-time method for the examination of thymidine uptake events--application of the method to V-79 cell synchrony studies.* Anal Biochem, 1997. **248**(2): p. 251-7.

115. Gad, S.C., *In Vitro Toxicology*. 2nd ed 2000: CRC Press.

116. Uehara, S. and H. Nikjoo, *Monte Carlo simulation of water radiolysis for low-energy charged particles.* J Radiat Res, 2006. **47**(1): p. 69-81.

117. Balagamwala, E.H., Stockham, A., Macklis, R., Singh, A.D., *Introduction to Radiotherapy and Standard Teletherapy Techniques*. Ophthalmic Radiation Therapy, ed. A.D. Singh, Pelayes, D.E., Seregard, S., Macklis, R. Vol. 52. 2013: Karger.

118. Hall, E.J., Giaccia, A.J., *Radiobiology for the Radiologist*. 6th ed2006, Philadelphia, PA: Lippincott Williams and Wilkins.

119. Jackson, S.P., *Sensing and repairing DNA double-strand breaks.* Carcinogenesis, 2002. **23**(5): p. 687-96.

120. Ward, J.F., *The yield of DNA double-strand breaks produced intracellularly by ionizing radiation: a review.* Int J Radiat Biol, 1990. **57**(6): p. 1141-50.

121. Franken, N.A.P., et al., *Clonogenic assay of cells in vitro.* Nature Protocols, 2006. **1**(5): p. 2315-2319.

122. Brown, J.M. and L.D. Attardi, *The role of apoptosis in cancer development and treatment response.* Nat Rev Cancer, 2005. **5**(3): p. 231-7.